Optimization and analysis of Deep-UV imaging systems

Optimization and analysis of Deep-UV imaging systems

Proefschrift

ter verkrijging van de graad van doctor
aan de Technische Universiteit Delft,
op gezag van de Rector Magnificus Prof.dr.ir. J.T. Fokkema,
voorzitter van het College voor Promoties,
in het openbaar te verdedigen op
woensdag 5 oktober 2005 om 10:30 uur

door

Alexander Georgievich SEREBRIAKOV

Master of Science
State University of Information Technologies, Mechanics and Optics,
geboren te Leningrad, USSR

Dit proefschrift is goedgekeurd door de promotor:
Prof.dr.ir. J.J.M. Braat.

Samenstelling promotiecommissie:

Rector Magnificus,	Voorzitter
Prof.dr.ir. J.J.M. Braat,	Technische Universiteit Delft, promotor
Prof.dr. T.M. Klapwijk,	Technische Universiteit Delft
Prof.dr. H.P. Urbach,	Technische Universiteit Delft
Prof.dr.ir. L.J. van Vliet,	Technische Universiteit Delft
Prof.dr. I.L. Livshits,	State University of Information Technologies, Mechanics and Optics, St. Petersburg, Rusland
Dr. F. Bociort,	Technische Universiteit Delft
Dr. H. Feldmann,	Carl Zeiss SMT AG, Duitsland
Prof.dr.ir. A. Gisolf,	Technische Universiteit Delft, reservelid

Dr. F. Bociort has provided substantial guidance and support in the preparation of this thesis.

Table of contents

1. Introduction

1.1. Historical overview of imaging systems development

Image formation is the main application of traditional optical systems such as loupe, telescope, microscope, camera, etc. In fact, lenses form images even if this is not their intended purpose.

The history of optics and, in particular, imaging optical devices begins in ancient Greece. The famous comic playwright Aristophanes mentioned the reflection of the sun's rays. Greek philosophers, such as Democritus and Aristotle, discussed the nature of vision in their works. The well-known story of Archimedes who is reported focusing the sun's rays to burn Romans ships during a battle for Syracuse in 213 BC seems to be only a legend, reported in the Middle Ages. However, in the Roman Empire, the philosopher Seneca noted the magnification of objects observed through transparent vessels filled with water. According to legend, his pupil, the Emperor Nero, was the first one who used a monocle while watching fights in the arena. Ptolemy of Alexandria, besides his astronomical and mathematical discoveries, measured the refractive effect of water and discussed the refractive effects of the atmosphere. At the beginning of the XI century, the famous Persian Alhazen formulated the laws of reflection and refraction and researched reflection with spherical and parabolic mirrors. The first imaging optical device was a camera obscura used to form images on a wall in darkened room. In antiquity the camera obscura, being a lensless device, formed image via a pinhole.

The first recorded analysis of the magnifying properties of lenses was made by Roger Bacon in 1262. Around 1284 in Italy, Salvino D'Armate has been given credit for inventing the first wearable eyeglasses which spread rapidly in Europe. A correct explanation of their principle, was done only in 1604 with the publication of the work of Johannes Kepler. About this time the camera obscura was upgraded by enlarging the hole, which became possible after inserting a telescope lens.

Credit for the first compound microscope (multiple lenses) is generally given to Zacharias Jansen of the Netherlands, in 1590. A Dutch spectacle maker Hans Lippershey invented a simple single lens objective for a refractor telescope in 1608. His contemporary, Galileo Galilei, also manufactured such telescopes that allowed him to make remarkable astronomical discoveries.

The first achromatic lens was made by Eustachio Divinus around 1657. He invented a telescope containing 19 lenses that "prevents discoloration of the image". In the year 1729 the Englishman Chester Moor Hall proposed the first achromatic doublet designed from two different types of glass.

Nicéphore Niépce was the first who combined the camera obscura with photosensitive paper as early as in 1816 and in 1826 he has got a permanent image. Works of Henry Fox Talbot and Louis Daguerre at the middle of the XIX century established the photography era and for more than hundred years the development of imaging devices continued mostly in the areas of photography, microscopy and astronomy. Józeph Miksa Petzval made his objective with extended aperture value in 1840. The Cooke triplet, the simplest lens system that allows - at the same time - the correction of third order aberrations and chromatism, was designed in 1893 by Dennis Taylor.

Since the discovery of X-rays by Röntgen in 1895 imaging devices went beyond the scope of visible optical range. Nowadays it is impossible even to mention all possible applications of imaging devices. They are found in all forms of human life from communication devices to astronomy, from medical endoscopes to quality and

security control, from digital camera to DVD players. These are only the most well-known items from the long list of applications of modern optics.

1.2.   Key issues in modern optical system design

Technologies based on computer microprocessors (chips) have penetrated in all kinds of everyday things, from satellites to kitchen devices, toys and personal computers. Chips fulfil different missions by design, but all processes in the chip are based on the mathematical computations and logical operations prescribed by the algorithms. Transistors in modern microprocessors are able to perform up to a few billions of commands per second. In order to meet the needs of society the manufactures use advanced tools to produce more and more chips and to increase their complexity. One of the most important tools is a photolithographic machine which contains an imaging optical system. According to World Semiconductor Trade Statistics, the world economy productivity can be linked to 30% per year growth with integrated circuits productivity, half of which is attributed to lithography improvements. The extension of present optical lithography technologies in manufacturing smaller chip's features allows to achieve this goal. Manufacturers employ the latest optical enhancement techniques in order to extend resolution capability. Each new generation of the lithographic machines faces new problems because of the use of new materials, methods and technologies. As a consequence, the design of the optical lithographic systems remains an extremely difficult process. Therefore, the design of these lithographic optical systems can be considered as the most challenging problem in modern optical design.

Nowadays optical designers possess highly advanced tools. Modern PCs are able to trace several millions of rays in an optical system per second. Such a huge computation speed helps to perform a fast analysis, but the development process is still a very time-consuming issue. With modern software for optical design a designer can start with a relatively rough sketch of the optical system and then software will optimize that sketch to achieve a required design goal. This optimization algorithm performs alterations of the starting system in order to satisfy certain conditions. In common cases the program varies design parameters within some limits to obtain the best image performance. This process becomes very complicated when the optical system has many parameters, the dependence between parameters and image quality is nonlinear and there are limitations defined by costs and manufacturing difficulties. One can say that a good optimization engine is the heart of the modern optical design software. Since optimization problems are also very important in other areas of engineering, an improvement of optimization algorithms is a relevant research subject in modern science.

1.3.   Outline of the thesis

This thesis is mainly devoted to two issues. The first one is the problem of the spatial dispersion in lithographic optical design, which was reported as a critical issue for new generations of lithographic objectives. We will focus on the mathematical description of this effect, on the analysis of issues caused by the effect in optical design and on the possible solutions for the compensation of the spatial dispersion in lithography.

The second issue is the global optimization problem. Our goal here is the development of a new global optimization method, which is built on the recently discovered regularities of the merit function landscape in optical design. This algorithm should be integrated with optical design software in order to be used for the

global optimization of optical systems. We expect that our new optimization approach can also provide designers with a special tool for analysis of complex optical design problems.

The outline of the thesis is as follows:

In Chapter 2 we give a short review of the lithographic imaging techniques. First we briefly discuss the basics of integrated circuits including key points such as Moore's Law and the International Technology Roadmap for Semiconductors. Then we give a brief introduction in chip technology and show the importance of lithographic tools in the manufacturing of chips. We also discuss the problem of resolution in optical lithography which defines the critical dimension size for microprocessors. Finally we show the evolution of the lithographic objectives since the 1960s to the near future.

In Chapter 3 we analyze the effect of spatial dispersion in crystals. We start from the general relationship for birefringence in crystalline media and then we obtain the expressions for the eigenpolarizations and the linear birefringence value in cubic crystals for an arbitrary ray direction

Chapter 4 is devoted to the effect of spatial dispersion in optical system design. We give a description of polarization effects in optical design and then we discuss the consequences of spatially induced birefringence for deep ultraviolet (DUV) lithography. We show that the presence of spatial dispersion may lead to severe image contrast loss.

Several possible approaches to the compensation of the phase retardation induced by spatial dispersion in lithographic objectives are discussed in Chapter 5. We discuss possible strategies and offer a number of compensation methods including examples of optical systems with compensated phase retardation.

In Chapter 6 we give an introduction to the problem of optical system optimization. We start with a description of the optimization problem in general and then we discuss the specific issues of the optimization in optics such as merit function construction, constraints, etc. We also give a review of the present methods and further we focus on some promising extensions of local optimization.

In Chapter 7 we discuss our approach to the global optimization problem. First, we try to find some regularity by looking at the topography of the merit function landscape with the help of the equimagnitude contours. Then we show the importance of the saddle points in the merit function landscape. Focussing on the saddle points we prove that they lead to the specific order in the lens composition. We show the existence of networks of optical systems consisting of local minima of the merit function connected via saddle points. Finally we present our algorithm of obtaining saddle points and computing eigenvectors in the multidimensional merit function space.

We show several examples of optical system networks in Chapter 8. On the base of our "saddle points" approach we explore the networks of optical systems for systems of different complexity starting from a single lens to lithographic objectives.

We conclude this thesis with the final discussion of the results of this research and short summaries in English and Dutch.

2. Current state of lithography

2.1.   Integrated circuits: a brief overview

The semiconductor industry started with the invention of the first semiconductor transistor by William Shockley, John Bardeen, and Walter Brattain at Bell Labs in 1947 [1]. Despite its simplicity, the device performed its function of using an applied voltage to switch and amplify electrical current quite well. This device was the parent of all of the various semiconductor transistor devices produced over the years. The new transistor started to replace vacuum tubes and opened new areas of use. In 1960 Jack Kilby and Robert Noyce made the next major step in semiconductors with the invention of the first monolithic integrated circuit [2]. Their integrated device consisted of many transistors that were placed on a single semiconductor substrate. The ability to interconnect the devices internally allowed to perform more complex functions by a single device. The "integrated circuit" gave rise to the modern microelectronics era.

The semiconductor manufacturers have made a significant progress since 1960, when device features were about 20 mm wide. Nowadays, semiconductor devices have critical dimensions (the smallest circuit element) in the device as small as 0.09 micron. Drastic reduction of feature size allows to integrate more and more devices on a single chip, which results in more functionally powerful products. It has to be mentioned that while the feature size decreases and the number of elements in integrated devices increases, the overall cost of producing a semiconductor device remains reasonably constant. This leads to a dramatic increase in the function per cost ratio for semiconductor devices. Reduction of critical dimension leads to dramatic growth in the speed of microprocessors as well.

In 1965, just five years after the first monolithic integrated circuit was made, Gordon Moore made his famous observation. Moore observed an exponential growth in the number of transistors per integrated circuit and predicted that this tendency would continue. Table 2.1.1 illustrates this tendency. Moore's Law still holds true today and makes lithographers expecting that it will continue at least through the end of this decade.

Table 2.1.1 Moore's Law for semiconductors.

Processor	Year of introduction	Clock speed	Transistors
4004	1971	108 kHz	2,250
8008	1972	200 kHz	2,500
8080	1974	2 MHz	5,000
8086	1978	10 MHz	29,000
286	1982	12 MHz	120,000
386™ processor	1985	16 MHz	275,000
486™ DX processor	1989	25 MHz	1,180,000
Pentium® processor	1993	60 MHz	3,100,000
Pentium II processor	1997	300 MHz	7,500,000
Pentium III processor	1999	733 MHz	24,000,000
Pentium 4 processor	2000	1.5 GHz	42,000,000
Pentium 4 processor	2004	3.4 GHz	178,000,000

2.2.   Introduction in microprocessor technology

A microprocessor is the one of the most complex devices on earth. The manufacturing of microprocessors comprises hundreds of steps. Microprocessors are formed by multilayer structures built on a silicon wafer using diverse processes [3].
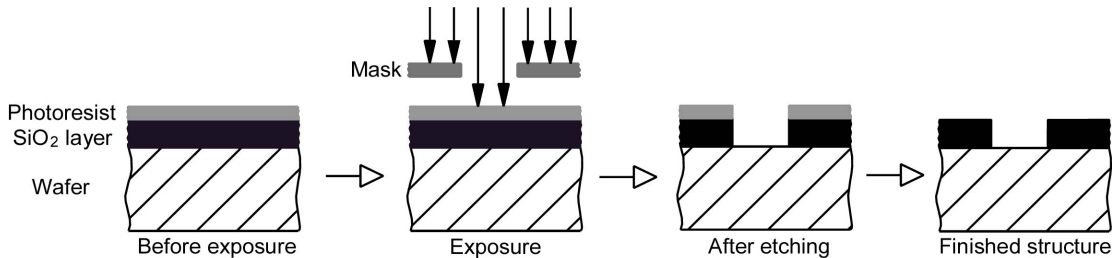
Figure 2.2.1 Patterning a layer above the silicon surface during photolithographic process (objective is not shown).

For our research the patterning process i.e. creating an image in a photoresist layer shown in Figure 2.2.1 is of interest. Patterning comprises silicon dioxide and photoresist deposition, exposure, photoresist development and etching. Commonly in the beginning of lithographic process, after preparation, the first layer of silicon dioxide is grown on the wafer. Then the wafer is coated with a photoresist which can be made soluble after exposing by light. In our research we assume the photolithographic exposition process shown schematically in Figure 2.2.2. Through the exposition process light from the source passes through a patterned mask which then is projected via an objective onto the coated silicon wafer.
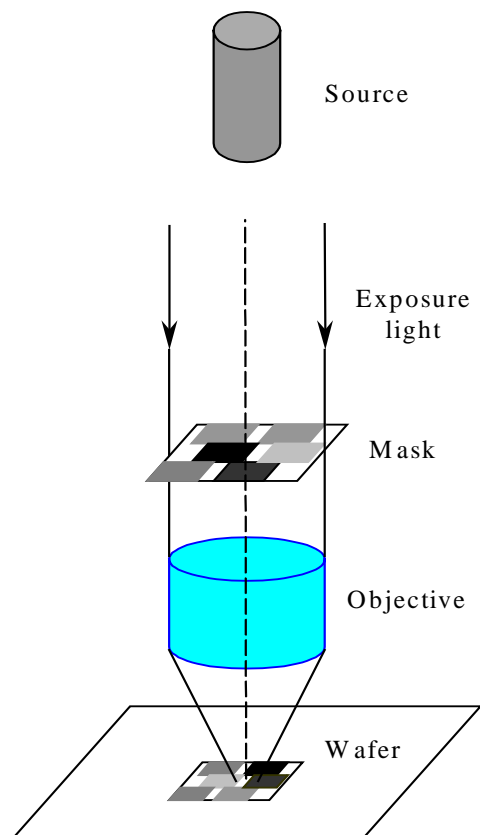
Figure 2.2.2 Exposure process. Light emitted from the source is projected through mask on the wafer via an objective.

The mask shields certain parts of the wafer from being exposed. In such a way light turns the exposed areas of the wafer into a gooey layer of photoresist which can be dissolved by a solvent. Later on, the uncovered silicon dioxide can be etched away with the help of chemicals. The unexposed areas protected by photoresist remain. At the end of the patterning process the rest of the photoresist is deleted baring ridges of silicon dioxide on the wafer.

Next, in order to create another structured layer, the pattering process is repeated and a new layer of silicon dioxide is grown over the wafer base. In many cases it is covered by polysilicon (conductive material used as an interconnect layer) and another layer of photoresist. This second layer of the microprocessor is exposed by using a second mask with a different pattern and after etching the gate-forming element remains. Through a process called ion implantation (or doping), ions are implanted in the wafer in the exposed areas which are able to conduct electricity. Another masking and etching stage leaves strips of a metal that form the electrical connections. About 20 connected layers form the 3-dimensional geometrical structure of a typical microprocessor circuitry based on the elementary transistor scheme.

a) **b)** **c)** **d)**
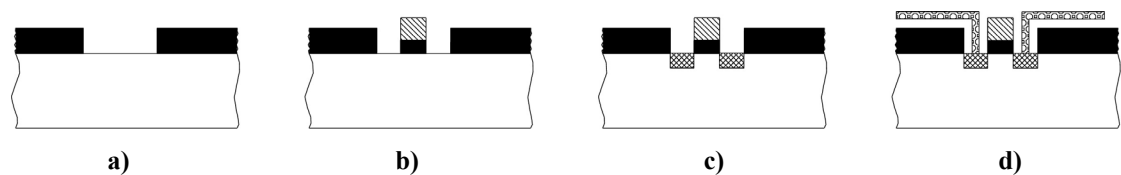
Figure 2.2.3 Building an elementary transistor on chip. a) wafer with field oxide; b) making polysilicon gate on thin oxide c) forming source/drain regions by ion implantation; d) forming connectors.

2.3. International Technology Roadmap for Semiconductors

The International Technology Roadmap for Semiconductors (ITRS) is an assessment of the semiconductor technology requirements [4]. The purpose of the ITRS is to set the guiding lines for the development of the integrated circuits performance. These reference points, all together called a roadmap, is a product of common effort of the global microelectronics industry, research institutes and government organizations. The ITRS shows the technological issues and requirements which will be encountered by the semiconductor industry over the next 15 years. The characteristics, relevant for our research are collected in Table 2.3.1.

In this table the Technology Node is the minimum half-pitch of custom-layout metal interconnects. This is the most representative characteristic of the technology capability enabling high-density integrated circuits. For each Node, the defined metal half-pitch is taken from products having the minimum value. Nowadays, a Dynamic Random Access Memory (DRAM) chip has the smallest metal pitch, therefore the half of its pitch (smallest element) is taken as a reference. Other parameters shown in Table 2.3.1 are important for characterizing integrated circuits technology as well. For instance, in the case of microprocessors (MPUs), physical bottom gate length is most representative of the leading-edge technology level required for maximum performance. Each technology node generation reflects the achievement of significant technology progress in metal half-pitch — about 70% of the previous node and 50% of two previous nodes. Taking the ITRS roadmap as a reference we can expect that the Moore's Law will remain valid at least in the near future.

Table 2.3.1 Roadmap of chip lithography.

Technology Characteristics	YEAR OF PRODUCTION						
	2003	2004	2005	2006	2007	2008	2009
Technology Nodes (nm)							
DRAM ½ Pitch	100	90	80	70	65	57	50
MPU ½ Pitch	107	90	80	70	65	57	50
MPU Printed Gate Length	65	53	45	40	35	32	28
MPU Physical Gate Length	45	37	32	28	25	22	20
Chip Frequency (MHz)							
On-chip local clock	2,976	4,171	5,204	6,783	9,285	10,972	12,369
Chip-to-board speed	2,000	2,500	3,125	3,906	4,883	6,103	7,629
Performance and Package Chips							
# Mask Levels — MPU	29	31	33	33	33	35	35
# Mask Levels — DRAM	24						
Maximum number wiring levels on chip — maximum	13	14	15	15	15	16	16
Maximum number wiring levels on chip — minimum	9	10	11	11	11	12	12
Lithographic-Field and Wafer-Size Trends							
Lithographic field size length (mm)	32						
Lithographic field size width (mm)	22						
Wafer size (diameter, mm)	300						

2.4. Resolution in optical lithography

As far as the technology node is the key parameter in the semiconductors technology it is taken as a reference for all adjacent areas. For lithographic imaging systems it is defined by critical dimension. The critical dimension of the patterns imaged on the wafer is limited by the imaging characteristics of the lithographic objective.

In the case of an ideal optical system all infinitesimal points on the object can be imaged as corresponding infinitesimal points on the image. However for a real system due to the diffraction and aberrations each point is imaged as a finite spot. The diameter of this spot and the distribution of light intensity within it can be reduced to the theoretical diffraction limit with the help of advanced optical system design. For lithographic objectives the strict respect of the orthoscopic condition, i.e. the rigorous observation of dimensional proportions, is required as well. This demands a correction of distortion and the maintaining of telecentricity of the beams in the image space.

There are many known characteristics of image quality, which can be described by geometrical and wavefront aberrations, spot diagrams, Point Spread Function (PSF), Modulation Transfer Function (MTF), Root Mean Squared (RMS) wavefront error and Strehl ratio [5]. The PSF describes the distribution of the light intensity of the image of the point source in the image plane. MTF is the spatial frequency response

of the imaging system; it is the contrast at a given spatial frequency relative to zero frequency. The Strehl ratio is the ratio of peak focal intensities in the real and in the ideal point spread functions. It allows to characterize image quality for each field point by only one number. The lithographic optical systems are diffraction-limited and only PSF, MTF and Strehl ratio in combination with the distortion value and the field curvature can describe their performance truthfully because these characteristics take into account polarization effects which are very important for optical system with high numerical aperture.

In optical projection lithography, the resolution δ of an objective (feature size) at the diffraction limit is given by the expression

$$\delta = k_1 \frac{\lambda}{NA}. \tag{2.4.1}$$

In this equation λ is the wavelength, NA is numerical aperture of the objective, and k_1 is an empirical constant. NA is defined by the formula

$$NA = n \sin \theta, \tag{2.4.2}$$

where θ is the half-angle of the image-forming light cone at the image side and n is the index of refraction of the medium in image space. It is known from optics theory that in the case of idealized conditions for two incoherent point sources, the Rayleigh criterion implies that $k_1 = 0.61$ and then δ is a distance between the central maximum of the Airy distribution and its first minimum. In lithographic practice, this coefficient depends on lens aberrations, illumination conditions (such a degree of coherence and intensity distribution in the aperture plane), mask structure, resist properties, process conditions, operator skills etc. It follows from the expression (2.4.1) that resolution can be improved in three ways: by increasing the numerical aperture, by shortening the exposure wavelength, and by decreasing the value of k_1 [6].
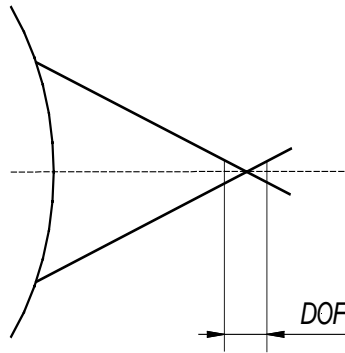
Figure 2.4.1 Depth of focus of optical system. The depth of focus is defined by permissible spot size at the image plane.

Optical resolution depends also on the depth of focus (DOF), because with the increase of NA the optical system becomes very sensitive to defocus. In common case the depth of focus for diffraction limited optical system is defined as half the distance along the optical axis between the central diffraction maximum and the first zero of the Airy distribution and it is given by the approximate expression

$$DOF = \frac{\lambda}{NA^2}. \tag{2.4.3}$$

However in lithography an effective depth of focus is defined as

$$DOF = k_2 \frac{n\lambda}{NA^2}, \tag{2.4.4}$$

where k_2 is also an empirically determined constant (it is a specific lithographic process-related factor as well) and n is the index of refraction of the medium in image space. Eliminating NA from (2.4.1) and (2.4.4) we obtain

$$DOF = \frac{k_2 n \delta^2}{k_1^2 \lambda}.$$
(2.4.5)

In practice, the coefficients k_1 and k_2 are experimentally determined for each exposure tool. At high numerical aperture, the formulae above have to be adopted [7].

2.5.   Evolution of lithographic objectives

The first high-aperture UV optical systems were developed in the beginning of the XXth century when the first monochromatic UV micro-objectives for ultra-high resolution microscopy were introduced. These objectives had a NA value as large as 0.35, the working wavelength was at 280 nm (magnesium line) and lenses were made from fused quartz.

The intensive research on lithographic optics design started in the 1960s together with the integral circuits invention. The pioneers of lithography used photographic objectives for the lithographic projection. However in the late 1960s companies like CERCO, Carl Zeiss and IBM started developing ultraviolet reduction lenses for production of masks and later for projection onto the wafer [8]-[10]. These schemes were based on photographic objectives as well but they had a significant difference required by the orthoscopic condition. Most of them were realized on the base of classical Gauss-type objective with adding several correction components. One of these objectives introduced by IBM in 1974 and called Lentar is shown in Figure 2.5.1. The materials for the lenses were glasses from the Schott catalog.
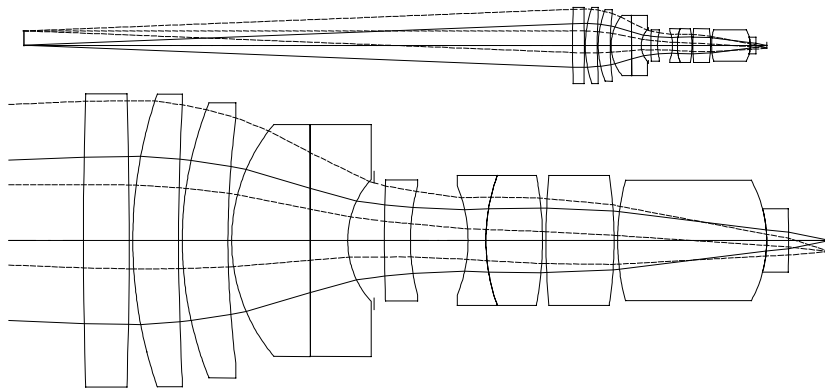
**Figure 2.5.1 Lithographic objective Lentar (1974) with image side *NA* = 0.2,
image field size 15 × 15 mm², working wavelength 405 nm, reduction ratio 0.2.**

As it follows from equations (2.4.1) and (2.4.4) the resolution can be improved by increasing NA, and by decreasing the factors k_1, k_2 and the wavelength. Since 1960s lithographers have been developing technologies at progressively shorter wavelengths. In the past, the used wavelengths were 436 nm (g-line), 405 nm (h-line) and 365 nm (i-line). In the 1970s and early 1980s, optical exposure tools operated at 400 nm on average, and the feature sizes were always larger than the working wavelength of the exposure tool. Currently, most systems use 248 nm and 193 nm. The sources of radiation are a KrF excimer laser at 248 nm and an ArF excimer laser at 193 nm. In the future, wavelengths could be shortened to 157 nm (F$_2$ laser) or less. At each step to lower wavelength and higher NA, besides other issues, lithographers

should find solutions for the source, the lens material, and the required polishing accuracy [11]. An example of an optical system working at a wavelength of 248 nm is shown in Figure 2.5.2.
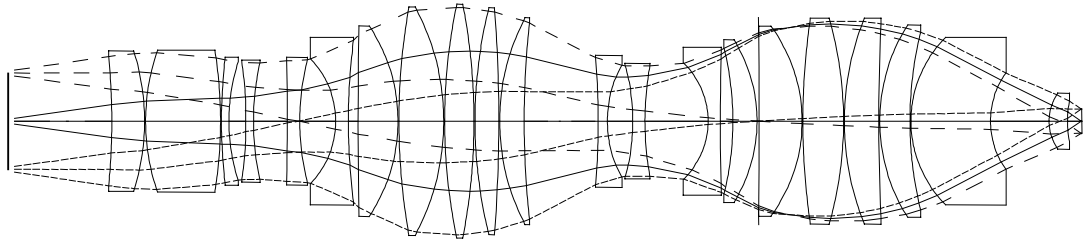
Figure 2.5.2 Lithographic objective from US Patent *5,805,344* (1998) with image side *NA* = 0.56, image field size 15 × 15 mm², working wavelength 248 nm, reduction ratio 0.25.

The development of polishing and measurement techniques allowed a decrease of number and of the size of components in the optical layout by using lens surfaces with an aspherical shape (aspheres). The design possibilities were widened as well by using catadioptric objectives, e.g. by combining reflective mirror surfaces and refractive lens elements. In the system shown in Figure 2.5.3. the plane mirror allows to produce a compact objective and the combination of a beam splitter and a concave mirror allows a reduction of astigmatism and chromatic aberrations.
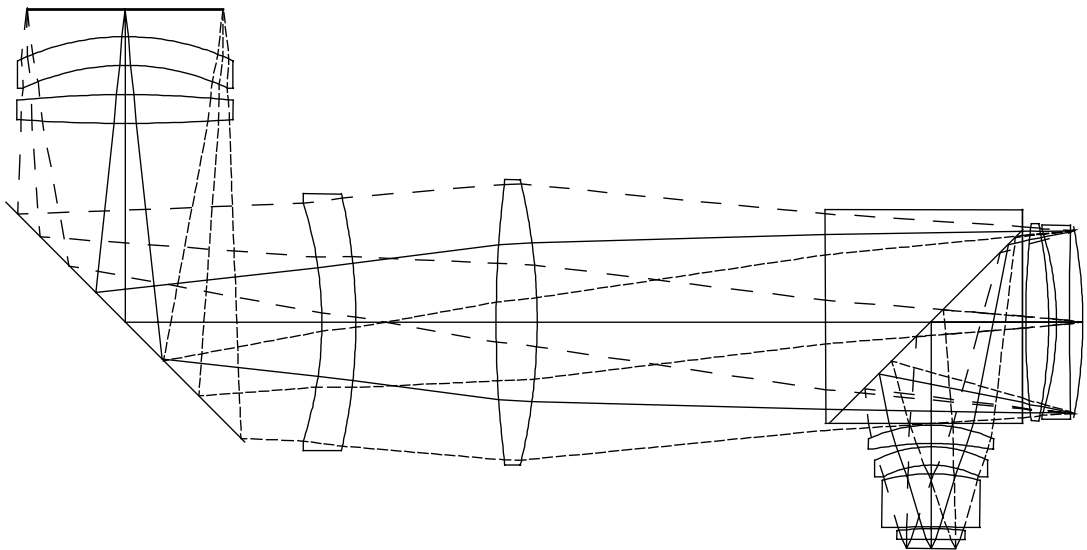
Figure 2.5.3 Lithographic objective from US Patent 4,953,960 (1990) with image side NA = 0.45, image field size 15 × 15 mm², working wavelength 248 or 193 nm, reduction ratio 0.25.

Recent breakthroughs in optical fabrication technology enable high-volume production of ultra-high-precision glass optics. Fused silica, a glass produced by melting crystal quartz, is the primary optical material used for 365-, 248- and 193-nm lithography. Calcium fluoride is used as a companion material to fused silica for achromatization at 193 nm and it is also used in areas of high flux because of its high laser damage resistance. Only this material can be used for optical systems working at 157 nm because of the high absorption of fused silica at this wavelength. However, usage of calcium fluoride is limited by its birefringence and inhomogeneity. These difficulties reflected on the design solution shown in Figure 2.5.4, which has small

number of lenses but has a disadvantage because of mirror obscuration. The induced birefringence in CaF_2 is a main subject of this thesis and discussed in Chapters 3-5.
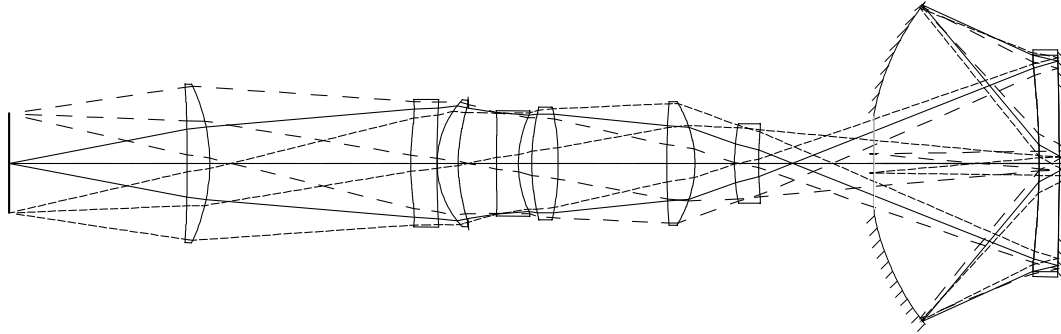
Figure 2.5.4 Lithographic objective from US Patent *6,757,051* Embodiment 1 (2002) with image side *NA* = 0.75, field size 20 × 20 mm², working wavelength 157 nm, reduction ratio 0.25.

It can be observed that, in parallel with the decreasing working wavelength, optical designers are vigorously developing systems having higher numerical apertures (from 0.2 in 1970s up to 0.9 nowadays). An example of such a system with NA=0.8 is shown in Figure 2.5.5. With the increase of NA and decreasing wavelength, different design challenges are encountered; in particular because of the shallow depth of focus, the distance between the surface of the last lens and the wafer should be controlled with high accuracy. The field size is also currently increasing in order to produce larger chips. This can be achieved either by optical design adaptation or by scanning object and image through the highly corrected objective field.
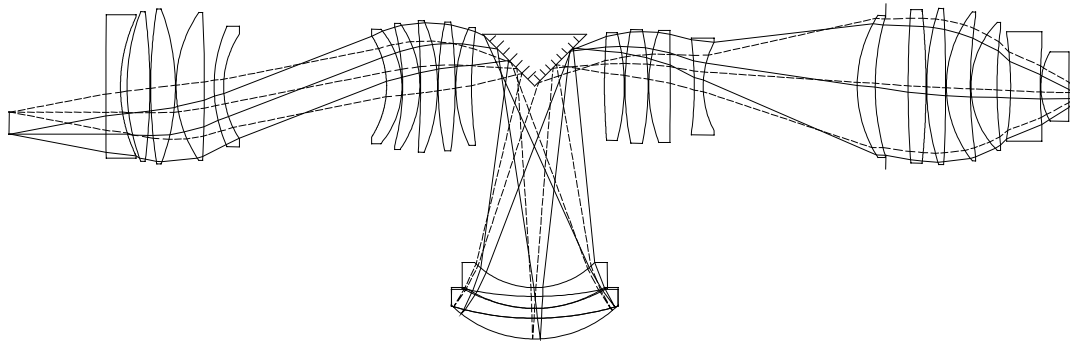
Figure 2.5.5 Lithographic objective from US Patent *6,757,051* Embodiment 5 (2002) with image side *NA* = 0.8, field size 15 × 15 mm², working wavelength 157 nm, reduction ratio 0.25.

The alternative for increasing NA is changing the refractive index of the medium in front of the wafer as it can be seen from relation (2.4.2). This immersion technique seems to be a very promising technology which can postpone or even make superfluous the 157 nm lithography generation.

Lithographers are also working on decreasing coefficients k_1 and k_2. Nowadays tool vendors and process developers are pushing k_1 to the value of 0.3 (very close to the theoretical value of 0.25) and k_2 to 1, which is usually achievable with good-quality objectives. Equation (2.4.5) shows explicitly that at the same NA and the same lens resolution, a shorter wavelength gives a larger depth of focus. From the viewpoint of lens resolution, this is the incentive for exploring shorter wavelengths, even when a longer wavelength seems adequate. Another observation is that a smaller value of k_1 increases the depth of focus quadratically. Since different resolution enhancement techniques are used such as phase-shift masks, better photoresists, improved process

control and off-axis illumination schemes, it is possible to achieve a smaller k_1 and extend the depth of focus.

Currently immersion lithography generations are under development. The next generation will be the Extreme Ultra Violet (EUV) lithography. This generation operates with a wavelength in the range of 10 to 14 nm (Xe-laser). There is no material that can be transparent at this wavelength and optical systems should consist of mirrors only. The number of mirrors should be minimized because the value of the reflectivity of a single reflector doesn't exceed 70%. In order to provide the designer with enough parameters to correct aberrations these mirrors should be extremely high-order aspheres. The example of this optical system is shown in Figure 2.5.6. The first operational EUV system is expected around the year 2010.
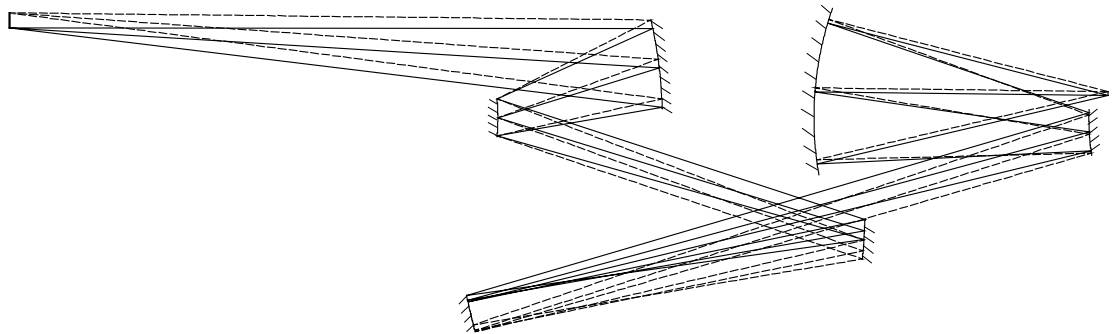
Figure 2.5.6 Lithographic objective from US Patent *5,815,310* (1998) with image side *NA* = 0.25, annular width of the field 1.5 mm, working wavelength 13 nm, reduction ratio 0.25.

Lithographers consider the possibility of X-ray lithography as well, but at the moment it is difficult to predict its future.

3. Spatially induced birefringence in cubic crystals, a theoretical analysis

3.1. Overview of the research on spatially induced birefringence

The phenomenon of birefringence in certain types of crystals has been known for more than three centuries. It was first discovered by Bartholinus, qualitatively explained by Huygens and marvelously described quantitatively by Fresnel. A firm foundation for the phenomenon of birefringence was obtained by applying Maxwell's laws to crystalline media with specific symmetry properties. In this classical description, cubic crystals do not show birefringence and, indeed, for most purposes they can effectively be considered as being isotropic.

It was Lorentz who first indicated the presence of anisotropy introduced by spatial dispersion (dependence dielectric constant on the ray direction) in cubic crystals as early as 1878 [12]. This observation was made again in Ref. [13] on the basis of a microscopic investigation of quadripolar transitions in crystals, and in Ref. [14] on the basis of macroscopic electrodynamics. The detailed analysis of this problem was carried out in the first edition of Ref. [15]. It was shown, among others, that cubic crystals possess seven optical axes (the three main crystallographic axes and the four body diagonals of the cubic crystallographic lattice). In this respect cubic crystals can be called heptaxial i.e. possessing seven optical axis.

A number of experimental and theoretical studies were carried out in the 1970's on the birefringence effect induced by spatial dispersion in semiconductors (see Ref. [15], Section 4.6.2). Because of the very small magnitude of the effect and the absence of any practical applications these investigations have not been done in much detail. However, recent publications [16][17] demonstrate the great practical importance of the phenomenon for the next generation of photolithography.

It was reported that the birefringence induced by spatial dispersion (BISD), sometimes also called intrinsic birefringence, has been measured and calculated for fluorides CaF_2 and BaF_2 in the ultraviolet part of the spectrum [16][17]. It was also shown that the magnitude of the BISD in these crystals is sufficiently large to cause serious problems when using CaF_2 for precision UV optical systems at wavelengths as short as 157 and perhaps 193 nm in the case of high numerical aperture.

The single-crystal fluorides such as calcium fluoride, barium fluoride and lithium fluoride are the only materials with sufficient transmissivity at 157 nm. Calcium fluorite CaF_2 is the most robust and highly developed of the fluorides; barium and lithium fluoride are highly hygroscopic and much more difficult to work. Moreover CaF_2 is a widely used material in optics because it is transparent in a very wide spectral range (from 0.13 to 10 microns). Nowadays, calcium fluoride crystals are grown by the so-called vacuum Stockbarger technique [18] in diameters up to about 350 mm and one crystal ingot for one lithographic lens needs about 90 days to grow. The crystal lattice of fluorite is shown in Figure 3.1.1. It has a face-centered structure of calcium ions with fluoride ions in every tetrahedral hole. Fluorides belong to cubic crystal class *m3m* (International notation) or O_h (Schoenflies notation).

Spatially induced birefringence in cubic crystals, a theoretical analysis
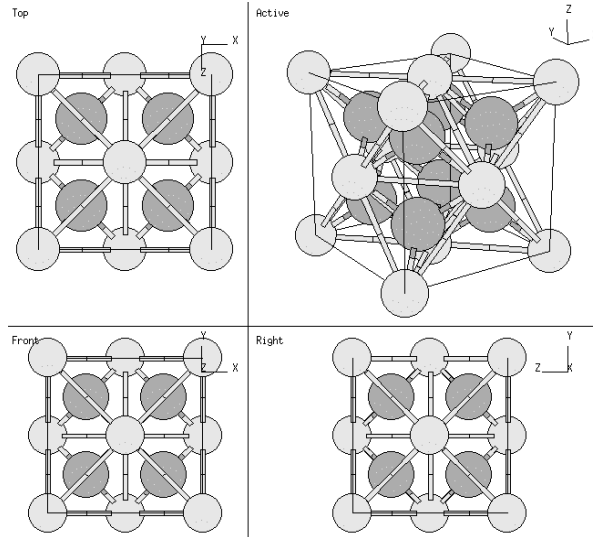
Figure 3.1.1 The crystal lattice structure of calcium fluorite.

3.2. Birefringence in crystalline media

The essence of the BISD phenomenon in cubic crystals is the dependence of the dielectric constant ε not only on the wave frequency (the wavelength) but also on the direction of the wave vector i.e. the direction of propagation of the rays in the media. An alternative formulation is the following: the polarization induced at some point of the space depends not only on the local field value in this point but also on the local field induced at the neighboring points. This effect should be taken into account especially when the wavelength is so short that the typical crystal lattice constant is not negligible anymore as compared with the wavelength, because in this case the anisotropic behavior of crystals, although still very small, becomes important. In other words it is necessary to regard the BISD effect when we use the UV-range for those crystals which can be considered isotropic in ordinary conditions. In practice, it leads to the possibility of the appearance of a pair of polarized rays after refraction on each surface, and the angular difference between them depends on the wavelength, thickness and shape of the lens. To each ray from the pair of rays, a particular refractive index of refraction should be attributed like in case of common birefringence and the crystal refracts light differently depending on how the incident light is polarized. Thus the index of refraction of the crystal depends on the light polarization and direction of light propagation.

In addition to the BISD another effect having similar nature occurs [19],[20]. When polishing crystal materials, such as calcium fluoride, the hardness of the material depends on the crystal orientation, thus the pressure at different points of the glass block is not constant. The stress produces an anisotropic and inhomogeneous optical medium where the magnitudes of the refraction indices vary at every point. This effect may result in a wavefront error and a change of the polarization state and it is called stress-induced birefringence. For cubic crystals the stress-birefringence figure is often a lobed structure with three high zones and three low zones when the crystal's {111} plane is perpendicular to the optical axis of the element [19].

Our goal is to find a proper description of the polarization of the light, refracted by cubic crystals, depending on the direction of propagation. We shall obtain the relationship for the polarization state of two bifurcated rays and the difference between their refraction indices. We will use the macroscopic electrodynamic

approach [15] to analyze the birefringence in crystals. The macroscopic Maxwell equations for the electromagnetic field quantities in a medium are written as

$$\left.\begin{array}{c} \text{rot } \mathbf{B} = \dfrac{1}{c}\dfrac{\partial \mathbf{D}}{\partial t} + \dfrac{4\pi}{c}\mathbf{j}_{ext} \\[2mm] \text{div } \mathbf{D} = 4\pi\rho_{ext} \\[2mm] \text{rot } \mathbf{E} = -\dfrac{1}{c}\dfrac{\partial \mathbf{B}}{\partial t} \\[2mm] \text{div } \mathbf{B} = 0. \end{array}\right\} \qquad (3.2.1)$$

Here $\mathbf{E}$ is the electric field strength, $\mathbf{D}$ and $\mathbf{B}$ are the electric and magnetic induction. The quantities $\mathbf{j}_{ext}$ and ρ_{ext} are the external current and charge densities which are sources of the external electromagnetic field. These equations are supplemented by the relation between the electric induction $\mathbf{D}$ and the electric field $\mathbf{E}$. This material equation can be written in the framework of macroscopic electrodynamics in the following general form

$$D_i(\mathbf{r},t) = \int_{-\infty}^{t} \mathrm{d}t' \int \mathrm{d}\mathbf{r}' \varepsilon_{ij}(t-t',\mathbf{r}-\mathbf{r}')E_j(\mathbf{r}',t'), \qquad (3.2.2)$$

where $\varepsilon_{ij}(t,\mathbf{r})$ is the dielectric tensor of the medium, and the Einstein summation convention has been used.

Here we have used the principle of causality according to which the induction at time t is only determined by the present field and the field at previous times $t' \le t$.

We Fourier transform the Eqs. (3.2.1) and (3.2.2) assuming that

$$E_i(\mathbf{r},t) = \int\int E_i(\omega,\mathbf{k})e^{i(\mathbf{kr}-\omega t)}\mathrm{d}\omega\,\mathrm{d}\mathbf{k}. \qquad (3.2.3)$$

For the other quantities we use the same notation as well. Then we obtain

$$\mathbf{D}(\omega,k) = -\frac{c}{\omega}\left(\mathbf{k}\times\mathbf{B}(\omega,\mathbf{k})\right), \qquad (3.2.4)$$

$$\mathbf{k}\cdot\mathbf{D}(\omega,k) = 0, \qquad (3.2.5)$$

$$\mathbf{B}(\omega,\mathbf{k}) = \frac{c}{\omega}\left(\mathbf{k}\times\mathbf{E}(\omega,\mathbf{k})\right), \qquad (3.2.6)$$

$$\mathbf{k}\cdot\mathbf{B}(\omega,k) = 0, \qquad (3.2.7)$$

and

$$D_i(\omega,\mathbf{k}) = \varepsilon_{ij}(\omega,\mathbf{k})E_j(\omega,\mathbf{k}), \qquad (3.2.8)$$

where summation over the index j, appearing twice, is assumed.

We can also introduce the inverse dielectric function matrix $\varepsilon_{ij}^{-1}(\omega,\mathbf{k})$ and write

$$E_i(\omega,\mathbf{k}) = \varepsilon_{ij}^{-1}(\omega,\mathbf{k})D_j(\omega,\mathbf{k}). \qquad (3.2.9)$$

Writing Eqs. (3.2.4)-(3.2.7) we have used the fact that in our case external current and charges are absent. The spatial dispersion is determined by the parameter $a\mathbf{k}$ or by the somewhat more descriptive parameter a/λ, where a is a characteristic dimension (the radius of "the region of influence", radius of molecular action, etc.) and λ is the length of the electromagnetic wave. In a condensed non-metallic medium the radius a is about the order of the lattice constant. Therefore, the parameter a/λ is very small, even in the optical or ultraviolet range of the electromagnetic spectrum.

Eliminating the magnetic induction $\mathbf{B}$ from the Eqs. (3.2.4) - (3.2.7) we obtain the expression

Spatially induced birefringence in cubic crystals, a theoretical analysis

$$\mathbf{D} = -\frac{c^2}{\omega^2}[\mathbf{k} \times (\mathbf{k} \times \mathbf{E})] = \frac{c^2}{\omega^2}[k^2 \mathbf{E} - \mathbf{k} \cdot (\mathbf{k} \cdot \mathbf{E})], \tag{3.2.10}$$

and, substituting the Eq. (3.2.8) into (3.2.10), we find

$$\left[\frac{\omega^2}{c^2}\varepsilon_{ij}(\omega, \mathbf{k}) - k^2\left(\delta_{ij} - \frac{k_i k_j}{k^2}\right)\right]E_j(\omega, \mathbf{k}) = 0. \tag{3.2.11}$$

If we use the matrix $\varepsilon_{ij}^{-1}(\omega, \mathbf{k})$ we obtain

$$\left[\frac{\omega^2}{c^2}\delta_{ij} - k^2\left(\delta_{il} - \frac{k_i k_l}{k^2}\right)\varepsilon_{lj}^{-1}(\omega, \mathbf{k})\right]D_j(\omega, \mathbf{k}) = 0. \tag{3.2.12}$$

These homogeneous systems of algebraic equations have nontrivial solutions $\mathbf{E}(\omega, k) \neq 0$ and $\mathbf{D}(\omega, k) \neq 0$, only if the corresponding determinants vanish

$$\left|\frac{\omega^2}{c^2}\varepsilon_{ij}(\omega, \mathbf{k}) - k^2\left(\delta_{ij} - \frac{k_i k_j}{k^2}\right)\right| = 0, \tag{3.2.13}$$

and

$$\left|\frac{\omega^2}{c^2}\delta_{ij} - k^2\left(\delta_{il} - \frac{k_i k_l}{k^2}\right)\varepsilon_{lj}^{-1}(\omega, \mathbf{k})\right| = 0. \tag{3.2.14}$$

The dispersion equations (3.2.13) and (3.2.14) give the relation between ω and $\mathbf{k}$ for the electromagnetic normal waves (or eigenwaves) in a given medium for $\omega_l = \omega_l(\mathbf{k})$, where the subscript l corresponds to the given normal wave. For these normal waves, we can write the wave vector $\mathbf{k}$ in the form

$$\mathbf{k} = \frac{\omega}{c}n(\omega, \mathbf{s})\mathbf{s}, \tag{3.2.15}$$

where $\mathbf{s}$ is the unit vector in the direction $\mathbf{k}$ and $n(\omega, \mathbf{s})$ is the corresponding refraction index. The dispersion equation (3.2.13) can be conveniently written in the form

$$\left|n^2(\omega, \mathbf{s})(\delta_{ij} - s_i s_j) - \varepsilon_{ij}\left(\omega, \frac{\omega}{c}n(\omega, \mathbf{s})\mathbf{s}\right)\right| = \varepsilon_{ij}s_i s_j n^4 - \left[(\varepsilon_{ij}s_i s_j)\varepsilon_{ll} - \varepsilon_{il}\varepsilon_{lj}s_i s_j\right]n^2 + |\varepsilon_{ij}| = 0. \tag{3.2.16}$$

This is the fundamental equation of crystal optics. In classical crystal optics $\varepsilon_{ij} = \varepsilon_{ij}(\omega)$ and (3.2.16) becomes quadratic with respect to n^2 and this reduced form is frequently called Fresnel's equation.

For our purpose, it is more convenient to investigate the dispersion equation (3.2.14) because we can use the property that the electric induction $\mathbf{D}$ is always transverse for normal waves. This means that we can choose the coordinate system whose z-axis is directed along $\mathbf{s}$ and then the vector $\mathbf{D}$ will have only two components D_x and D_y. By setting $s_1 = s_2 = 0$ and $s_3 = 1$ the wave equation and the dispersion equation have the following form

$$m^2 D_\alpha = \varepsilon_{\alpha\beta}^{-1}D_\beta, \tag{3.2.17}$$

$$\left|m^2\delta_{\alpha\beta} - \varepsilon_{\alpha\beta}^{-1}\right| = m^4 - \left(\varepsilon_{11}^{-1} + \varepsilon_{22}^{-1}\right)m^2 + \varepsilon_{11}^{-1}\varepsilon_{22}^{-1} - \left(\varepsilon_{12}^{-1}\right)^2 = 0, \tag{3.2.18}$$

where we introduced the notation

$$\frac{1}{n^2} = m^2; \quad \alpha, \beta = 1, 2. \tag{3.2.19}$$

The dispersion equation (3.2.18) has two roots for the quantity m^2

$$m_{1,2}^2 = \frac{\varepsilon_{11}^{-1} + \varepsilon_{22}^{-1}}{2} \pm \frac{1}{2}\sqrt{\left(\varepsilon_{11}^{-1} - \varepsilon_{22}^{-1}\right)^2 - 4\left(\varepsilon_{12}^{-1}\right)^2}. \tag{3.2.20}$$

and, consequently, we are led to two mutually orthogonal vectors $\mathbf{D_1}$ and $\mathbf{D_2}$. As is well known from Ref. [15] and [21], the existence of two values of the refractive index n for a given direction of the wave vector $\mathbf{k}$ is the origin of the appearance of the birefringence effect. The dispersion equation (3.2.18) has a multiple root $m_1^2 = m_2^2$ if

$$\left(\varepsilon_{11}^{-1} - \varepsilon_{22}^{-1}\right)^2 - 4\left(\varepsilon_{12}^{-1}\right)^2 = 0 \tag{3.2.21}$$

and the birefringence is absent in this case. Also, it is well known from Ref. [15] and [21] that in the case of classical crystal optics, i.e., for $\varepsilon_{ij} = \varepsilon_{ij}(\omega)$, the multiple root for m exists for every direction of $\mathbf{k}$ only in the case of cubic crystals. For all other crystals with a lower symmetry, birefringence is absent only for the wave with the wave vector $\mathbf{k}$ oriented along the principal optical axis. For hexagonal, tetragonal or trigonal crystals there is one such axis and these crystals are called uniaxial. For the three remaining crystal systems, namely the orthorhombic, monoclinic and triclinic ones, there are two privileged normal wave directions for which there is no birefringence and the crystals are called biaxial. As shown in what follows, the situation is more complicated when the spatial dispersion is taken into account, i.e., if the dielectric function matrix depends on both the frequency ω and the wave vector $\mathbf{k}$.

3.3.   Spatial dispersion of cubic crystals

We first write the inverse dielectric matrix for cubic crystals in the case of small spatial dispersion in the form

$$\varepsilon_{ij}^{-1}(\omega, \mathbf{k}) = \varepsilon_{ij}^{-1}(\omega)\delta_{ij} + \beta_{ijlm}(\omega)k_l k_m, \tag{3.3.1}$$

or as

$$\varepsilon_{ij}^{-1}(\omega, \mathbf{k}) = \varepsilon_{ij}^{-1}(\omega)\delta_{ij} + \beta_{ijlm}(\omega)\frac{\omega^2}{c^2}n^2 s_l s_m . \tag{3.3.2}$$

The fourth-rank tensor β_{ijlm} has only three independent and non-zero components for cubic crystals with symmetry classes O, T_d and O_h [15],[22]. These are

$$\beta_1 = \beta_{xxxx} = \beta_{yyyy} = \beta_{zzzz}, \tag{3.3.3}$$

$$\beta_2 = \beta_{xxzz} = \beta_{yyxx} = \beta_{zzyy} = \beta_{zzxx} = \beta_{xxyy} = \beta_{yyzz}, \tag{3.3.4}$$

$$\beta_3 = \beta_{xyxy} = \beta_{yzyz} = \beta_{zxzx}. \tag{3.3.5}$$

Using these expressions the matrix elements of ε_{ij}^{-1} can be written as

$$\varepsilon_{xx}^{-1} = \varepsilon^{-1}(\omega) + \left(\frac{\omega}{c}n\right)^2 \left[\beta_1 s_x^2 + \beta_2\left(s_y^2 + s_z^2\right)\right], \tag{3.3.6}$$

$$\varepsilon_{xy}^{-1} = 2\left(\frac{\omega}{c}n\right)^2 \beta_3 s_x s_y, \tag{3.3.7}$$

$$\varepsilon_{yy}^{-1} = \varepsilon^{-1}(\omega) + \left(\frac{\omega}{c}n\right)^2 \left[\beta_2\left(s_x^2 + s_z^2\right) + \beta_1 s_y^2\right], \tag{3.3.8}$$

Spatially induced birefringence in cubic crystals, a theoretical analysis

$$\varepsilon_{xz}^{-1} = 2\left(\frac{\omega}{c}n\right)^2 \beta_3 s_x s_z \ , \tag{3.3.9}$$

$$\varepsilon_{zz}^{-1} = \varepsilon^{-1}(\omega) + \left(\frac{\omega}{c}n\right)^2 \left[\beta_2\left(s_x^2 + s_y^2\right) + \beta_1 s_z^2\right] \ , \tag{3.3.10}$$

$$\varepsilon_{yz}^{-1} = 2\left(\frac{\omega}{c}n\right)^2 \beta_3 s_y s_z \ . \tag{3.3.11}$$

The factor two in the expressions for ε_{xy}^{-1}, ε_{xz}^{-1} and ε_{yz}^{-1} is due to the summation in Eq. (3.3.1). Equations (3.3.1)– (3.3.11) allow us to write the expression for the inverse dielectric matrix in the form

$$\varepsilon_{ij}^{-1}\left(\omega, \frac{\omega}{c}n\mathbf{s}\right) = \left(\varepsilon^{-1}(\omega) + \frac{\omega^2}{c^2}n^2\beta_2\right)\delta_{ij} + \frac{\omega^2}{c^2}n^2\tilde{\beta}s_i^2\delta_{ij} + 2\frac{\omega^2}{c^2}n^2\beta_3 s_i s_j \ , \tag{3.3.12}$$

where

$$\tilde{\beta} = \beta_1 - \beta_2 - 2\beta_3 \ . \tag{3.3.13}$$

The first term in the right hand side of Eq. (3.3.12) is the isotropic contribution, the second one is anisotropic, but it is expressed in terms of a diagonal matrix; the last term is purely longitudinal. If we rewrite the wave equation (3.2.14)

$$\left[\frac{\delta_{ij}}{n^2(\omega, \mathbf{s})} - \left(\delta_{il} - s_i s_l\right)\varepsilon_{lj}^{-1}\left(\omega, \frac{\omega}{c}n\mathbf{s}\right)\right]D_j\left(\omega, \frac{\omega}{c}n\mathbf{s}\right) = 0 \tag{3.3.14}$$

it follows after some simple algebra that the longitudinal part of ε_{ij}^{-1} disappears from this equation due to the prefactor $\left(\delta_{il} - s_i s_l\right)$, because the multiplication of this prefactor with the longitudinal part yields zero.

We will solve Eq. (3.3.14) with the aid of perturbation theory and rewrite this equation as

$$\left(L_0 + L_1\right)_{ij} D_j = \rho(\omega, \mathbf{s})\delta_{ij} D_j \tag{3.3.15}$$

and

$$\rho(\omega, \mathbf{s}) = \rho_0(\omega) + \rho_1(\omega, \mathbf{s}) \ , \tag{3.3.16}$$

where

$$\rho(\omega, \mathbf{s}) = \frac{1}{n^2(\omega, \mathbf{s})} \tag{3.3.17}$$

is the eigenvalue of this equation which should be calculated up to the first order perturbations described by the perturbation operator L_1. L_1 has the form

$$\left(L_1\right)_{ij} = \frac{\omega^2}{c^2}n^2(\omega, \mathbf{s})\tilde{\beta}s_i^2\delta_{ij} - \frac{\omega^2}{c^2}n^2(\omega, \mathbf{s})\tilde{\beta}s_i s_j^3 \ . \tag{3.3.18}$$

In the framework of perturbation theory, we can change the value $n^2(\omega, \mathbf{s})$ in Eq. (3.3.18) into $n_0^2(\omega)$ defined by the zero-order approximation. This zero-order perturbation is defined by the equation

$$\left(L_0\right)_{ij} D_j^0 = \rho_0(\omega)D_i^0 \ , \tag{3.3.19}$$

where

$$\left(L_0\right)_{ij} = \left(\varepsilon^{-1}(\omega) + \frac{\omega^2}{c^2}n_0^2\beta_2\right)\left(\delta_{ij} - s_i s_j\right) \tag{3.3.20}$$

and, consequently, Eq. (3.3.19) for the zero-order approximation can be written as

Spatially induced birefringence in cubic crystals, a theoretical analysis

$$\left[\left(\varepsilon^{-1}(\omega) + \frac{\omega^2}{c^2} n_0^2 \beta_2\right)(\delta_{ij} - s_i s_j)\right]D_j^0 = \rho_0(\omega)D_i^0. \tag{3.3.21}$$

By using Eq. (3.2.5) this equation reduces to the wave equation for isotropic media, which has the multiple root for $\rho_0(\omega)$ equal to

$$\rho_0(\omega) = \frac{1}{n_0^2(\omega)} = \varepsilon^{-1}(\omega) + \frac{\omega^2}{c^2} n_0^2(\omega)\beta_2. \tag{3.3.22}$$

Moreover, in the framework of macroscopic electrodynamics we can neglect the second term in the right part of (3.3.22) because there are no possible experiments which can help us to distinguish the terms $\varepsilon^{-1}(\omega)$ and $\frac{\omega^2}{c^2} n_0^2(\omega)\beta_2$. This means that for the refraction index $n_0(\omega)$ in the zero-order approximation we can write

$$n_0^2(\omega) = \varepsilon(\omega), \tag{3.3.23}$$

where

$$\varepsilon(\omega) = \left(\varepsilon^{-1}(\omega)\right)^{-1}. \tag{3.3.24}$$

The existence of the multiple root of $\rho_0(\omega)$ in the zero-order approximation tells us that the system of equations (3.3.15) and (3.3.16) has a degenerate kernel [23] and we should use for the calculation of the first order correction to $\rho_1(\omega,\mathbf{s})$ a so-called secular equation. This equation will give also the two correct values of $\tilde{D}_i^0(\omega, n(\omega,\mathbf{s}))$ resulting from the removal of the degeneracy due to the perturbation operator L_1. If we write the first order correction $\rho_1(\omega,\mathbf{s})$ as

$$\rho_1(\omega,\mathbf{s}) = \frac{\omega^2}{c^2} n_0^2(\omega)\tilde{\beta}\tilde{\rho}_1(\mathbf{s}), \tag{3.3.25}$$

the secular equation will have the form

$$\left(s_i^2 \delta_{ij} - s_i s_j^3\right)e_j(\mathbf{s}) = \tilde{\rho}_1(\mathbf{s})e_i(\mathbf{s}), \tag{3.3.26}$$

where we introduced the unit vector $\mathbf{e}$ in the direction of $\tilde{\mathbf{D}}^0(\mathbf{s})$. The pair of eigenmodes $(e_1(\mathbf{s}), e_2(\mathbf{s}))$ has been chosen in such a way that in this basis the 2×2 matrix associated with the operator L_1 becomes diagonal. Because the vector $\tilde{\mathbf{D}}^0(\mathbf{s})$ is orthogonal to the vector $\mathbf{s}$, when the matrix is computed, the contribution of the terms $s_i s_j^3$ vanishes and Eq. (3.3.26) can be replaced by

$$s_i^2 e_i(\mathbf{s}) = \tilde{\rho}_1(\mathbf{s})e_i(\mathbf{s}). \tag{3.3.27}$$

Because of its complexity, the computation has been done by using computer algebra software. The two solutions for $\tilde{\rho}_1(\mathbf{s})$ i.e. the diagonal element of the matrix mentioned above turn out to be the roots of the quadratic equation

$$\tilde{\rho}_1^2(\mathbf{s}) - 2(s_x^2 s_y^2 + s_x^2 s_z^2 + s_y^2 s_z^2)\tilde{\rho}_1(\mathbf{s}) + 3s_x^2 s_y^2 s_z^2 = 0. \tag{3.3.28}$$

These solutions are

$$\tilde{\rho}_1^{(1,2)}(\mathbf{s}) = (s_x^2 s_y^2 + s_x^2 s_z^2 + s_y^2 s_z^2) \pm \sqrt{(s_x^2 s_y^2 + s_x^2 s_z^2 + s_y^2 s_z^2)^2 - 3s_x^2 s_y^2 s_z^2}. \tag{3.3.29}$$

Note that the equation for $\tilde{\rho}_1(\mathbf{s})$ has only one solution for the seven directions of the propagation vector $\mathbf{s}$, mentioned above, i. e., the three main crystallographic axes and the four body diagonals of the cube.

Spatially induced birefringence in cubic crystals, a theoretical analysis

We can also obtain the expression for the eigenmodes of Eq. (3.3.27). The components of the eigenmode $e_2(\mathbf{s})$, which correspond to the eigenvalue $\tilde{\rho}_1^{(2)}(\mathbf{s})$, the one with the minus sign in front of the square root, have the following form

$$e_{2z}(\mathbf{s}) = \frac{1}{\sqrt{2}}\sqrt{s_x^2 + s_y^2 + \frac{s_x^2 s_y^2\left(s_x^2 + s_y^2\right) - \left(s_x^4 + s_y^4\right)s_z^2}{r}}\,, \qquad (3.3.30)$$

$$e_{2x}(\mathbf{s}) = e_{2z}(\mathbf{s})\frac{s_y^2\left(s_z^2 - s_x^2\right) + r}{s_x s_z\left(s_x^2 - s_y^2\right)}\,, \qquad (3.3.31)$$

$$e_{2y}(\mathbf{s}) = e_{2z}(\mathbf{s})\frac{s_x^2\left(s_z^2 - s_y^2\right) + r}{s_y s_z\left(s_y^2 - s_x^2\right)}\,, \qquad (3.3.32)$$

where r is given by

$$r = \sqrt{(s_x^2 s_y^2 + s_x^2 s_z^2 + s_y^2 s_z^2)^2 - 3s_x^2 s_y^2 s_z^2}\,. \qquad (3.3.33)$$

For certain directions $\mathbf{s}$ zero denominators appear and then these expressions cannot be used directly. When Eqs. (3.3.30)-(3.3.33) must be used for a direction which leads to zero denominators, use of a non-singular direction very close to the singular one gives sufficient accuracy for practical purposes. Analytical expressions can also be derived for these special cases. For instance, for $s_x > 0$ and $s_y > 0$, but s_x is very small we obtain

$$e_{2x}(\mathbf{s}) = -\sqrt{\frac{1}{s_z^2}}s_z\,, \quad e_{2y}(\mathbf{s}) = \frac{s_x\sqrt{\frac{1}{s_z^2}}s_z}{2\sqrt{1 - s_z^2}}\,, \quad e_{2z}(\mathbf{s}) = \frac{1}{2}s_x\sqrt{\frac{1}{s_z^2}}\,. \qquad (3.3.34)$$

The components of the eigenmode $e_1(\mathbf{s})$ corresponding to the eigenvalue $\tilde{\rho}_1^{(1)}(\mathbf{s})$ can be obtained from the equation

$$e_1(\mathbf{s}) = e_2(\mathbf{s}) \times \mathbf{s}\,. \qquad (3.3.35)$$

Our first order correction to the eigenvalue $\tilde{\rho}_1(\mathbf{s})$ coincides with that obtained by Burnett et al in [17]. An alternative approach that leads to relations that are equivalent to Eqs. (3.3.30-35) is discussed in [24].

If we define the variation of the birefringence with propagation direction according to Eq. (22) in [17] as

$$\Delta\tilde{\rho}_1(\mathbf{s}) = \tilde{\rho}_1^{(1)}(\mathbf{s}) - \tilde{\rho}_1^{(2)}(\mathbf{s}) = 2\sqrt{(s_x^2 s_y^2 + s_x^2 s_z^2 + s_y^2 s_z^2)^2 - 3s_x^2 s_y^2 s_z^2}\,, \qquad (3.3.36)$$

this value will have the same sign for every direction. The origin for a possible change of the sign of the birefringence variation shown in Figure 3.3.3 is related to the behavior of the eigenmodes $e_{1,2}(\mathbf{s})$. This fact can be easily understood from Figure 3.1.1.

Here and below we introduce a notation used in crystallography implying that:

- (hkl) - parenthesis designate a crystal face or a set of parallel planes throughout a crystal lattice.
- [uvw] - square brackets designate a direction in the lattice from the origin to a point.
- {hkl} - braces designate a set of faces that are equivalent by the symmetry of the crystal. The set of face planes results in the crystal form. For instance {100} in the cubic crystals includes (100), (010), (001), and opposite ($\bar{1}00$), ($0\bar{1}0$) and ($00\bar{1}$).

Spatially induced birefringence in cubic crystals, a theoretical analysis

- <uvw> - angle brackets designate a group of symmetry equivalent directions. <100> in the cubic crystals includes [100], [010], [001] and opposite directions; <110> includes [110], [101], [011] and opposite directions.
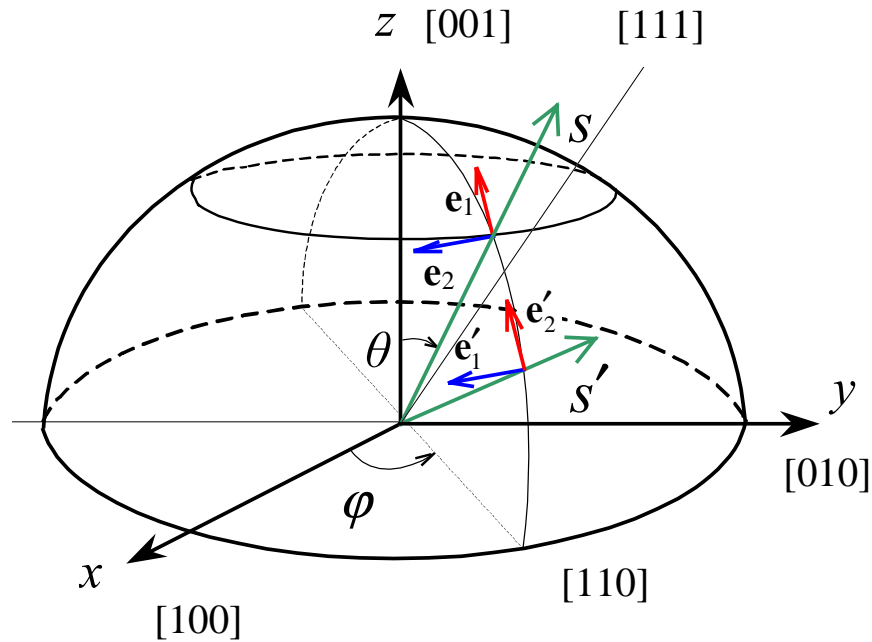
Figure 3.3.1 Behavior of the eigenvectors in the ($\overline{1}10$) -diagonal plane of an elementary cubic cell.

In Figure 3.3.1 we show the behavior of the eigenmodes $e_{1,2}(\mathbf{s})$ for two propagation directions in the diagonal plane ($\overline{1}10$) of the cubic cell containing the [001], [111] and [110] directions. We can see that the eigenmode $e_1(\mathbf{s})$ corresponding to the larger value of $\tilde{\rho}_1(\mathbf{s})$ lies in the plane ($\overline{1}10$) for the directions above the axis [111]. The eigenmode $e_2(\mathbf{s})$ is normal to this plane. The situation is reverse for the directions below the axis [111]. Here the eigenmode $e_2'(\mathbf{s}')$ lies in the plane ($\overline{1}10$). This means that, if we consider the difference of the refraction indices between one wave polarized in the ($\overline{1}10$) plane and on other normal to this plane, this difference will have an opposite sign for directions above and below axis [111].
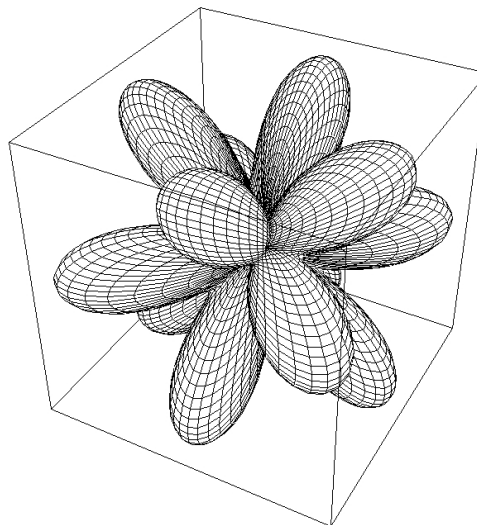
Figure 3.3.2 Distribution of the BISD in the cubic crystal.

The directional distribution of the BISD magnitude in the cubic crystal is shown in Figure 3.3.2. It can be seen that the birefringence in the cubic crystal has 12 maxima in <110> directions and 14 minima in <100> and <111> directions i.e. the cubic crystal has seven non-birefringent axis and can be called heptaaxial.

Finally the value of linear birefringence in spherical coordinate system shown on Figure 3.3.1 can be written as

$$\Delta n(\omega, \mathbf{k}) \sim \sin^2 \theta \sqrt{\frac{1}{16} \cos^4 \theta \left(7 + \cos 4\phi\right)^2 + \frac{1}{4} \sin^4 2\phi + \frac{1}{4} \cos^2 \theta \sin^2 2\phi \left(\cos 4\phi - 5\right)}. \quad (3.3.37)$$
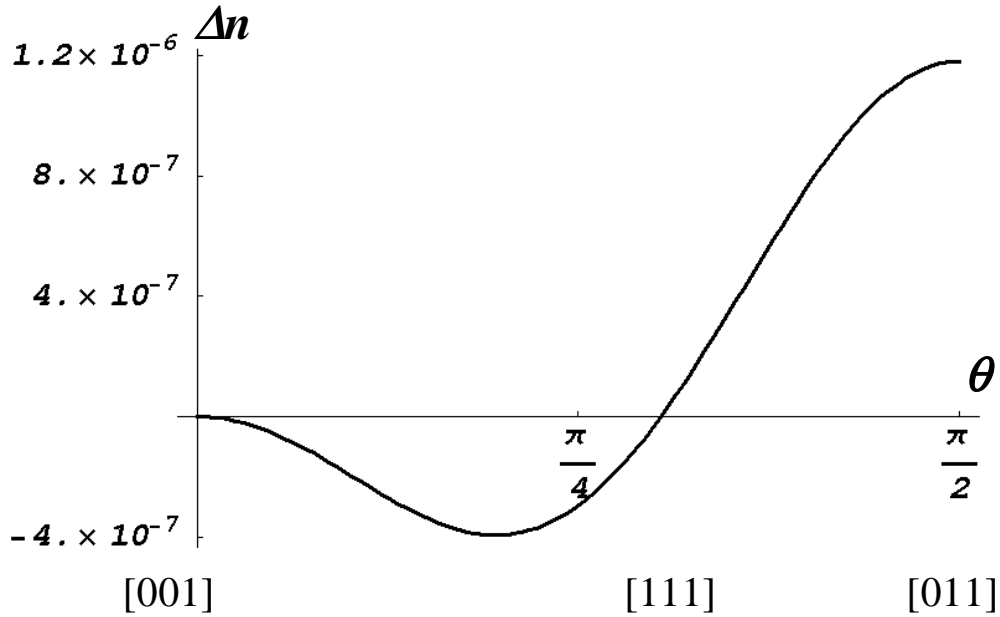
Figure 3.3.3 Behavior of the linear birefringence in ($\overline{1}10$) plane.

Figure 3.3.3 shows the behavior of the linear birefringence in the distinctive case of ($\overline{1}10$) plane. In this case we show the difference of the values indices of refraction for the polarization normal to the ($\overline{1}10$) plane and lying in the ($\overline{1}10$) plane depending on the value of θ. It can be seen that birefringence value has a main maximum in the <110> directions and secondary maximum between the <001> and <111> directions (in the <211> direction). A sign change occurs when the propagation direction passes through the <111> direction.

3.4.   Conclusions

In this chapter we have derived an expression for the eigenpolarizations and the linear birefringence value in the case of BISD in cubic crystals for an arbitrary ray direction. From this expression it followed that cubic crystals possess seven optical axis with respect to the BISD effect. The angular dependence of the magnitude of the effect has been analyzed. These data, supplemented with the reported measured magnitude of the effect, cause a serious anxiety regarding the use of cubic crystals in DUV lithography. This concern should be further investigated in more detail by modeling the BISD effect in the optical design software, which allows us to estimate the damage of the effect for the optical resolution.

4. Analysis of spatial dispersion in optical design

4.1.   Description of polarization in optical design

The state of polarization is one of the most important characteristics of an optical beam because many processes involving light depend on its polarization. If light propagates through a medium, the state of polarization is very sensitive to the optical properties of the medium as well. The fact that the optical properties of media may affect polarization offers great opportunities in many areas including biology, chemistry, physics and materials science, but it can also cause undesirable effects. For this reason, in optics it is important to precisely determine the state of polarization and its evolution on propagation through an optical system.

The state of polarization can be specified by the relative amplitudes of two orthogonal polarization components and the phase difference (retardation) between them. We limit ourselves here to fully polarized light.

When we consider optically anisotropic materials, such as crystals, the phase velocity of propagation generally depends on the direction of propagation and on the polarization state. The propagation directions for which the phase velocity is independent of the state of linear polarization are called optical axes. For any other propagation direction the polarization of a wave is defined with the aid of two orthogonal eigenaxes perpendicular to the propagation vector. These eigenstates of polarization are linear states which have refractive indices determined by the propagation direction and the crystal's dielectric tensor. Light polarized in an eigenstate propagates through an anisotropic material with unchanging polarization, but light having any other polarization state changes its polarization state with distance during the beam propagation. When the direction of light propagation coincides with an optical axis, the eigenpolarizations are degenerate, and an optical beam with any state of polarization propagates with refractive index n_o. For light propagating in other directions, one eigenpolarization has refractive index n_o and for other propagation directions refractive index takes on values between n_o and n_e according direction of propagation (for classical anisotropy see [25] and [26], for spatially induced anisotropy see Chapter 3).

The propagation of a monochromatic electromagnetic wave through an anisotropic material implies the propagation in the form of two eigenstates $\mathbf{D}'$ and $\mathbf{D}''$, linear and orthogonal, whose orientations are determined by the previous considerations. Propagation through the medium introduces the phases δ' and δ'', respectively equal to $2\pi n'd/\lambda$ and $2\pi n''d/\lambda$, where n' and n'' are the principal refraction indices along the direction of the propagation, d is the thickness of the material traversed along the same direction and the difference $\Delta n = n' - n''$ corresponds to a linear birefringence. In terms of linear algebra the traversal of the material is described by an operator which acts on the incident vectors $\mathbf{D}'_i$ and $\mathbf{D}''_i$, and it supplies us with the outgoing vectors $\mathbf{D}'_t$ and $\mathbf{D}''_t$ such that:

$$\begin{cases} \mathbf{D}'_t = e^{i\delta'}\mathbf{D}'_i \\ \mathbf{D}''_t = e^{i\delta''}\mathbf{D}''_i \end{cases}. \qquad (4.1.1)$$

The states of polarization $\mathbf{D}'_t$ and $\mathbf{D}''_t$ are respectively identical to the states $\mathbf{D}'_i$ and $\mathbf{D}''_i$, they simply have a phase difference.

Two allowed orthogonal linearly polarized waves propagate with differing phase velocities for a given incident wave vector **k**. Generally, one of the two possible waves exhibits "extraordinary" behavior and the wave vector and ray (Poynting) vector directions differ. In addition, the phase velocity $\mathbf{v_p}$, polarization orientation, and ray vector of each wave change with the wave vector direction. For each allowed wave, the electric field **E** is not parallel to the displacement vector **D** (which defines polarization orientation) and, therefore, the ray vector **S** is not parallel to the wave vector **k** as shown in Figure 4.1.1. The angle between **D** and **E** is the same as the angle between **k** and **S**. Furthermore, for each wave $\mathbf{D} \perp \mathbf{k} \perp \mathbf{H}$ and $\mathbf{E} \perp \mathbf{S} \perp \mathbf{H}$, forming orthogonal sets of vectors. The vectors **D**, **E**, **k**, and **S** are coplanar for each wave. Here and below we consider the orthogonal vector pair (**D**, **k**). The phase advance of the wave along the vector **k** then has to be projected on the ray direction **S**.
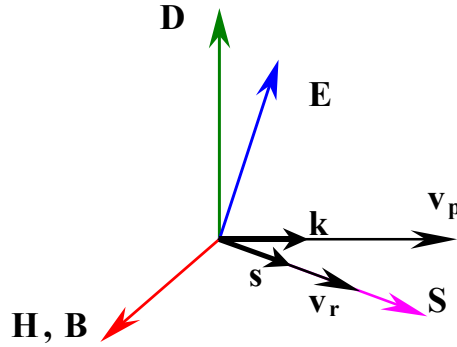
Figure 4.1.1 Relationship between various vectors used in the discussion of the propagation of light in an anisotropic medium. The Poynting vector S is orthogonal to both E and H because H is normal to the plane formed by D, E and k. However, unlike the case of an isotropic medium, S is not parallel to k.

It was shown that the BISD value can be calculated for any specified ray direction. The effect can be integrated through the entire optical system by use of the so-called Jones calculus [27]. For each ray along its path the Jones rotation and retarder matrices can be defined. A two-element Jones vector is the column vector formed by the two electrical vector components D_x and D_y

$$\mathbf{J} = \begin{bmatrix} D_x \\ D_y \end{bmatrix} = \begin{bmatrix} |D_x| e^{i\delta_x} \\ |D_y| e^{i\delta_y} \end{bmatrix} = e^{i(\delta_x + \delta_y)/2} \begin{bmatrix} |D_x| e^{i\Delta/2} \\ |D_y| e^{-i\Delta/2} \end{bmatrix}, \qquad (4.1.2)$$

where $\Delta = \delta_x - \delta_y$ is the phase lag.

The Jones matrix is a 2×2 transfer matrix used for transferring Jones vectors. The retarder matrix is a Jones matrix which is used to modify the optical phase of the two orthogonal field components due to the different indices of refraction in the two directions, $\Delta n'$ and $\Delta n''$. If the addition in phase for each component given by the retarder matrix is $\hat{\mathbf{J}}_R$, then

$$\mathbf{J}' = \hat{\mathbf{J}}_R \mathbf{J} . \qquad (4.1.3)$$

The Jones matrix for a linear polarization element of thickness d is

$$\hat{\mathbf{J}}_R = \begin{pmatrix} e^{i2\pi n' d/\lambda} & 0 \\ 0 & e^{i2\pi n'' d/\lambda} \end{pmatrix} = e^{i2\pi d \frac{(n'+n'')}{2\lambda}} \begin{pmatrix} e^{i2\pi \Delta n d/\lambda} & 0 \\ 0 & e^{-i2\pi \Delta n d/\lambda} \end{pmatrix}, \qquad (4.1.4)$$

where $\Delta n = n' - n''$ is the linear birefringence in the plane perpendicular to the direction of propagation of the beam, and

$$\delta = \frac{2\pi\Delta n d}{\lambda} \tag{4.1.5}$$

is the retardation (the phase difference).

If an optical element is rotated by an angle θ about the optical axis, a new Jones matrix $\hat{\mathbf{J}}'$ is derived from the original matrix $\hat{\mathbf{J}}$ by applying 2×2 rotator matrices

$$R(\theta) = \begin{bmatrix} \cos\theta & \sin\theta \\ -\sin\theta & \cos\theta \end{bmatrix}, \tag{4.1.6}$$

$$\hat{\mathbf{J}}' = R(-\theta) \cdot \hat{\mathbf{J}} \cdot R(\theta). \tag{4.1.7}$$

Note that

$$R(\theta_1)\, R(\theta_2) = R(\theta_1 + \theta_2). \tag{4.1.8}$$

In general, a linear retarder has the Jones matrix

$$\hat{\mathbf{J}}_R = \begin{bmatrix} \cos\dfrac{\delta}{2} + i\cos 2\theta \sin\dfrac{\delta}{2} & i\sin 2\theta \sin\dfrac{\delta}{2} \\ i\sin 2\theta \sin\dfrac{\delta}{2} & \cos\dfrac{\delta}{2} - i\cos 2\theta \sin\dfrac{\delta}{2} \end{bmatrix}. \tag{4.1.9}$$

For the optical system with k components we have

$$\mathbf{J}' = \prod_{1}^{k} \hat{\mathbf{J}}_k \mathbf{J} = \hat{\mathbf{J}}\mathbf{J}. \tag{4.1.10}$$

How to calculate the phase retardation on the base of a Jones matrix? First we have to carry out the ray tracing and to obtain the Jones matrices for each ray crossing each element. Then we can build the Jones matrices $\hat{\mathbf{J}}$ for each ray i.e. for each point in the pupil plane. The retardation value $RET(\hat{\mathbf{J}})$ for this pupil point can be obtained by the polar decomposition of the Jones matrix $\hat{\mathbf{J}}$.

It is known from linear algebra [28] that for any complex square matrix $\mathbf{M}$ there is exist nonnegative definite Hermitian matrices $\mathbf{H}$ and $\mathbf{H}'$ and a unitary matrix $\mathbf{U}$, such that

$$\mathbf{M} = \mathbf{U}\mathbf{H} = \mathbf{H}'\mathbf{U}. \tag{4.1.11}$$

This is known as the polar decomposition of $\mathbf{M}$. Matrices $\mathbf{U}$, $\mathbf{H}$ and $\mathbf{H}'$ can be uniquely determined by

$$\mathbf{U} = \mathbf{M}\mathbf{H}^{-1} = \mathbf{H}'^{-1}\mathbf{M}, \quad \mathbf{H}^2 = \mathbf{M}^*\mathbf{M}, \quad \mathbf{H}'^2 = \mathbf{M}\mathbf{M}^*, \tag{4.1.12}$$

where * denotes the conjugate transpose (Hermitian conjugate). However, $\mathbf{U}$ is not uniquely determined for a singular matrix $\mathbf{M}$.

Applying the polar decomposition to a Jones matrix we have

$$\hat{\mathbf{J}} = \hat{\mathbf{J}}_R \hat{\mathbf{J}}_D = \hat{\mathbf{J}}_D' \hat{\mathbf{J}}_R, \tag{4.1.13}$$

where $\hat{\mathbf{J}}_R$ is a retarder (unitary) Jones matrix and $\hat{\mathbf{J}}_D$ and $\hat{\mathbf{J}}_D'$ are diattenuator (nonnegative definite Hermitian) Jones matrix. The diattenuation defines the dependence of the polarization element's transmittance on the incident polarization state. The retardance shows the dependence of the polarization elements optical path length on the incident polarization state. Therefore any polarization element described by a Jones matrix can be interpreted as a couple of a retarder and a diattenuator.

Matrices $\hat{\mathbf{J}}_D$ and $\hat{\mathbf{J}}_D'$ can be diagonalized by unitary matrices, applying the singular value decomposition

$$\hat{\mathbf{J}} = \mathbf{V}\mathbf{D}\mathbf{W}^*, \tag{4.1.14}$$

where $\mathbf{D}$ is a diagonal matrix having the singular values of $\hat{\mathbf{J}}$ as diagonal elements, $\mathbf{V}$ and $\mathbf{W}^*$ are unitary matrices. Thus we can obtain

$$\hat{\mathbf{J}}_{\mathbf{D}} = \mathbf{WDW}^*, \quad \hat{\mathbf{J}}_{\mathbf{D}}' = \mathbf{VDV}^*, \quad \hat{\mathbf{J}}_{\mathbf{R}} = \mathbf{VW}^*. \qquad (4.1.15)$$

From the polar decomposition described above we can define the retardation of an arbitrary polarization element $\hat{\mathbf{J}}$.

It can be shown [29] that with our definitions the retardation can be found even without polar decomposition as

$$RET\,(\hat{\mathbf{J}}) = 2\cos^{-1}\frac{\left|\operatorname{tr}\hat{\mathbf{J}} + \dfrac{\det\hat{\mathbf{J}}}{\left|\det\hat{\mathbf{J}}\right|}\operatorname{tr}\hat{\mathbf{J}}^*\right|}{2\left[\operatorname{tr}(\hat{\mathbf{J}}^*\hat{\mathbf{J}}) + 2\left|\det\hat{\mathbf{J}}\right|\right]^{\frac{1}{2}}}. \qquad (4.1.16)$$

If the Jones matrix is written as

$$\hat{\mathbf{J}} = \begin{pmatrix} j_{11} & j_{12} \\ j_{21} & j_{22} \end{pmatrix} = \begin{pmatrix} j_{r11} + i\cdot j_{i11} & j_{r12} + i\cdot j_{i12} \\ j_{r21} + i\cdot j_{i21} & j_{r22} + i\cdot j_{i22} \end{pmatrix} \text{ or} \qquad (4.1.17)$$

$$\hat{\mathbf{J}} = \hat{\mathbf{J}}_{\mathbf{r}} + \hat{\mathbf{J}}_{\mathbf{i}} = \begin{pmatrix} j_{r11} + i\cdot j_{i11} & j_{r12} + i\cdot j_{i12} \\ j_{r21} + i\cdot j_{i21} & j_{r22} + i\cdot j_{i22} \end{pmatrix}, \qquad (4.1.18)$$

with j_r and j_i the real and imaginary elements, we can determine the $\hat{\mathbf{J}}_{\mathbf{R}}$ and $\hat{\mathbf{J}}_{\mathbf{D}}$ matrices by using Eq. (4.1.16)

The Jones matrix for each ray traversing each component can be described by ray coordinates on the specific surface X and Y (or pupil coordinates ρ_x and ρ_y), and by the direction cosines $L,\ M$ and N for each intersection ray-surface. For the specified field point in the image plane $L,\ M$ and N also can be defined by the pupil coordinates ρ_x and ρ_y. For an optical system with k components we are now allowed to write

$$\prod_1^k \hat{\mathbf{J}}_k(X_k, Y_k) = \begin{bmatrix} j_{11}(\rho_x,\rho_y) & j_{12}(\rho_x,\rho_y) \\ j_{21}(\rho_x,\rho_y) & j_{22}(\rho_x,\rho_y) \end{bmatrix}. \qquad (4.1.19)$$

If the incident ray on the first surface is linearly polarized in the azimutal direction θ as measured from the x-axis, then the Jones vector $\mathbf{J}$ is given by $(\cos\theta, \sin\theta)$ independently of the beam path. Then the following equation gives the complex amplitude transmittance of the optical system at the exit pupil decomposed into its orthogonal-polarization components

$$\mathbf{J}' = \begin{bmatrix} D_x'(\rho_x,\rho_y) \\ D_y'(\rho_x,\rho_y) \end{bmatrix} = \begin{bmatrix} j_{11}(\rho_x,\rho_y)\cos\theta + j_{12}(\rho_x,\rho_y)\sin\theta \\ j_{21}(\rho_x,\rho_y)\cos\theta + j_{22}(\rho_x,\rho_y)\sin\theta \end{bmatrix}. \qquad (4.1.20)$$

Since $\mathbf{J}'$ is a function of the pupil coordinates, it is possible to calculate the image quality taking into account the polarization effects only as a function of the position (ρ_x, ρ_y) in the exit pupil [30].

4.2.   BISD in optical design

The presence of the BISD effect in crystals at short wavelengths was a surprise for the lithography industry that has caused considerable difficulties for 157 nm lithography. Lithography equipment manufacturers were already familiar with stress-induced birefringence in calcium fluoride (induced by technological machining) and they were prepared to compensate it with relatively complex lens designs. But intrinsic

birefringence is able to inflict several times more birefringence than allowed, creating fuzzy images at the wafer.

In optical system design, BISD leads to the appearance of multiple polarized rays during refraction. There are two basic effects depending on crystal orientation, wavelength, thickness and shape of the lens. The first BISD consequence is the appearance of an optical path-length difference between the two orthogonally polarized components corresponding to a ray. This path-length difference, resulting in a phase retardation, can be visualized in pupil maps for arbitrary field points. An example of such a pupil map is shown in Figure 4.2.1.

<RET>=85.17 σ=53.26
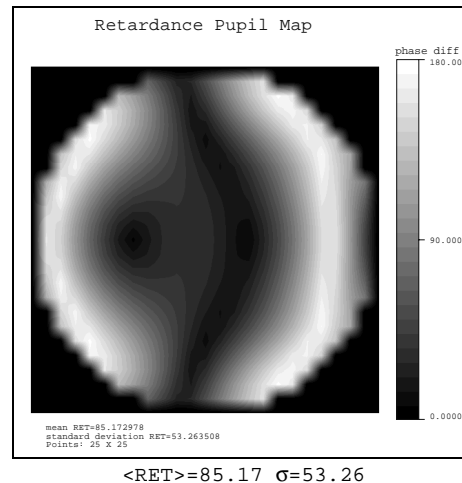
Figure 4.2.1 Retardation pupil map produced with Code V. The dark tone indicates regions with low phase retardation and light tone indicates ones with high phase retardation. <RET> is the average retardation value and σ is the standard deviation over the pupil.

The second consequence of BISD is a small angular difference in ray paths. In an optical system with N components, for each incident ray on the first surface there are 2^N outgoing rays at the image plane. For instance, in an optical system containing two birefringent elements there are four branches in the network. One set of rays is in the ordinary polarization mode in both the first and the second birefringent elements (fully ordinary ray). A second set is ordinary in the first and extraordinary in the second. The third set is extraordinary in the first and ordinary in the second, and the fourth set is extraordinary in both elements. Such multiple ray sets produce transmitted wave fronts, which may or may not substantially overlap in the exit pupil and in the image plane (see Figure 4.2.2).
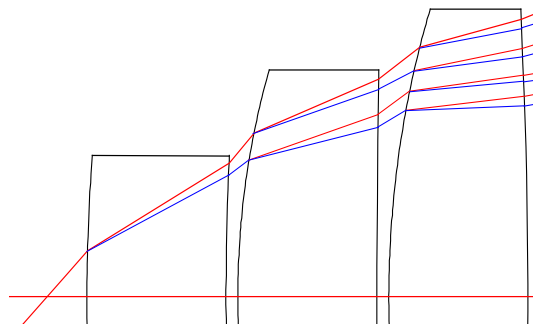
Figure 4.2.2 Ray splitting in optical system. On each surface each ray may split into two. (The birefringence effect is exaggerated for demonstration purposes)

The bifurcation of the rays leads to an angular difference in ray path between ordinary and extraordinary rays after each refraction, which results in a ray deviation at the

image plane. Thus, instead of one ray there is a full cone of outgoing rays and the opening angle of this cone can be called the maximal angular deviation.
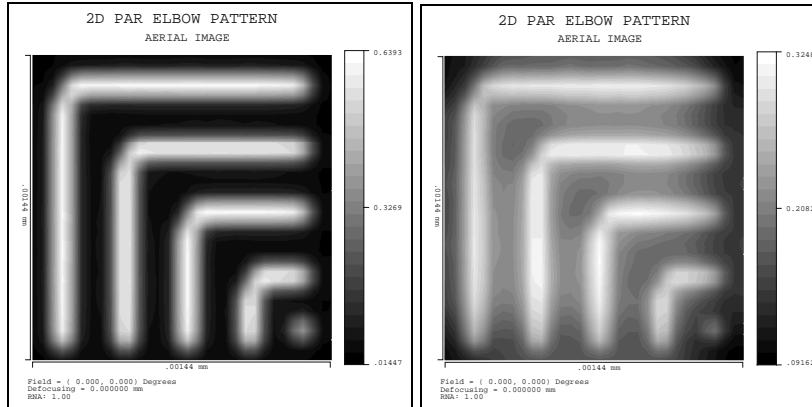
Figure 4.2.3 Image contrast loss due the BISD-caused phase retardation. In the graph on the left side the BISD is not considered; in the right-hand drawing the BISD is included. Image size of the shown area is about 1×1μm.

The polarization phase shifting and the ray bifurcation induce undesirable effects for the image formation. The degradation of the image quality caused by phase retardation is shown in Figure 4.2.3.

The first issue in optical system design considering BISD is the calculation of the effect itself. Only one commercial optical design program (Code V®, © Optical Research Associates) supports the calculation of the effect within a given approximation and analysis of the image quality, taking into account the phase retardation caused by BISD. For each lens the maximum of linear birefringence value $\Delta n = n_o - n_e$ (i.e. in <011> direction) and the crystal orientation can be specified. For CaF$_2$ and BaF$_2$, the Δn value was measured by John Burnett et al [17] and it amounts at 157 nm to $\Delta n = -11.8 \times 10^{-7}$ for CaF$_2$ and $\Delta n = 34 \times 10^{-7}$ for BaF$_2$.

In general any crystal orientation can be described by three Euler angles. To this purpose we use two polar coordinates φ and θ shown in Figure 3.3.1 for the definition of the optical axis direction and a pupil angle ψ for crystal orientation around this optical axis. In order to define some intermediate positions it is convenient to introduce the notation where in addition to crystal orientations we define the orientation of the pupil map (angle ψ counted in a clockwise direction) as <crystal orientation>-ψ e.g. <001>-0°, <100>-45°, <111>-0°, <111>-60° etc (see Figure 4.2.4). The value of these angles for some characteristic crystal orientation can be observed in Table 4.2.1. However for computation of cubic crystal intrinsic birefringence Code V requires six angles for the Y and Z cubic crystal axis to specify the crystal orientation [31]. Obviously three of these angles are superfluous because their values can be defined through φ, θ and ψ as follows:

$$
\left.
\begin{aligned}
\alpha_Y &= \sin(\varphi)\cos(\psi) + \cos(\varphi)\cos(\theta)\sin(\psi), \\
\beta_Y &= \cos(\varphi)\cos(\theta)\cos(\psi) - \sin(\varphi)\sin(\psi), \\
\gamma_Y &= -\cos(\varphi)\sin(\theta), \\
\alpha_Z &= \sin(\theta)\sin(\psi), \\
\beta_Z &= \sin(\theta)\cos(\psi), \\
\gamma_Z &= \cos(\theta).
\end{aligned}
\right\}
\qquad (4.2.1)
$$

| <001>-0° | <001>-45° | <111>-0° | <111>-60° |
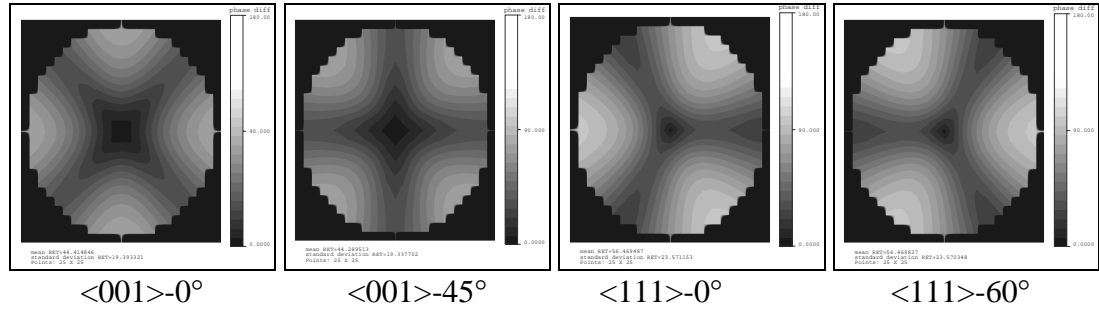
Figure 4.2.4 Designation of the orientation of pupil maps.

Moreover Code V has limitations in computing, e.g. the arbitrary choice of the crystal orientation during optimization is not supported; the ray bifurcation and its consequences on energy transmission are not included (only specified one ray from cone generated by multiple bifurcations can be computed at the same time i.e. a ray with defined ordinary-extraordinary ray selection, thus reducing the result to one combination from 2^N outgoing rays).

Table 4.2.1 Direction angles for characteristic crystal orientations.

Crystal orientation	φ	θ	ψ
<001>-0°	0	0	0
<001>-45°	0	0	$\pi/4$
<011>-0°	0	$\pi/4$	0
<111>-0°	$\pi/4$	$\arctan\sqrt{2}$	0
<111>-60°	$\pi/4$	$\arctan\sqrt{2}$	$\pi/3$

In the case of the BISD the phase retardation is a function of the angle between the ray and the optical axis of the crystal. Depending on the crystallographic direction chosen as an optical axis, different types of distribution of the phase retardation over the pupil can be observed. The directions with circular symmetry are shown in Table 4.2.2. Here we show the retardation dependence for one optical element, i.e. one of single lens in Figure 4.2.2.

It can be observed from this table that, the <001> direction has a minimum for the axial point if this direction is chosen along an optical axis, and four maxima around forming a square-like distribution, i.e. it has 4-fold (90°) symmetry. For the <111> direction we have a similar distribution with zero retardation at the center of the pupil and three maxima at the edge, i.e. the <111> direction exhibits a 3-fold (120°) symmetry. Finally, for the <011> direction we have almost circularly symmetrical distribution around the maximum at the center of the pupil. However, there is a very important nuance; because the <111> direction is not symmetric with respect to the center of pupil, we have to be careful of the change of sign of the angle between the incident ray and the optical axis when we use a <111> crystal orientation because in this case the orientation <111> - 0° becomes <111> - 60°, and vice versa i.e. the same component may have turned pupil maps for different beams.

Table 4.2.2 Directional dependence of the BISD for single lens.

Chosen optical axis	The phase retardation dependence over the pupil	The projections of eigenvector states on the pupil
<100>		
<110>		
<111>		
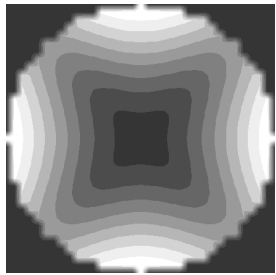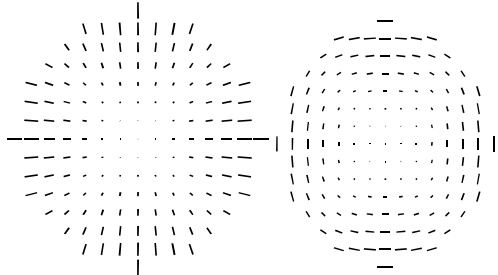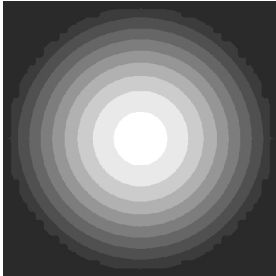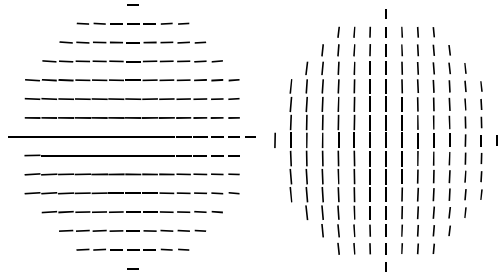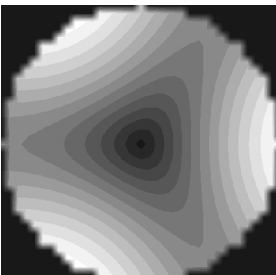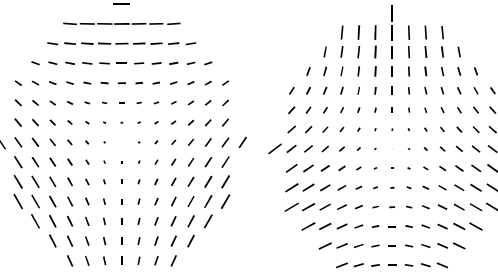
Table 4.2.3 Accuracy of BISD calculation with various numbers of rays.

	Number of rays	5	13	24	49	89	481	973
	Computation time, sec	0.5	0.9	1.5	2	4	16	34
Low BISD Value	Mean retardation	154.32	149.68	151.17	148.95	151.54	151.04	151.11
	Standard deviation of retardation	11.174	10.717	12.075	12.235	13.546	14.136	14.103
High BISD value	Mean retardation	28.176	86.253	76.489	88.437	82.043	85.119	84.729
	Standard deviation of retardation	35.734	59.455	41.456	49.023	51.595	49.944	49.791

The second important design issue is the speed of computation. For an adequate estimation of BISD it is necessary to trace through the system at least 50 rays taking into account their polarization properties (see Table 4.2.3). According to our experience the accuracy of the computation of retardation should nor exceed ±5°. For a lithographic lens with about 50 surfaces this requirement drastically increases the time of image quality estimation. The computation of all possible ordinary-extraordinary ray combinations of splittings only for one ray takes a week on the modern PC with Pentium IV processor.

4.3.   Image quality in the presence of BISD

Another issue is to identify a relevant characteristic of the image quality for BISD in DUV systems. In optical design it would be very convenient to define the influence of BISD on the image quality by one number. We found that the standard deviation of the retardation over the pupil is a good indicator of the BISD influence. This quantity shows a very good correlation with the image quality loss due to the phase retardation. This is confirmed by the calculation of BISD in optical systems with and without BISD compensation (see Table 4.3.2). It is obvious that not only the value of Strehl ratio but also the standard deviation of the retardation indicates adequately the loss of image quality caused by BISD. Therefore, by taking the standard deviation of the retardation into the merit function we can optimize an optical system with respect to the BISD correction.

Table 4.3.1 Image quality in an optical system with and without BISD compensation.

Field #	Strehl ratio (in the absence of **BISD**)	**BISD** uncompensated			**BISD** compensation		
		Strehl ratio	mean retardation	standard deviation of retardation	Strehl ratio	mean retardation	standard deviation of retardation
1	**0.841016**	**0.2348**	93.8879	**51.0658**	**0.7889**	18.8005	**7.56805**
2	0.838666	0.2444	93.7125	**51.0096**	0.7950	23.2214	**10.8823**
3	0.835668	0.2440	93.7175	**50.0968**	0.7670	34.5270	**14.3829**
4	0.836719	0.2465	94.0004	**48.2277**	0.7177	45.5730	**17.0637**
5	0.830060	0.2852	90.2522	**45.2942**	0.6973	55.7135	**16.4321**

The reader might be surprised to see the relatively low values of the Strehl ratio in the first column, for our very well corrected optical systems such as lithographic objectives. For the explanation of this fact we will obtain the expression for Strehl ratio in the case of polarized beams.

The Strehl ratio for an ideal aberration-free optical system with high NA can be defined by two expressions

$$S_1 = \frac{\left| \dfrac{1}{\pi} \int\limits_0^1 \int\limits_0^{2\pi} A(\rho,\varphi)\rho \, d\rho \, d\varphi \right|^2}{\dfrac{1}{\pi} \int\limits_0^1 \int\limits_0^{2\pi} \left| A(\rho,\varphi) \right|^2 \rho \, d\rho \, d\varphi} \tag{4.3.1}$$

or

$$S_2 = \frac{\left| \dfrac{1}{\pi} \int\limits_0^1 \int\limits_0^{2\pi} A(\rho,\varphi)\rho \, d\rho \, d\varphi \right|^2}{1}, \tag{4.3.2}$$

where ρ is the lateral position on the exit pupil sphere relative to the pupil rim, φ is the azimuth in the pupil and $A(\rho,\varphi)$ is the pupil function defined as

$$A(\rho,\varphi) = B(\rho,\varphi)\exp\{ikW(\rho,\varphi)\} . \tag{4.3.3}$$

In the last expression $B(\rho,\varphi)$ is the amplitude distribution and $W(\rho,\varphi)$ is the wavefront aberration. The first definition according to S_1 is the general one, the second definition (4.3.2) is used when $A(\rho,\varphi)$ has the property that $B(\rho,\varphi) \equiv 1$. In the case of an aberration-free high-NA optical system, the "effective" amplitude part

of the pupil function $A(\rho,\varphi)$ is not uniform but shows a more complicated behavior [32] in ρ according to the expression

$$B(\rho) = \frac{1+\sqrt{1-NA^2\rho^2}}{2} \frac{1}{\left(1-NA^2\rho^2\right)^{1/4}} . \qquad (4.3.4)$$

In the function $B(\rho)$, both the polarization effects in a high-NA systems have been incorporated and the amplitude distribution adaptation at high-NA that is found in a system that obeys the sine condition. A more detailed analysis of the Strehl ratio definition when the image space itself is anisotropic can be found in [33]

The first factor of $B(\rho)$ takes into account the polarization effect and after averaging over an annular area the amplitude distribution is

$$B_1(\rho) = \frac{1+\sqrt{1-NA^2\rho^2}}{2} . \qquad (4.3.5)$$

The second factor of $B(\rho)$ is specific for the amplitude distribution on the exit pupil sphere of the optical system in terms of the lateral coordinate ρ on that sphere

$$B_2(\rho) = \frac{1}{\left(1-NA^2\rho^2\right)^{1/4}} . \qquad (4.3.6)$$

Carrying out the integrations with the substitution $\sin\theta = NA/n$ according to the definition in Chapter 2.4, where n is the refractive index in the image space, we obtain

$$S_1 = \frac{8}{\sin^2\theta} \left(\frac{\frac{1}{9}\left(1-\cos^{3/2}\theta\right)^2 + \frac{1}{25}\left(1-\cos^{5/2}\theta\right)^2 + \frac{2}{15}\left(1-\cos^{3/2}\theta\right)\left(1-\cos^{5/2}\theta\right)}{\left(1-\cos\theta\right)+\frac{1}{3}\left(1-\cos^3\theta\right)+\sin^2\theta} \right), \qquad (4.3.7)$$

and

$$S_2 = \frac{1}{4\sin^2\theta}\left(2\left(1-\cos\theta\right)+\frac{2}{3}\left(1-\cos^3\theta\right)+2\sin^2\theta\right). \qquad (4.3.8)$$

Definition (4.3.1) leads to a much smaller high-NA effect and is physically more consistent; a defect-free optical system produced a Strehl ratio close to unity. For instance, Code V computes the Strehl ratio in two analysis modes: Wavefront Analysis (WAV) and Point Spread Function (PSF). In the WAV-mode Code V uses the following relationship

$$S = e^{-(2\pi\sigma)^2} , \qquad (4.3.9)$$

where σ is the root-mean-square (RMS) wavefront error. This relationship is quite accurate for RMS < 0.1 waves. In the PSF-mode the actual PSF data are available to calculate the Strehl ratio numerically. The PSF is computed as a sum of contributions from each point in the pupil, a separate summation is made in which the contributions from each point in the pupil have no phase aberration - i.e. the second summation is made while setting the aberration to zero. This second sum represents the value that is used to compute the perfect lens peak value. Because of the way in which this term is computed, the perfect lens value does account for vignetting (it uses the real pupil shape). It also inherently computes the peak at the best focus for the ideal lens. The peak for the actual lens is computed by evaluating the PSF at each point in the image plane (i.e. the plane tangent to the image surface at the point where the principal ray intersects the image surface.). The WAV- and PSF-based Strehl values may differ

somewhat due to their different principle, different grid size and other factors but the PSF calculation is generally more accurate [34].

The values of the Strehl ratio for different θ in the case of an ideal system are shown in Table 4.3.2.

Table 4.3.2 Strehl ratio values for an ideal optical system illuminated by a linearly polarized incident beam.

θ, degrees	NA in air	S1	S2	Code V
0	0	1.00000	1.00000	1
5	0.087156	1.00000	1.00000	0.998109
10	0.173648	1.00000	1.00002	0.992541
15	0.258819	1.00000	1.00010	0.983593
20	0.342020	1.00000	1.00031	0.971731
25	0.422618	1.00000	1.00077	0.957429
30	0.500000	0.99999	1.00160	0.935929
35	0.573576	0.99999	1.00300	0.924210
40	0.642788	0.99999	1.00517	0.906846
45	0.707107	0.99998	1.00838	0.889721
50	0.766044	0.99996	1.01295	0.872998
55	0.819152	0.99989	1.01926	0.857365
60	0.866025	0.99976	1.02778	0.842727
65	0.906308	0.99948	1.03906	0.830679
70	0.939693	0.99891	1.05377	0.820619
75	0.965926	0.99774	1.07273	0.812145
80	0.984808	0.99531	1.09697	0.806401
85	0.996195	0.99002	1.12775	0.801787
90	1.000000	0.97524	1.16667	0.800620

Table 4.3.3 Dependence of the Strehl ratio on aperture value when polarization effects are taken into account.

Field #	Strehl ratio						
	No polarization ray tracing, Image NA 0.75	Polarization ray tracing enabled, No coating, No BISD phase retardation, Image NA 0.75	Polarization ray tracing enabled, Ideal coating, No BISD phase retardation, Image NA 0.75	Polarization ray tracing enabled, Ideal coating, No BISD phase retardation, Image NA 0.56	Polarization ray tracing enabled, Ideal coating, No BISD phase retardation, Image NA 0.28	Polarization ray tracing enabled, Ideal coating, BISD phase retardation uncompensated, Image NA 0.75	Polarization ray tracing enabled, Ideal coating, BISD phase retardation compensated Image NA 0.75
1	0.9968	0.799467	0.841016	0.914413	0.975125	0.2348	0.7889
2	0.9938	0.768287	0.838666	0.914879	0.976685	0.2444	0.7950
3	0.9912	0.773003	0.835668	0.912160	0.976423	0.2440	0.7670
4	0.9937	0.788147	0.836719	0.912932	0.977304	0.2465	0.7177
5	0.9791	0.762186	0.830060	0.902666	0.972940	0.2852	0.6973

The dependence of Strehl ratio on NA is remarkable. It is seen that in the case of high NA the value of Strehl ratio cannot exceed some certain NA-defined limit even in case of an ideal optical system once the polarization of the light is taken into account. Table 4.3.3 shows the value of Strehl ratio for different cases depending on incorporation of the BISD-effect, coating issues and the value of NA.

4.4.   Analysis of the phase retardation

It was shown that the phase retardation caused by BISD leads to a loss of image contrast. As it follows from Eq. (4.1.5) the magnitude of the phase retardation value of a single component depends on the thickness and the linear birefringence of the medium. In turn linear birefringence depends on the angle between the direction of the ray and on the crystal optical axis, i.e. on the incident angle, shape of the lens and on the position of the component in optical system.

It is not only the magnitude of the phase retardation which is important for an analysis of the total phase retardation but its orientation as well. After refraction into a lens, this orientation can be defined as the orientation of the projection of the fast eigenvector onto the pupil plane.   Figure 4.4.1 illustrates the value of the phase retardation.   The magnitude of retardation in degrees is shown in Figure 4.4.1 a), it changes within the range of 0…180°. The orientation of the retardation is shown in Figure 4.4.1 b) where vertical lines have retardation orientation of 0° and coincide with a vertical fast axis. The value of the orientation of the phase retardation is within the range of -90…90°. Multiplying the values in a) and b) yields the line graph retardation representation shown in Figure 4.4.1 c).

<RET>=100.10 σ=43.62

a)   b)   c)
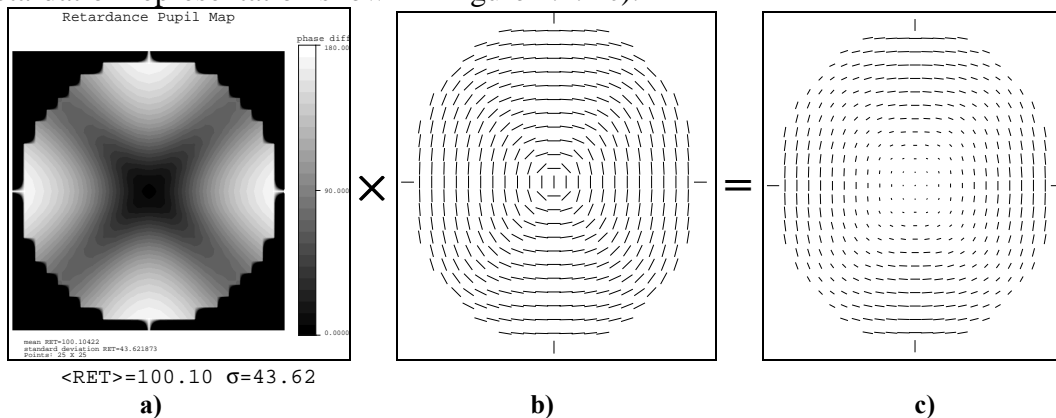
Figure 4.4.1 Visualization of the retardation value: a) pupil map of retardation magnitude; b) pupil map of retardation orientation; c) line graph of the lens retardation where the length of each line represents the retardation magnitude and orientation indicates the fast-axis orientation.

We will show that it is very useful for our investigation to determine the contribution of separate components in the cumulative phase retardation of an objective for lithography. For this purpose, we classify optical components according to their contribution to the cumulative phase retardation. The phase retardation for each component was computed and normalized to the maximum value for each case. In order to define the maximal possible contribution, the computations were made with a marginal ray for the crystal orientations <001> and <111>. Because the phase retardation distribution is monotonic, only one ray needs to be traced for these directions. For the <011> direction, however, the difference between center and edge of the pupil must be computed, because both have non-zero retardation value. In this case at least two rays, the marginal one and the ray along the optical axis, have to be traced. It should be pointed out that for the <011> direction the distribution be inverted when the retardation at the edge is higher than the retardation in the center of

the pupil. This happens, for instance, in biconcave lenses, when the edge thickness is much larger than the center thickness.

An optical system with components gray-scaled according to their phase retardation contribution is shown in Figure 4.4.2. (The specifications of this system were taken from Ref. [35].) It can be seen that for the <001> and <111> orientations only a few components contribute significantly to the cumulative retardation. For the <011> direction, several components have a significant contribution because in this case the phase retardation contribution mostly depends on the lens thickness.

Figure 4.4.3 shows the distribution of the cumulative phase retardation over the pupil depending on the crystal orientation for the optical system shown in Figure 4.4.2 In this case all components in the optical system are oriented along the same direction.
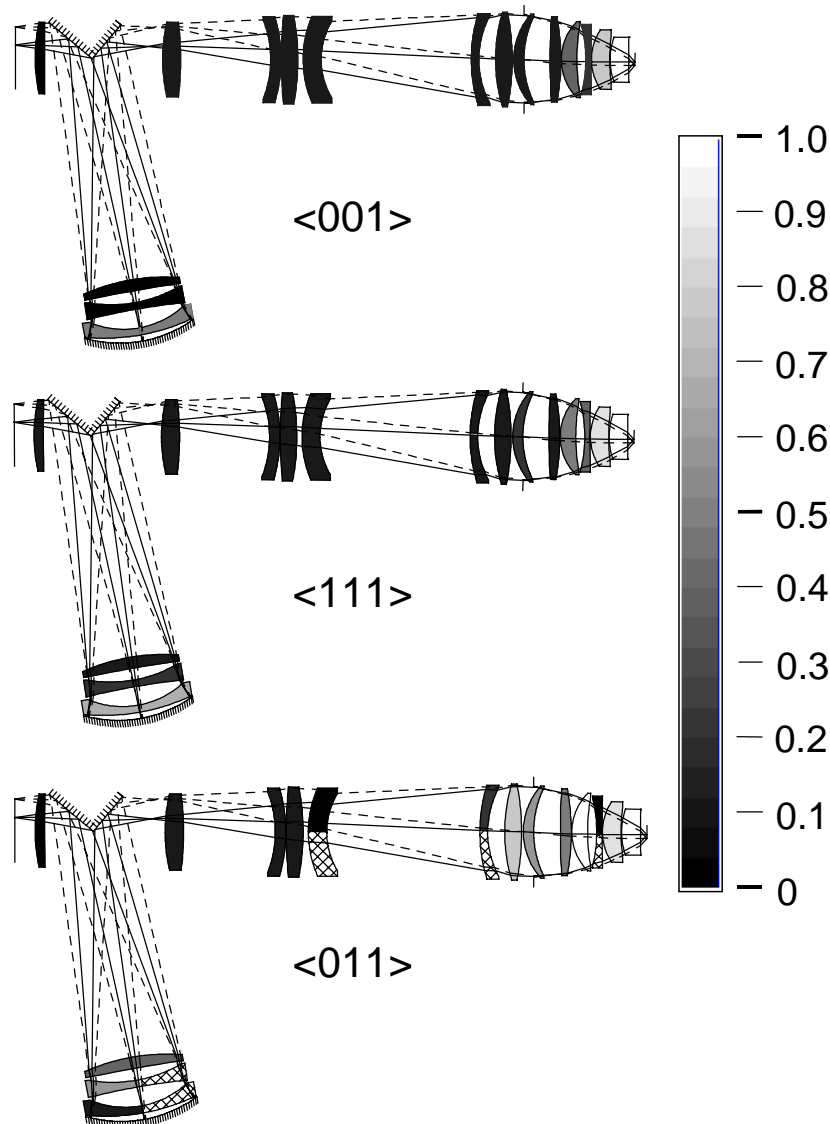
Figure 4.4.2 Contribution of separate components to the cumulative phase retardation depending on the chosen crystal orientation (all components have the same orientation shown below). A light tone indicates components with high contribution. For the <011> direction, the elements with inverted retardation value distribution (with highest retardation value at the edge) are partially hatched.

<RET>=93.67 σ=51.07

a)

<RET>=73.11 σ=44.51

b)

<RET>=108.51 σ=52.20

c)
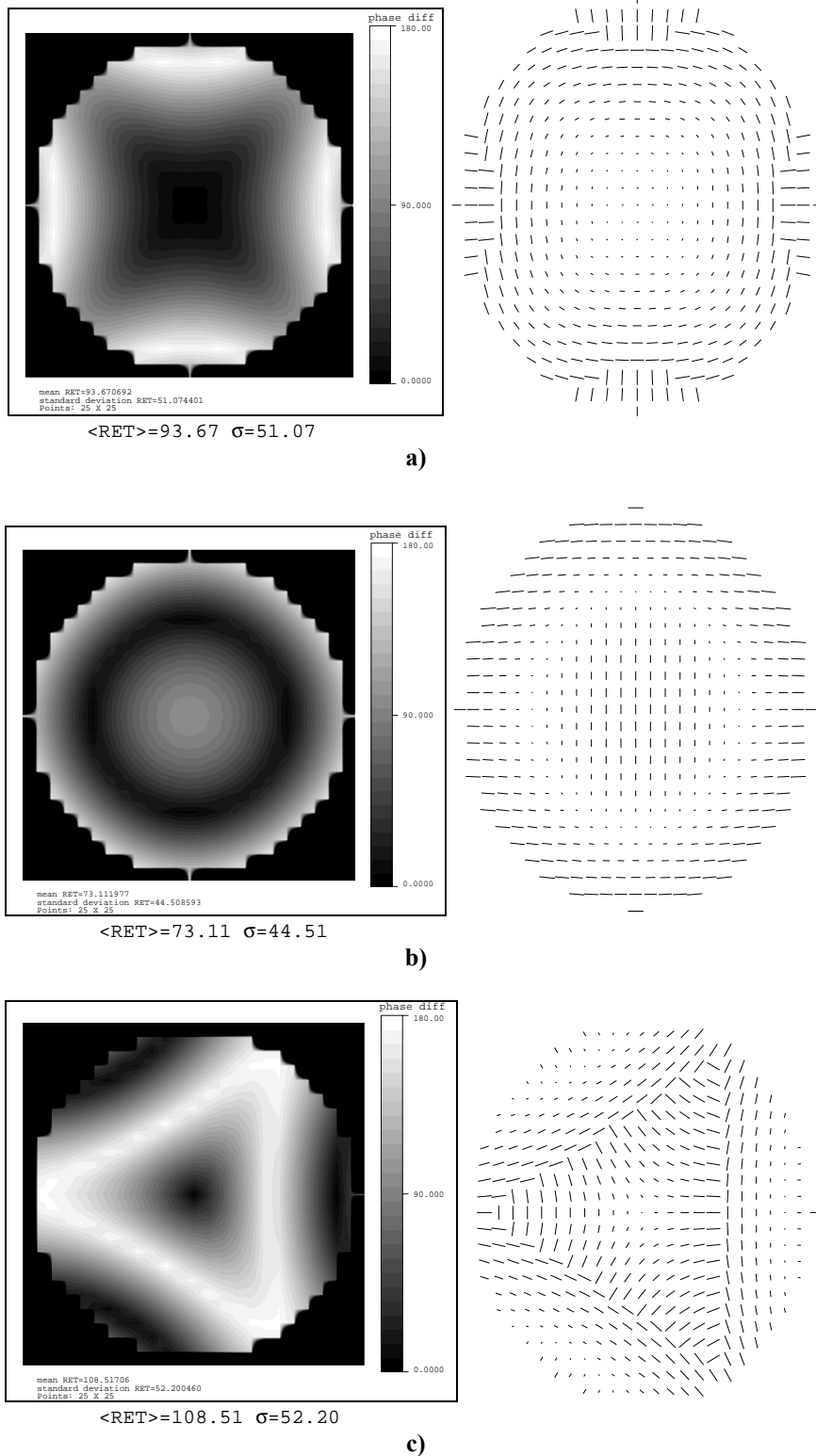
Figure 4.4.3 Cumulative phase retardation pupil maps depending on different crystal orientation for the optical system shown in Figure 4.4.2. The graphs on the right side represent the orientation and the retardation magnitude like in Figure 4.4.1: a) all components are oriented along <100> direction; b) all components are oriented along <110> direction; c) all components are oriented along <111> direction.

4.5.   Analysis of ray bifurcation

Although a certain number of the researches claim that the magnitude of the ray deviation caused by BISD is very small and that a single path approximation for the ray tracing is sufficient, we will pay some attention to this effect. In particular, in reference [36] it was shown that the phase error introduced by the ray bifurcation cannot exceed several nanometers even in the case of a long track in material. However, in order to illustrate the birefringence properties we want to discuss the easiest way to compute possible ray deviation. This research may also be helpful to analyze the ray propagation in other media with weak birefringence.

When a single ray propagates through a birefringent optical element, two distinct rays are transmitted. Thus, as it was mentioned above, in an optical system containing N birefringent elements, each ray incident upon the entrance pupil can result in as many as 2^N rays at the exit pupil. If we consider a single ray propagating from object to image, we can observe multiple ray bifurcation at the image plane similar to a scattering mechanism. For the estimation of the bifurcation effect, a ray deviation similar to the geometrical transverse aberration can be computed. This ray deviation can be defined as the maximum distance in the image plane between two rays having the same origin before the first bifurcation. For preserving good image quality this deviation should not exceed the resolution limit. A more appropriate method would be to analyze the corresponding 2^N wavefronts that exit from the pupil of the system, but computational load is prohibitive. We will show some examples of "bifurcated" wavefronts further on in this section.

It is not a trivial task to select from 2^N possible ray combinations the ray with maximum deviation in the image plane. We offer the following algorithm for this purpose:

1. For each birefringent component we define a binary code "0" or "1" depending on which ray is computed: the ordinary or the extraordinary one. The number of digits in the code shows the number of birefringent components in the optical system. Thus each ray from 2^N has its own binary code. For instance a code "100000100110001" indicates that there are 15 birefringent components and from all possible combinations we select the extraordinary ray after the refraction on components 1, 7, 10, 11, and 15, and the ordinary ray after refraction on the remaining components. This binary code can be easily converted to decimal numeration and then the ray with code 0 is "fully ordinary" and the ray with code 2^N-1 is "fully extraordinary".

2. The contribution of each single component to the total ray deviation is computed, i.e. a ray with only a single "1" in its code. The fully ordinary ray is taken as a reference. As in the case of the phase retardation, it is useful, for further analysis, to classify components in the optical system according to their contribution to the cumulative ray deviation value. The same optical system as before with its components colored according to the magnitude of their contribution is shown in Figure 4.5.1. From a comparison with Figure 4.4.2 it turns out that the contribution of separate components in the cumulative ray deviation effect does not substantially differ from the phase retardation contributions. The difference can be explained by the observation that the optical power of a lens plays a role for the ray deviation and it has no influence on the phase retardation.

3. The maximum ray deviation is computed. Because the contribution of the effect for a single component is very small, it is possible to obtain the total ray deviation in the image plane by adding corresponding contributions from each component. This observation is confirmed by direct computation of all possible combinations

of rays for a marginal ray in the lithographic system. In all cases, observed by us, the deviation value obtained by adding component contributions and the one obtained by ray tracing are the same.
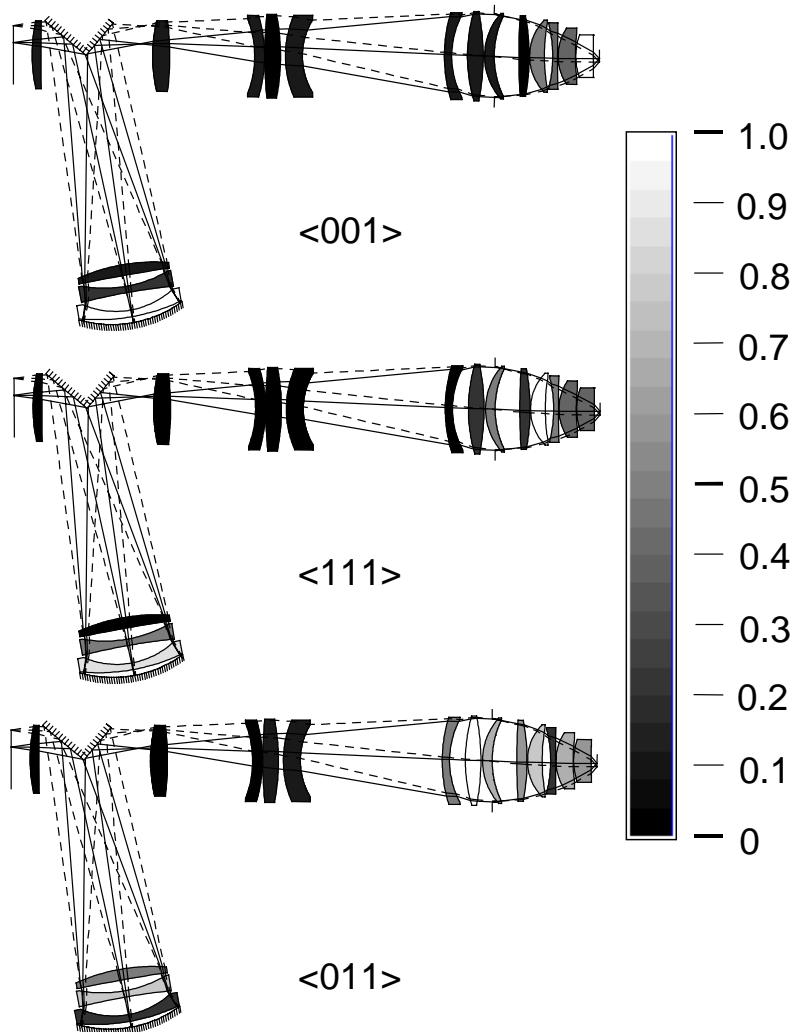
Figure 4.5.1 Contribution of separate components to the cumulative ray deviation depending on the chosen crystal direction. A light tone indicates components with high contribution.

Interestingly, the maximal absolute deviation is found not for the fully extraordinary ray (ray with all "1" in the code) but for one of the rays collecting all partial deviations with the same sign. Thus the maximum ray deviation is the difference between positions of two rays collecting all partial deviations of the same sign. The second consequence is that instead of computing 2^N rays for obtaining the maximal deviation value it is enough to compute just N+1 rays. This observation is valid not only for BISD ray bifurcation but for any ray bifurcation consisting of reasonably small contributions e.g. stress-induced birefringence.

Unfortunately mutual compensation of ray deviation is not possible in general, because there are always two rays that absorb all positive or negative contributions. It is only possible to redistribute all contributions in such a way that the difference for fully ordinary and extraordinary rays is null. In this case the modulus of two sums for all partial deviations of the same sign should be equal. Thus there is only one approach for minimization of the ray deviation - to minimize the final value of deviation by minimization of partial contributions.

It is important to know how the ray deviation is distributed between maximum and minimum values. In order to investigate this problem, 5000 random samples of rays for the same system presented in Figure 4.5.1 and partial contributions of components were taken and a statistical analysis was done. As it is seen from Figure 4.5.2 the ray deviation is almost normally distributed between the maximum and minimum deviation value and the mean value is about the average between them. If we suppose that the ray deviation corresponds to a normal distribution, 70% percent of the rays are within a confidence interval defined by the value of the standard deviation σ. Thus, on the basis of computed limits of deviation it is possible to estimate the energy distribution in the luminous spot in the image plane (all within the framework of geometrical optics). The relative importance of ordinary and extraordinary rays in each lens medium has not been included.
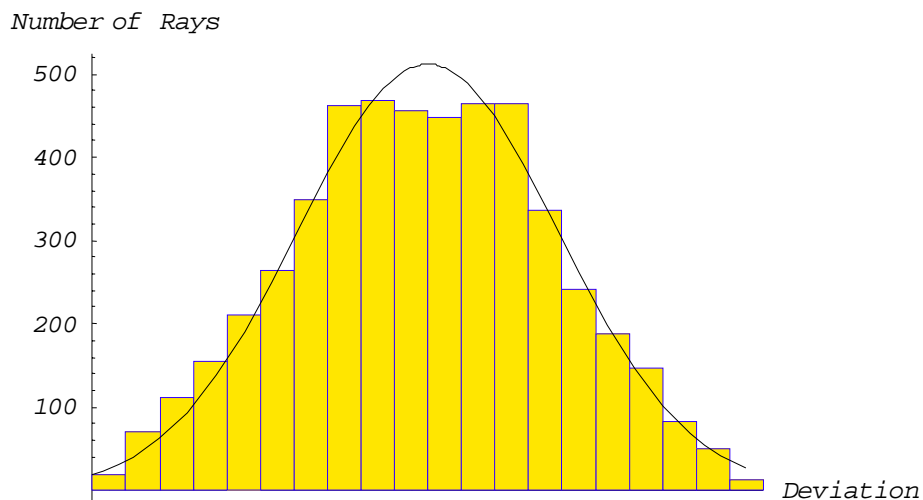
Figure 4.5.2 The distribution of the ray deviation obtained on the base of 5000 random ray samples for the optical system shown in Figure 4.5.1. A best-fitting normal distribution has been shown for comparison.
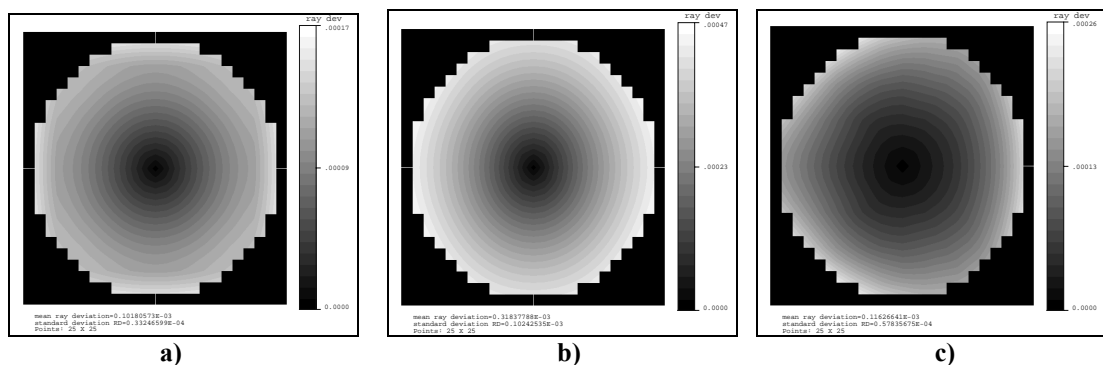
Figure 4.5.3 Ray deviation pupil map depending on different crystal orientations in the optical system shown in Figure 4.5.1. The map has been calculated for an on-axis object point using 441 rays (square grid 25×25): a) for <100> direction; b) for <011> direction; c) for <111> direction.

As it follows from Figure 4.5.3, the distribution of the ray deviation over the pupil depending on crystal orientation differs from the corresponding phase retardation distribution. Usually the ray deviation has almost circular distribution and may just slightly resemble the corresponding retardation pupil maps. The minimum mean deviation is observed for <100> direction.

The total value of the ray deviation for the entire system depends mainly on the amount of cubic crystals in the optical system and it changes for different basic types

of optical systems. The average value of the ray deviation grows with the amount of crystal material in the optical system.

4.6.   Conclusions

In this chapter we made an analysis of the influence of the spatially induced birefringence in lithographic optical design. First we discussed the method and approaches in physical optics which can be used to describe the polarization effect and its influence on the image quality. The expression for the Strehl ratio in the case of a high NA optical system including polarization was derived.

From this chapter we have also seen that the spatial dispersion effect in lithographic projection systems includes two basic effects: the phase retardation and the ray bifurcation. The first effect can be computed on the basis of polarization ray tracing with the help of Jones matrices. We examined the possibilities for the BISD analysis, offered by modern software tools such as Code V. The accuracy of the effect computation and some program settings were discussed as well. For the estimation of the retardation value, the standard deviation of the retardation over the pupil is useful. The analysis we made allows to conclude that the magnitude of the phase retardation is high enough to cause serious problems for obtaining the required resolution and that it must be reduced.

For the second BISD consequence - the ray bifurcation and deviation - a special method for computation of the maximum ray deviation was offered. If the magnitude is sufficiently large, this second effect has a much less regular character, cannot be corrected and can be evaluated by computing the maximum ray deviation. The method described here can be a starting point for future independent verifications of the statement that, once the phase retardation is compensated, ray bifurcation has a negligible effect on the imaging quality of DUV lithographic systems.

5. Compensation of phase retardation

5.1. Compensation of phase retardation: Basics

The basic idea of the phase compensation is the following. It is not possible to avoid the spatial birefringence effect completely (that would require zero angles between rays and an optical axis of the crystal), but it is possible to achieve a certain distribution of the retardation magnitude and retardation orientation in the pupil plane. Since the contribution of components (or group of components) to the total phase retardation is additive, it is possible to combine two predefined distributions of the phase retardation with the same magnitude but orthogonal orientation. Summation these two distributions can cancel each other (see Figure 5.1.2). The different methods proposed for obtaining desired phase distribution are discussed in this chapter.
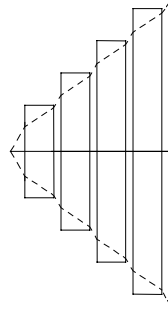
Figure 5.1.1 Simple optical system for modeling of the BISD compensation
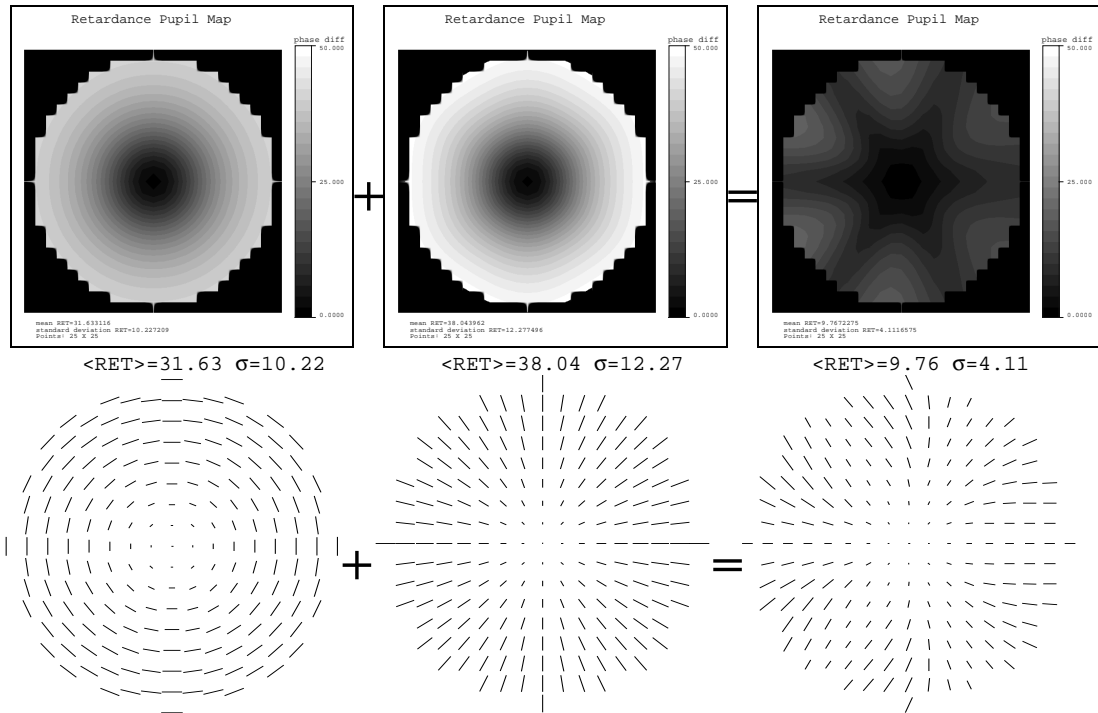
Figure 5.1.2 Basic compensation of the phase retardation. Two components with the same distribution of the retardation magnitude but orthogonal retardation orientation give much smaller resulting retardation magnitude.

According to our experience the effect can be considered as compensated if the value of the standard deviation of the residual phase retardation does not exceed 10-20°, depending on specifications of the objective. In this case the contrast loss caused by the BISD-effect is smaller than the image deterioration caused by aberrations and

other unavoidable polarization effects induced by high-NA, coating, residual stress-induced effects i.e. [38], [39].

There is not too much difference between phase compensation for 193 and 157 nm objectives, because the character of the effect remains the same and only the magnitude of the linear birefringence scales up with lowering the wavelength.

For investigation of the phase retardation we will first use the model shown in Figure 5.1.1. This is the simplest optical system possessing high NA where all components give the same contribution to the total retardation value.

5.2.   Crystal Axis Clocking

One of the major obstacles for the BISD compensation is the possible effect of asymmetry of the pupil map around the center of the pupil. For preserving the symmetry only three types of directions <001>, <110> and <111> can be selected as an optical axis. The directions <001> and <110> have an advantage over <111> because for them the pupil map of the phase retardation distribution does not change sign as a function of the angle between the ray and the optical axis, but along <110> we have a maximum of the effect. Generally it is possible to select an arbitrary direction [uvw] as an optical axis but in that case both the BISD compensation and the technological issues may be much more difficult.

From the point of view of crystal production the components oriented along the <111> direction are preferable because for this direction the residual stresses are minimal. Crystals grown along <100> and <011> require additional effort from the industry.

The regular nature of the BISD may lead to the "clocking" solution, which is widely used today in 248 and 193-nm lithography in order to adjust for aberrations caused by deviations of the lens surfaces [40]-[45]. Clocking adjusts the lens elements by rotation in a plane perpendicular to the system axis. However, using clocking for the compensation of phase retardation limits the possibility of using clocking later on to adjust for the unavoidable defects of the lens elements. Nowadays the UV-lithography tools have objectives, which use mostly the wavelength of 193 nm. They consist of more than twenty lenses, and about one third of the optical components are made of calcium fluoride. The assembling of an objective is a tedious task, because the tuning operation is very difficult. The stress-induced birefringence effect and local deviation of the surface profile should be estimated for every lens component and the assembling is done only after the mutual compensation is realized.

The references, mentioned above, discuss the compensation approach for certain types of optical systems. We will summarize all approaches and describe the general strategy of the compensation of phase retardation in what follows.

The first step is the creation of a circular distribution of the phase retardation over the pupil. As it can be observed from Table 4.2.2, different crystal orientations along the system axis have different angular symmetry of the retardation distribution. It is thus possible to tune the separate components to achieve the desired distribution of the retardation over the pupil by adjusting of the phase retardation contributions of several components. So, by combining lenses with orientations <001>-0° and <001>-45° for the <001> direction or <111>-0° and <111>-60° for the <111> direction, we can achieve almost circular distributions of the phase retardation magnitude (see Figure 5.2.1 and Figure 5.2.2). It is seen that regions in the pupil with low phase retardation overlap with those having a high phase retardation value. These two rotated components (or groups of components) with overlapping pupil maps should give the same contribution.

<RET>=44.41 σ=19.39   <RET>=44.29 σ=19.34   <RET>=85.42 σ=27.40

<001>-0°   <001>-45°   <001>-0°+<001>-45°
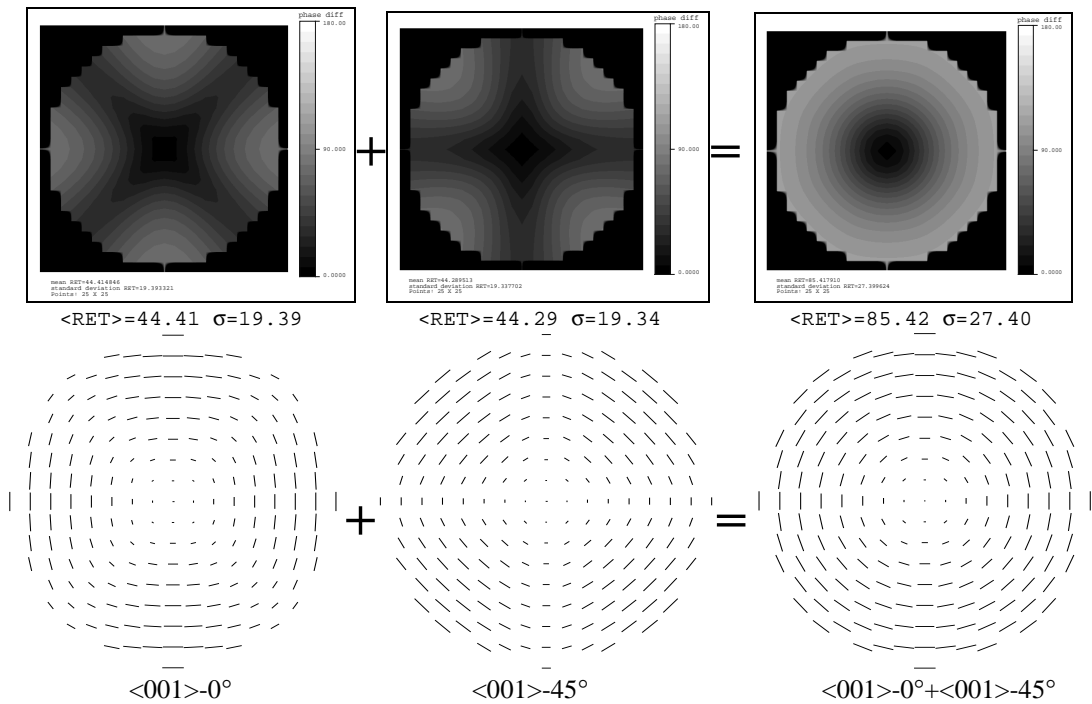
Figure 5.2.1 Obtaining a circular distribution of the phase retardation for the <001> direction. The resulting magnitude of the phase retardation has a circular distribution and tangential orientation.

<RET>=56.47 σ=23.57   <RET>=56.47 σ=23.57   <RET>=57.08 σ=18.54

<111>-0°   <111>-60°   <111>-0°+<111>-60°
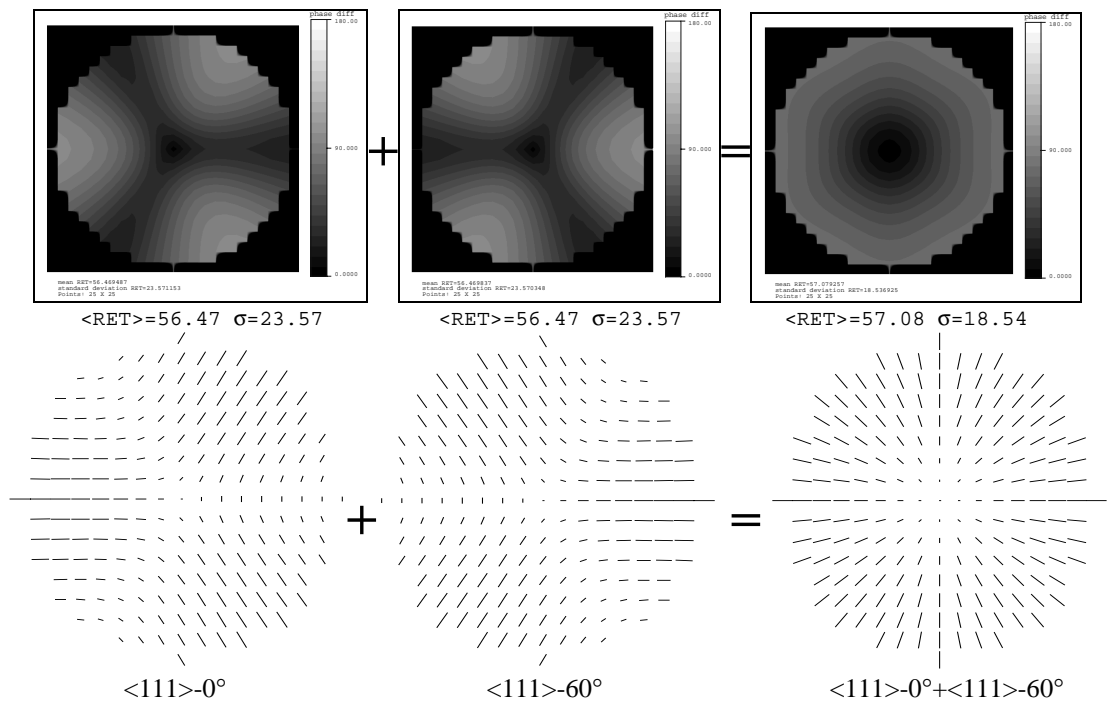
Figure 5.2.2 Obtaining a circular distribution of the phase retardation for the <111> direction. The resulting magnitude of the phase retardation has a circular distribution and the radial orientation.

<RET>=34.33 σ=14.65   <RET>=34.33 σ=14.65   <RET>=32.07 σ=20.17

<011>-0°   <011>-90°   <011>-0°+<011>-90°

<RET>=34.30 σ=14.65   <RET>=34.30 σ=14.64   <RET>=32.20 σ=20.12

<011>-45°   <011>-135°   <011>-45°+<011>-135°

<RET>=45.18 σ=15.54

Σ Total (<011>-0°+<011>-90°+<011>-45°+<011>-135°)
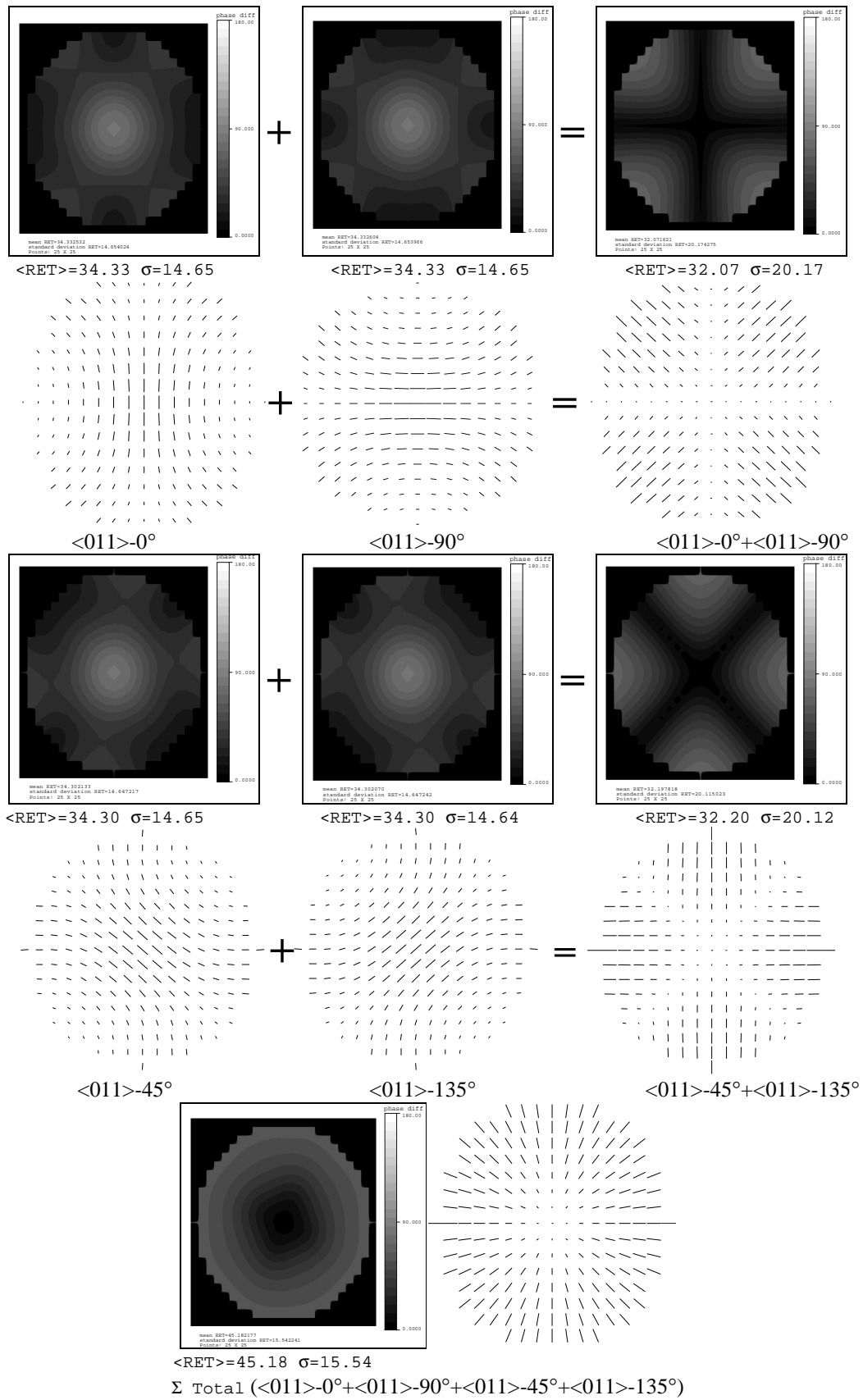
Figure 5.2.3 Obtaining a circular distribution of the phase retardation for <011> direction. The resulting magnitude of the phase retardation has a circular distribution and radial orientation. This approach requires four components. The intermediate cumulative pupil maps have cross-like retardation distributions.

<RET>=31.63 σ=10.22   <RET>=38.04 σ=12.28   <RET>=9.77 σ=4.11

<001>-0°+<001>-45°   <111>-0°+<111>-60°   Σ Total

a)

<RET>=25.60 σ=7.65   <RET>=31.15 σ=10.82   <RET>=4.98 σ=1.88

<001>-0°+<001>-45°   <011>-0°+<011>-90°+   Σ Total
                             <011>-45°+<011>-135°
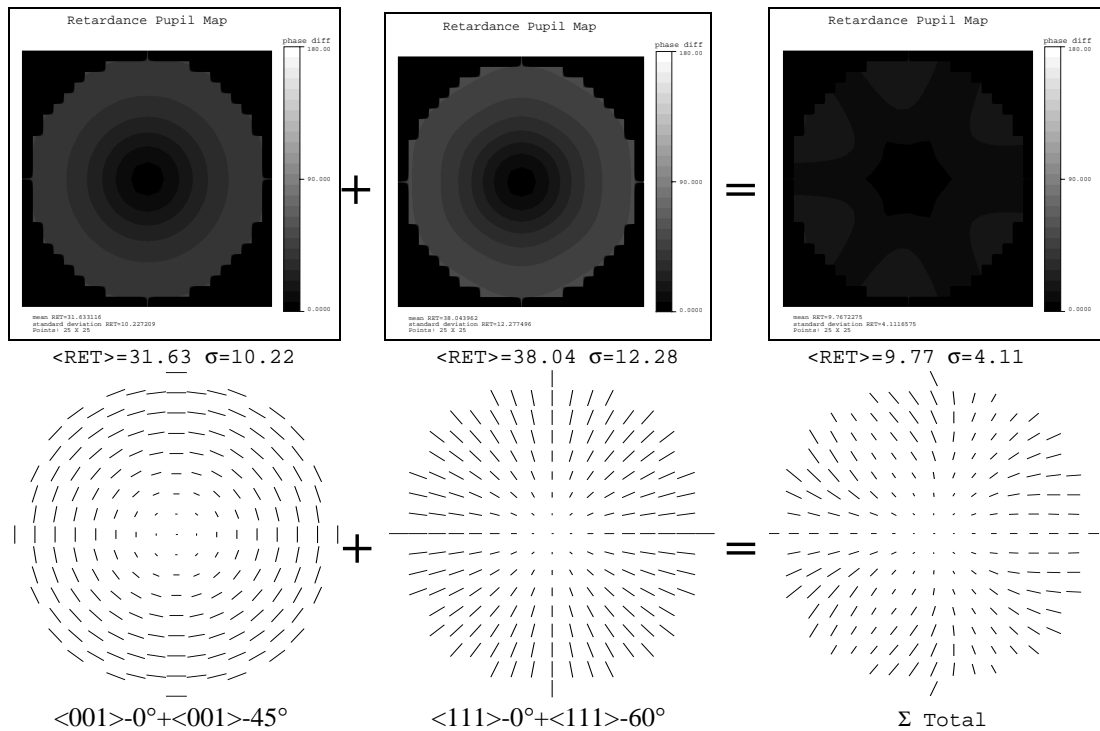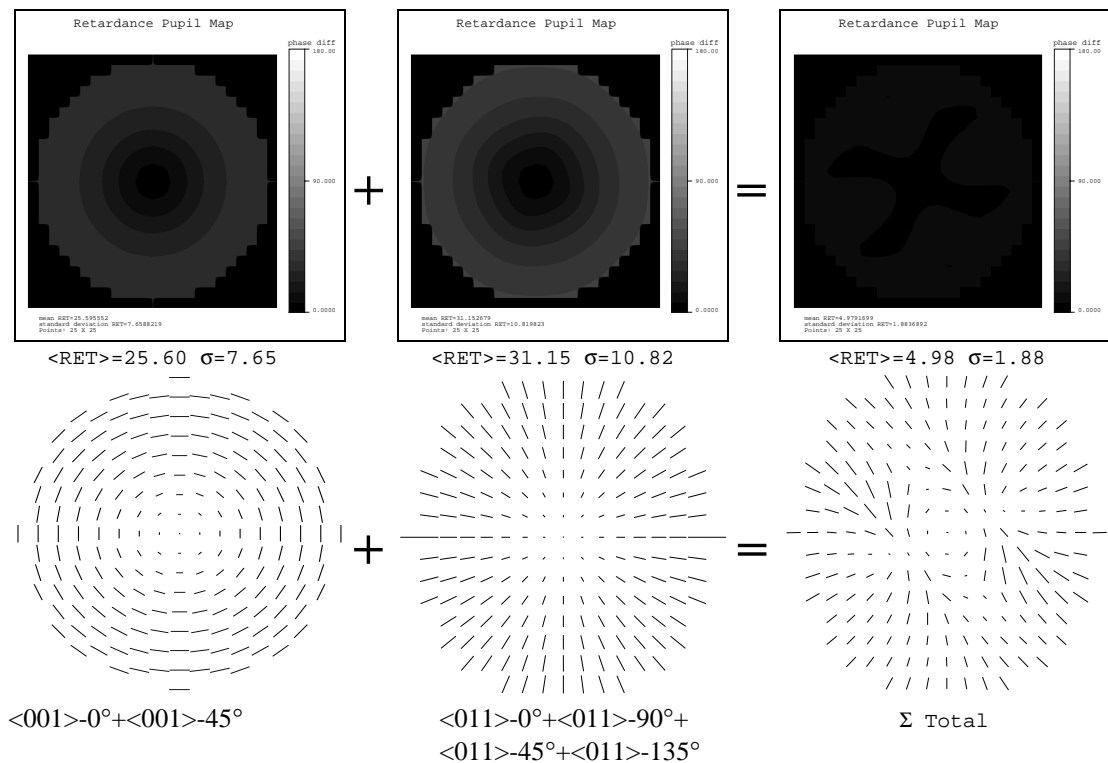
b)

Figure 5.2.4 Nulling the phase retardation by crystal axis "clocking". Two sets of components with the same distribution of the phase retardation but having opposite orientation result in a very small total retardation value. a) (<001>-0°+<001>-45°)+(<111>-0°+<111>-60°) combination; b) (<001>-0°+<001>-45°)+(<011>-0°+<011>-90°+<011>-45°+<011>-135°) combination

It is seen from the figures that, as a result of the combination of <001>-0° and <001>-45°, we have tangential orientation of the phase retardation for any pupil point, and for the couple <111>-0° and <111>-60° we have radial orientation of this value. It should be pointed out that for two plates <111> and <001> with equal thicknesses the magnitude of the phase retardation for the <111> direction is lower, i.e. the path length in glass for this components should be larger in order to obtain the same contribution as for the <001> direction.

It is also possible to obtain a circular distribution for the <011> direction (see Figure 5.2.3). However, in this case at least four components should be used for obtaining a circular phase retardation distribution but the resulting magnitude is about 20% less than in case of the <001> direction. In principle, the shown pupil maps allow to combine them in any way in order to obtain desired phase retardation distributions.

The second step is the nulling of the phase retardation. By inspecting the phase retardation pupil maps shown in Figure 5.2.1, Figure 5.2.2 and Figure 5.2.3 it can be seen that the resulting orientation of the retardation for the <001> clocked pair is orthogonal to the orientation for the <111> clocked pair (or the orientation for the <011> clocked quartet). That means that the retardation has opposite sign for these combinations. Thus when the magnitude of the retardation is also equal then combining these lens blocks consisting of two or four lenses can be used to reduce or null out the total retardation value. The results of this compensation can be seen in Figure 5.2.4.

We can also find the initial value of thickness of the <111> (<011>) and <001> plates in Figure 5.1.1 for such a compensation. These thicknesses should have the same ratio as the mean retardation values of the two sets of components. For instance, for the <111> and <001>, this ratio is 1.5 and this value can be further optimized. The exact values obtained after optimization are $\Sigma d_{111}/\Sigma d_{001} = 1.82$ for the <111>-<001> compensation scheme and $\Sigma d_{011}/\Sigma d_{001} = 4.08$ for the <011>-<001> scheme. However this coefficient is not a constant and for real systems should be determined numerically for each type of optical system.

5.3.   Crystal clocking applied to a practical system

We will now apply the crystal axis clocking approach to the optical system shown in Figure 4.4.2. In the first stage, we compute the phase retardation contribution of components for the three basic crystal orientations and then we classify the components according their values (see Table 5.3.1 and corresponding grayscale maps in Figure 4.4.2). In this case we use a combination of <111> and <001> directions.

In the next step, for forming a circular distribution, we define the crystal orientation of certain components. As it is seen from Table 5.3.2 we were able to achieve equal cumulative retardation value for two directions in each of the two couples of the <111> and <001> directions. The ratio between the cumulative retardation values for the <111> and <001> directions is chosen to null the total retardation. Finally, the components are oriented along the direction shown in the last column of Table 5.3.1. We note that in this example system some components, close to the spherical mirror, are used double pass and should have the same crystal orientation in both directions. Moreover for the <111> direction, the components which have pupil maps rotated over 180°, because of opposite angle between marginal ray and optical axis, are shown as well (between brackets we show the orientation entered into the software).

The result of this compensation is shown in Figure 5.3.1. The presented pupil map shows that the phase retardation is very well balanced and the image of the 2D test-

object is drastically improved. For comparison, we also show the image of the 2D test-object for the same objective in the absence of the BISD-effect. If a further improvement is required then it is possible to adjust the thickness of components. In this case the merit function for optimization should be extended by adding the value of the standard deviation of retardation.

Table 5.3.1 Phase retardation contribution of the separate components in the example system

Component #	Surface #	Phase retardation contribution for <001> direction	Phase retardation contribution for <111> direction	Crystal orientation of the component
1	46	59.32751	89.97305	**111-0°**
2	44	40.50317	68.84210	**001-0°**
3	12	24.87031	50.15022	**111-60°**
4	9	24.21614	49.53407	**111-60°**(as #12)
5	40	20.76436	37.54656	**001-45°**
6	42	8.123430	23.39501	**001-45°**
7	35	4.667793	15.98327	**001-45°**
8	14	3.341908	20.71335	**001-45°**
9	7	2.976251	19.91663	**001-45°**(as #14)
10	25	2.056147	15.77146	**001-0°**
11	5	1.338430	1.991897	**001-45°**
12	31	1.325586	2.469966	**001-45°**
13	16	1.313316	2.550029	**001-45°**(as #5)
14	29	1.286954	3.685012	**111-60°**
15	23	1.121591	16.89479	**111-0°**(111-60°)
16	33	0.813918	6.257399	**111-0°**(111-60°)
17	38	0.544681	10.22191	**001-0°**
18	27	0.474838	13.69446	**001-0°**
19	2	0.086460	9.325174	**111-60°**(111-0°)

Table 5.3.2 Combining components with different crystal orientation for forming a circular distribution of the phase retardation and its compensation

Orientation	**001-0°**	**001-45°**	**111-0°**	**111-60°**
	2.056147	1.33843	16.89479	9.325174
	0.474838	2.976251	6.257399	49.53407
	0.544681	3.341908	89.97305	50.15022
Contribution of Components	40.50317	1.313316		3.685012
		1.325586		
		4.667793		
		20.76436		
		8.12343		
Σ	43.57883	43.85107	113.1252	112.6945

The BISD compensation for off-axis points is more difficult, because the distribution of the birefringence is not symmetric, but in general the behavior for such a field point is comparable to that of the axial point. In all cases we studied the compensation for the axial point helps the compensation for the off-axis points. In order to demonstrate this, we show the pupil map for the off-axis (with image height 16.4 mm) point for the compensated on-axis system discussed above. It is seen that in spite of increasing the

mean retardation value the standard deviation and the image quality are acceptable. For off-axis points it would be useful to have software support for the arbitrary choice of the crystal orientation during optimization.

- 001-0°
- 001-45°
- 111-0°
- 111-60°

a)

$<RET>=18.44$ $\sigma=7.43$
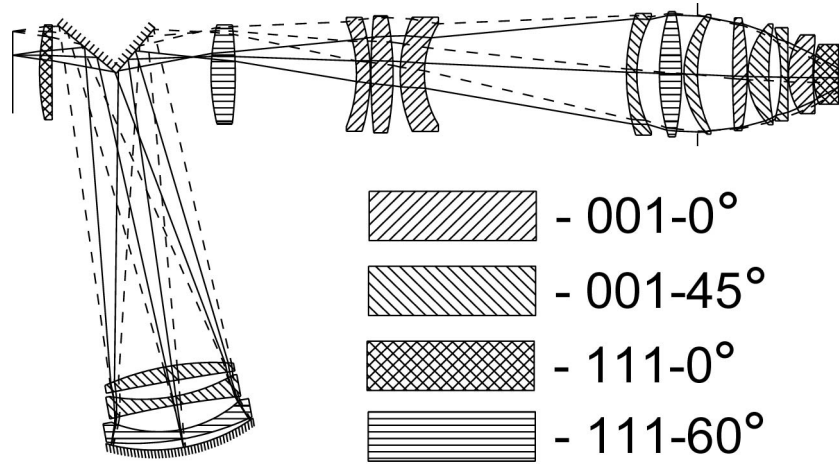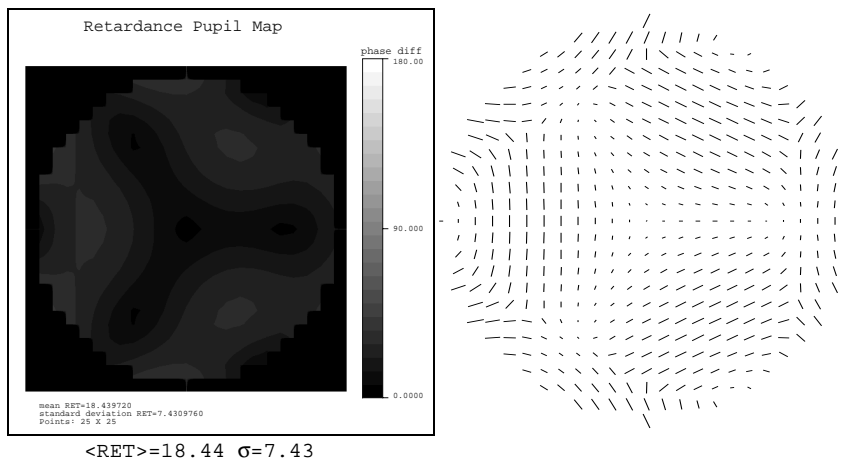
b)
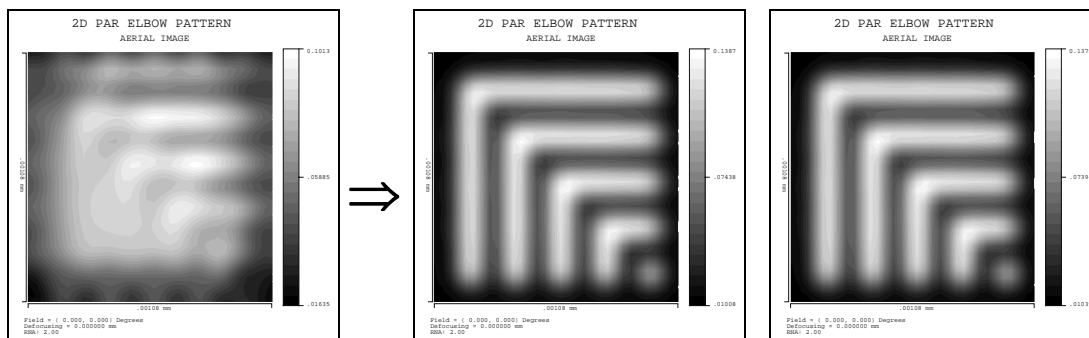
c)   **d)**   **e)**

Figure 5.3.1 Results of the phase retardation compensation (ray bifurcation is not included in the simulation): a) optical system with compensated phase retardation (the crystal orientation of the components is shown); b) pupil map for the compensated system; c) simulated image of the test-object for the uncompensated system; d) simulated image of the test-object for the compensated system; e) simulated image of the test-object for system without including the BISD-effect.

Generally speaking each type of lithographic objective requires a specific compensation approach. For instance, the optical system shown in Figure 2.5.4 [46] consists of eight optical components and it has a relatively small total track in glass. However, the approach discussed above cannot be applied because the phase retardation given by different components have different order of magnitude. The small number of components is not sufficient for the use four basic crystal orientations (<001>-0°, <001>-45°, <111>-0°, <111>-60°) which should have the same order of magnitude of the phase retardation in order to correct it.

<RET>=45.57 σ=16.85

a)

b)
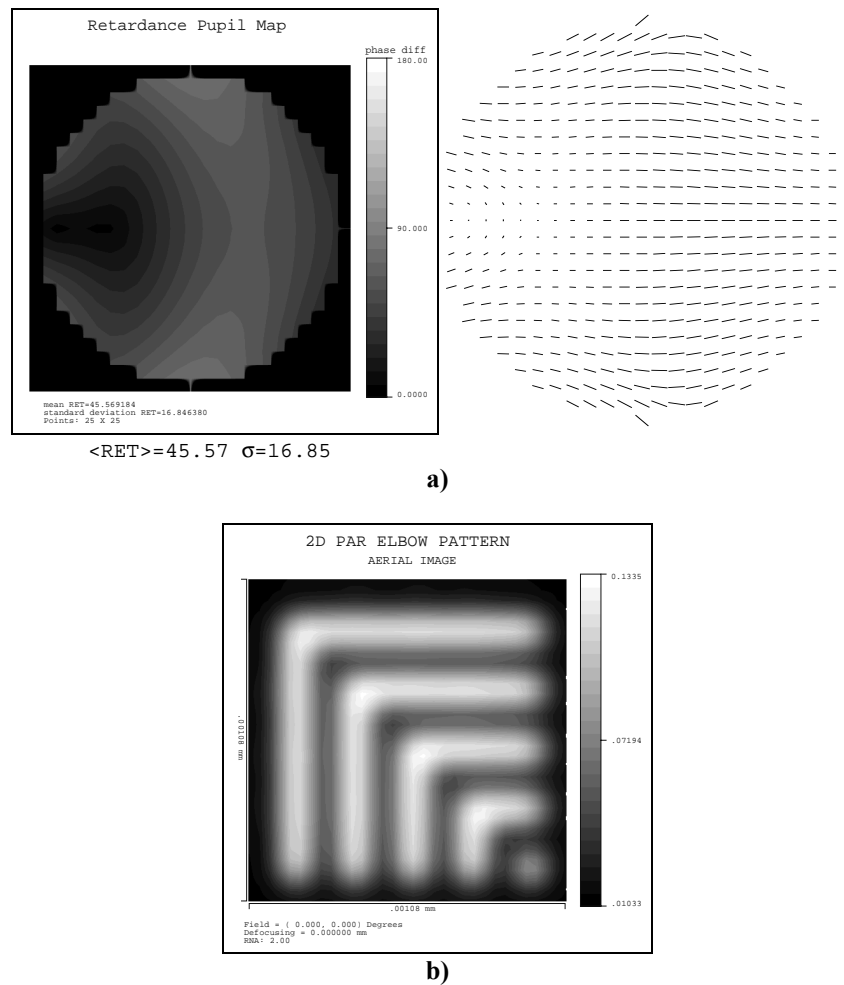
Figure 5.3.2 Results of the phase retardation compensation for off-axis image point: a) pupil map; b) image of the test-object for the optical system compensated with clocking approach.

For the compensation of phase retardation in this optical system another approach was applied. It turns out that for this system the contributions of separate components are of the same order of magnitude if they are oriented along <011> directions. Moreover most components are situated in the part of the system where the marginal ray angle with the optical axis is not large and the pupil maps of certain components possess only the central zone of the typical pupil maps for the <011> directions in Figure 4.4.3. It is seen from this figure that in the region, close to the optical axis, the orientations of the phase retardation for crystal orientations <011>-0° and <011>-90°, are orthogonal. Thus we can use only one clocked crystal orientation in order to compensate the phase retardation. The selection of the orientation of the components in the optical system was done on the basis of the method, described above, with classification by the single component contribution in the cumulative phase

retardation. The orientation of the components, cumulative pupil maps for <011>-0°
and <011>-90° and the final compensation result are shown in Figure 5.3.3

As in the case of the first example, such an arrangement allows compensation the
effect without or with minor additional optimization and does not break the
geometrical aberration correction. In all cases the final compensation can be done by
adjustment of the lens thicknesses.
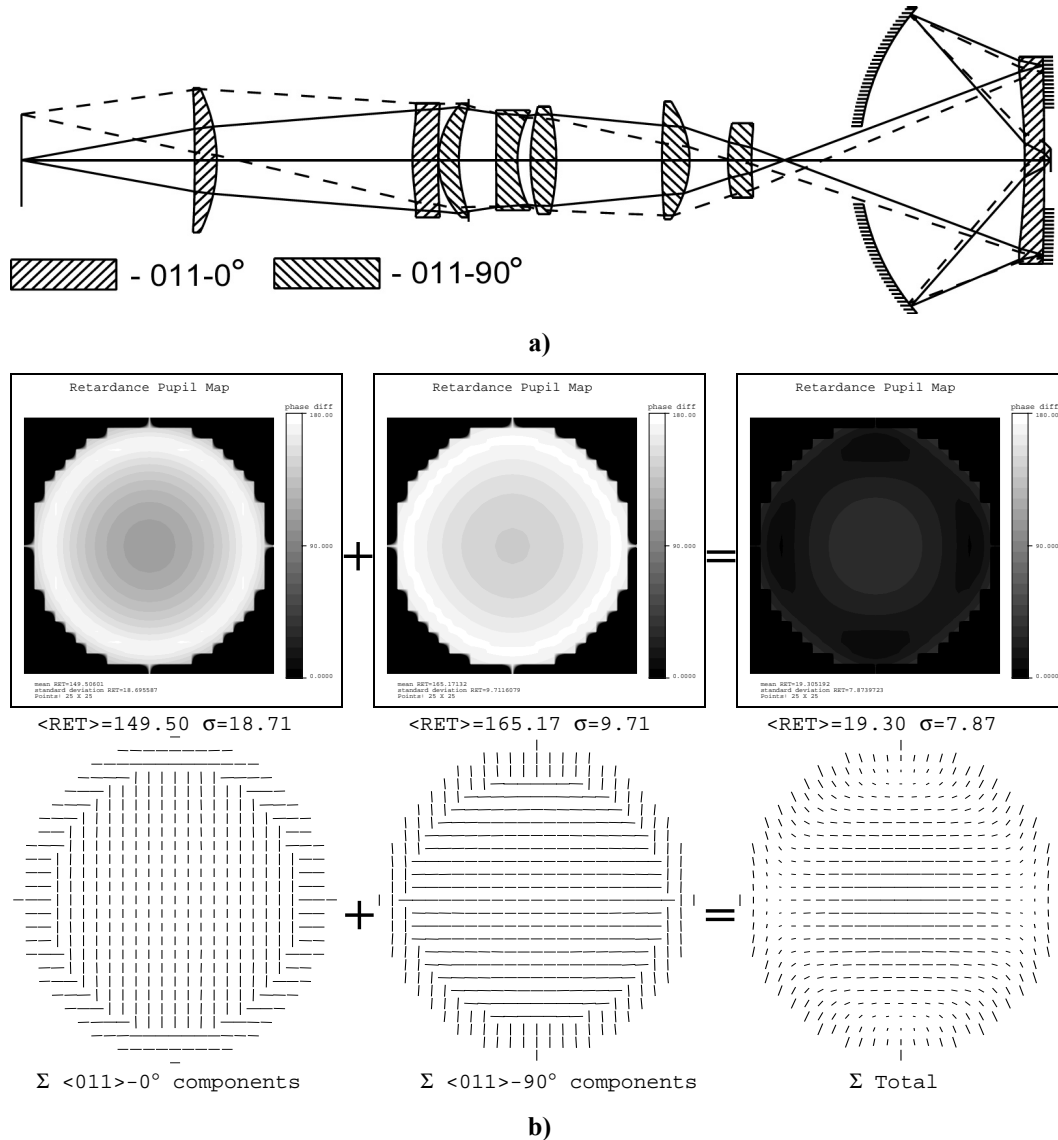
Figure 5.3.3 Compensation of the phase retardation in a DUV lithographic system with small number of components. a) Optical system layout [46]; b) phase retardation pupil maps of cumulative retardation for <011>-0° and <011>-90° directions and total retardation value.

On the basis of our experience we propose a general strategy with the following steps:
- Computation of the pupil maps for basic crystal orientations (<001>, <111>, <011>) for each component assuming that this component is the only one with the phase retardation.
- Classification of components according to their contribution to the cumulative phase retardation.
- Select a compensation strategy depending on number and position of components, thicknesses, balance contributions, total track in glass etc.
- Apply this compensation strategy to the optical system.

Final optimization including rotation of crystals, adjustment of lens thickness and curvatures.

5.4.   Correction of the phase retardation with the aid of stress-induced birefringence

Another compensation approach describes the use of a photoelastic effect for the BISD compensation [47]. It was already mentioned that the stress-induced birefringence has a similar nature [19], [20]. The stresses applied for obtaining stress-induced birefringence can be caused by tension, pressure, changing thermal gradients in crystals or by ion diffusion.

By analogy with Eq. (3.3.1) we can write that in the case of the photoelastic effect the impermeability tensor ε_{ij}^{-1} has an additional stress-induced contribution

$$\varepsilon_{ij}^{-1}(\omega,\sigma) = \varepsilon_{ij}^{-1}(\omega)\delta_{ij} + q_{ijlm}(\omega)\sigma_{lm}, \tag{5.3.1}$$

where q_{ijlm} is the piezo-optical coefficient matrix, and σ_{lm} is the stress tensor. However from Eq. (3.3.1) we have

$$\varepsilon_{ij}^{-1}(\omega,\mathbf{k}) = \varepsilon_{ij}^{-1}(\omega)\delta_{ij} + \beta_{ijlm}(\omega)k_l k_m. \tag{5.3.2}$$

Thus the complex variance of ε_{ij}^{-1} can be written as

$$\Delta\varepsilon_{ij}^{-1} = q_{ijlm}\sigma_{lm} + \beta_{ijlm}k_l k_m. \tag{5.3.3}$$
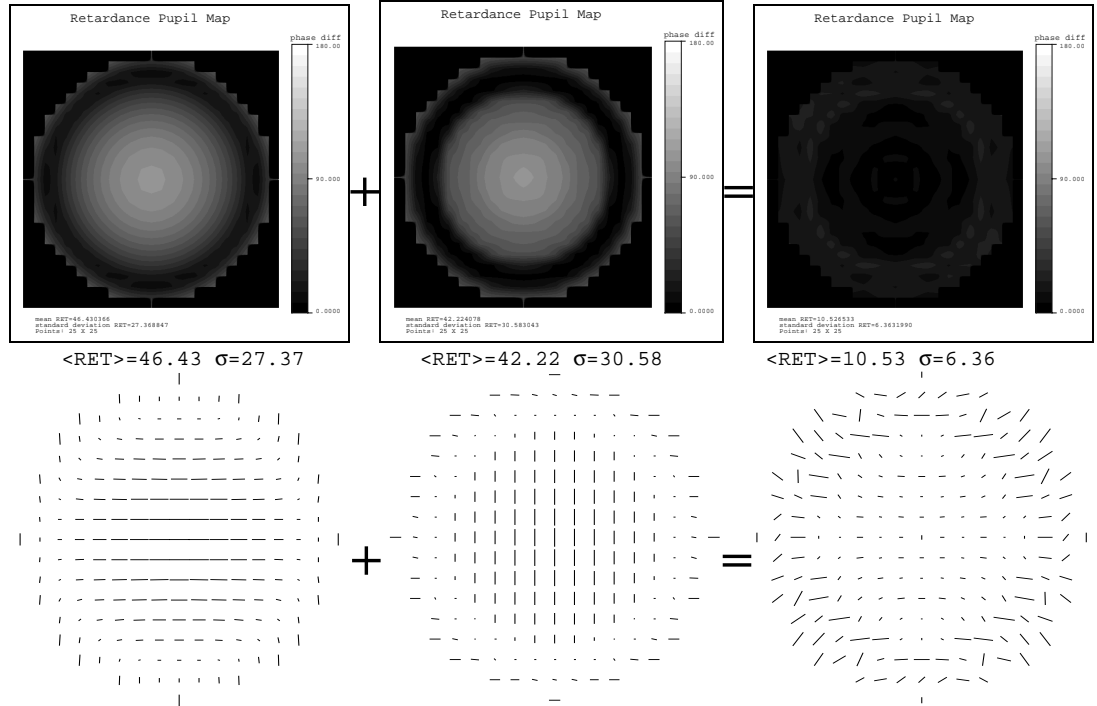
Figure 5.4.1 Compensation of the phase retardation by stress-induced birefringence. In the left picture the total phase retardation of the system without applied stress is shown. In the middle we see the phase retardation pupil map of the compensator. In the right hand picture, the total phase retardation distribution is presented.

This effect can also be modeled and analyzed with the help of modern optical software such as Code V [47]-[50]. For modeling stress-induced birefringence in Code V, two files should be supplied for each optical element [31]. The first one represents the magnitude of the birefringent index difference as a function of the position on the surface and is in units of nm/cm i.e. the data represents the increase in optical path of the slow component as compared to the fast component per unit length.

The second file represents the orientation, in degrees, of the crystal axis of the medium (i.e., the direction of the stress vector) with respect to position on the surface. In Figure 5.4.1 we show the example of compensation of the phase retardation for the optical system shown in Figure 2.5.4. In this case we apply stress to the component situated near the system stop because in this case the contributions for all field positions are similar. As it is seen from the drawings, the effect can be very well compensated. However, in practice it is very difficult to correct the large retardation value without risk of destroying the components. It is also unclear how to change the orientation of the phase retardation when tensions or stresses should alternate within one component. The sharp separation between orientation of the phase retardation in the neighboring pupil positions should be avoided as well. In our view this method can be successfully applied for the compensation of the residual phase retardation remaining after clocking.

5.5.   Correction of the phase retardation with birefringence compensator

Some references suggest the use of the natural crystal anisotropy for the correction of spatial dispersion [51]. There are media, transparent in the deep UV range, which have a too large birefringence value to be used as lenses, but thin compensator plates produced from such a material can contribute a small birefringence value. Examples of these materials with natural birefringence are uniaxial crystals such as SiO_2 (crystal quartz), Al_2O_3 (sapphire), MgF_2 (magnesium fluoride), LaF_3 (lanthanum fluoride).

One-plate retardation compensator

A simple phase retardation compensator can be produced with one plate. For the radially symmetric distribution of the phase retardation the optical axis of the crystal should be oriented along the system axis. The example of this one-plate compensator for the point object on the optical axis is shown in Figure 5.5.1.
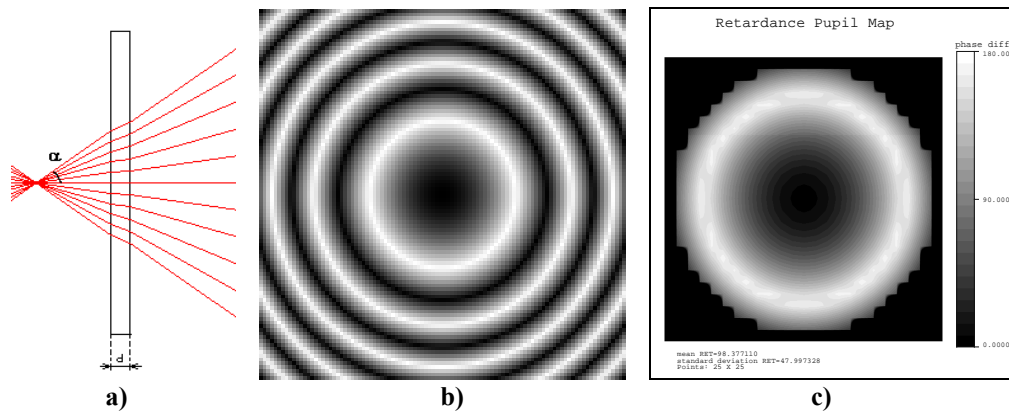
Figure 5.5.1 One plate retardation compensator: a) one-plate compensator, b) theoretically computed retardation pupil map; c) pupil map obtained with optical design software.

In this case the phase retardation value is defined by the expression

$$\delta = \frac{2\pi(n_e - n_o)d}{\lambda} \frac{\sin^2\alpha}{n_0^2\sqrt{1 - \sin^2\alpha / n_0^2}} , \qquad (5.4.1)$$

where α is the angle between the ray and the optical axis and d is the plate thickens. The circular distribution of the phase retardation distribution suggests to use it for the compensation of the circular distribution of the phase retardation obtained with <001>-0° and <001>-45° or <111>-0° and <111>-60° combinations (see Figure 5.2.1

and Figure 5.2.2). In this case the first "retardation ring" in the distribution shown in Figure 5.5.1 b) can be superimposed with the ring obtained by clocking. The position for the compensator in the optical system can be chosen near the object point (for adjustment of the retardation value for different field points) or near the system stop.

Two-component compensator

In this compensation approach we use two plates. One of them is made from a cubic crystal material and the other from a crystal with natural birefringence, transparent in the deep UV (SiO_2, Al_2O_3, MgF_2, LaF_3). The indices of refraction should be as close as possible. The outer surfaces of these plates are plane and the inner surfaces are identical and separated by a thin air space. Therefore this thin-plate construction doesn't actually influence the ray path but has a great impact on the state of polarization and consequently on the phase retardation of the rays. The inner surface profile can be optimized in order to minimize the total phase retardation of the objective. This plate construction can be positioned e.g. in the stop of the optical system.

CaF_2 SiO_2
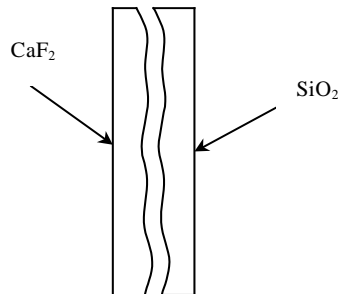
Figure 5.5.2 Two-component compensator.

By changing the shape of the inner profile it is possible to obtain various retardation pupil maps (Figure 5.5.3). More complex distributions or combinations of the shown maps are possible.
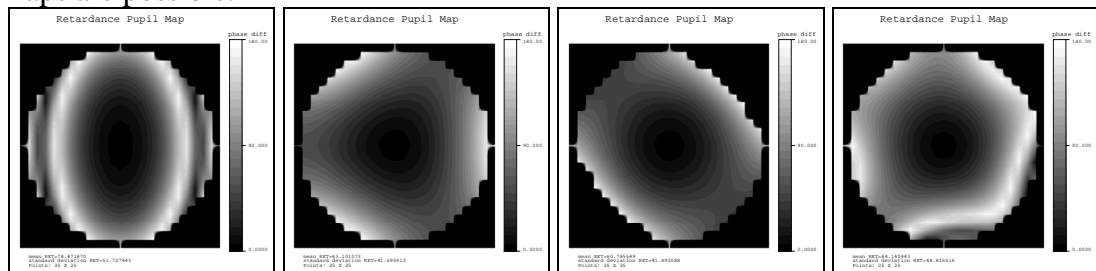
Figure 5.5.3 Phase retardation pupil maps obtained with different inner profiles of the two-plate compensator. The shape of the surface was modeled with the aid of Zernike polynomials.

In principle, this approach offers the widest possibilities for compensation because the shape of the surface can be tuned in order to adjust it to the phase retardation distribution to be compensated.

5.6. Conclusions

We have discussed three basic approaches for the compensation of the phase retardation. All concepts assume the presence in the optical system of two groups of components contributing with almost the same distribution of the retardation magnitude but with the orthogonal retardation orientation.

The first concept (clocking) uses the different dependence of the phase retardation for different crystal orientations. It was shown that by combining them in a certain way it

is possible to reduce the image quality loss significantly. Several approaches for this combination of the crystal orientation were discussed.

It is also possible to use the photoelasticity effect for the phase retardation compensation. It this case it is possible to introduce stress or tension in the crystal body to achieve the desired distribution of the retardation. This approach can be quite successful but has "mechanical" limits.

The last approach exploits natural crystal birefringence for compensation. The results of the compensation are also promising; for instance, the retardation distribution can be asymmetrical with respect to the center of the pupil, which is difficult to realize with the clocking strategy.

The main conclusion of this chapter is that the phase retardation effect in deep UV lithography can be compensated. This compensation requires an additional effort from the optical designer and limits certain other possibilities if the optical design; but in our view the birefringence effect can be reduced to a sufficiently low level.

6. Optimization

6.1. General optimization problem

In our competitive world, only the best feature (safest, cheapest, fastest, etc) is good enough. This is why optimization is very frequent in application. Optimization is the problem of finding the best set of admissible conditions to achieve the objective, formulated in mathematical terms. The solution of this task is a necessity in many areas, such as transportation logistics, packing and other object arrangement problems, potential energy models in computational physics and chemistry, classification and visualization, model fitting to data (calibration), forecasting in economics and finance etc [52]-[55].

The quality of a solution is measured by a single number, a value of the error function, sometimes also called merit function (MF), $f(\mathbf{x})$ which can be of any nature (price, distance, energy etc). In this case $\mathbf{x} = (x_1, x_2, ... x_n)$ is the set of optimization parameters varied to achieve the goal and n is a dimensionality of the problem. Thus $\mathbf{x}$ defines a point in an n -dimensional variable space X, which is composed of all possible combinations of variables $x_i, i = 1, 2, ..., n$. In general case we are interested in finding the extremum of $f(\mathbf{x})$, but without loss of generality, we can limit our discussion to a minimization problem, because a maximization problem can always be transformed into minimization problem by negating the error function. Often the range of optimization variables is limited by boundary conditions and the additional relationships between variables are required. These optimization constraints are expressed as a function of parameters that must be strictly equal or less some defined limit.

Depending on whether the variables take discrete or continuous values we can classify optimization problems as follows:

- *Continuous problems:* $\mathbf{x}$ is a vector of continuous variables;
- *Discrete problems:* $\mathbf{x}$ is a vector of discrete variables, where each component x_i can take discrete and finite values, for instance integer numbers (pieces).
- *Mixed-integer problems:* some variables take discrete values while others take continuous ones.

Mathematically the problem of optimization can be formulated as

$$\left. \begin{array}{c} \text{minimize } f(\mathbf{x}) \\ \text{subject to } g_i(\mathbf{x}) \le 0, \ h_i(\mathbf{x}) = 0, \mathbf{x} = (x_1, x_2, ... x_n) \end{array} \right\} \qquad (6.1.1)$$

where $f(\mathbf{x})$ is an error function that we want to minimize, $h_1, h_2, ..., h_m$ is a set of m equality constraints, and $g_1, g_2, ..., g_k$ is a set of k inequality constraints. The minimum is an unconstrained stationary point when

$$\nabla f(\mathbf{x}) = \left(\frac{\partial f}{\partial x_1}, \frac{\partial f}{\partial x_2}, ..., \frac{\partial f}{\partial x_n} \right) = 0, \qquad (6.1.2)$$

where $\nabla f(\mathbf{x})$ is gradient of $f(\mathbf{x})$. This is a vector field that, for a given point x, points the direction of greatest increase of $f(\mathbf{x})$.

Generally there are three ways for implementing constraints during optimization.

1. Eliminating constrains

The simplest way to satisfy constraints is to eliminate certain variables using constraint equations and solve a reduced problem of minimization of $f(\mathbf{x}^*)$. However it is not possible if the dependence is highly nonlinear as it mostly happens.

2. Penalty function

Consider, for simplicity, a problem with one equality and one inequality constraint. In this case a new minimization function is constructed in the following form

$$f(\mathbf{x}) + p(h^2(\mathbf{x}) + g^2(\mathbf{x})), \tag{6.1.3}$$

where $p \gg 1$ and the inequality constraint $g(\mathbf{x})$ is taken into account only when it is violated. In this case the minimization function increases rapidly, forcing the optimization routine to solutions where the constraint is not violated.

3. Lagrange Multipliers

This is the advanced way for implementing constrains. With one equality constraint, in order to satisfy the constraint the solution should lie on the surface $h(\mathbf{x}) = 0$. At the constraint minimum $\nabla f(\mathbf{x})$ is parallel to $\nabla h(\mathbf{x})$ i.e.

$$\nabla f(\mathbf{x}) = \lambda \nabla h(\mathbf{x}). \tag{6.1.4}$$

In the case of *n*-constrained optimization the following relationship is required

$$\nabla f(\mathbf{x}) = \lambda_1 \nabla h_1 + \lambda_2 \nabla h_2 + ... + \lambda_n \nabla h_n, \tag{6.1.5}$$

where the scalar values $\lambda_1, \lambda_2, ..., \lambda_n$ are called the Lagrange multipliers. This technique can be generalized for inequality constraint as well [56].

In general case the dependence $f(\mathbf{x})$ is non-linear and it is not possible to predict its behavior everywhere in the domain permitted by constrains. The optimized function may also posses many maxima and minima. The maxima and minima of $f(\mathbf{x})$ can either be *global* (the highest or lowest value within the whole variable space X) or *local* (the highest or lowest value within some certain region around the given initial point). Accordingly we can classify any optimization strategy as local optimization (which finds from the starting point one of the nearest local minima) or global optimization (which finds the global minimum). Normally the local optimization is an iterative process performing step by step a descent to the local minimum.

Local optimization methods

The most well-known local optimization strategies can be listed as follows [57]:

1. Bracketing a minimum

A region in the X space containing an expected local minimum is bounded by a group of points: in 1D by two points (a line segment), in 2D by three points (a triangle), etc. After that a direction of a decreasing function is found and the new estimation region is defined.

2. Downhill Simplex Method (Nelder-Mead)

This method assumes to enclose the local minimum inside an irregular volume defined by an *n*-dimensional convex figure called a simplex. The simplex is bounded by (*n*-1)-dimensional hyperplanes and defined by *n*+1 linearly independent corners, e.g. a tetrahedron for 3D. The simplex dimensions is continuously changing and mostly decreasing and finally it is small enough to enclose the minimum with the required accuracy. The operations of changing the simplex optimally with respect to the function values found at the corners of the simplex are called contraction, expansion and reflection, each of them determines new simplex corner points by linear combinations of existing corner points.

3. Newton's Method

There is a well-known Newton quadratic approximation method for finding a minimum of a function of one variable, which generates a sequence of second degree Lagrange polynomials, and uses them to approximate where the minimum is located [58]. It is assumed that near the minimum the quadratics approximates the shape of the error function with sufficient precision. The resulting sequence of minimums of the quadratics produced a sequence converging to the minimum of the objective function. Newton's search method extends this process to functions of n independent variables. Starting at an initial point, a sequence of iterations can be constructed recursively according the formula

$$\mathbf{x}_{i+1} = \mathbf{x}_i - [Hf(\mathbf{x}_i)]^{-1} \nabla f(\mathbf{x}_i), \qquad (6.1.6)$$

where $Hf(\mathbf{x})$ is the Hessian matrix of $f(\mathbf{x})$ i.e.

$$[Hf(\mathbf{x})]_{ij} = \frac{\partial^2 f}{\partial x_i \partial x_j}. \qquad (6.1.7)$$

If the objective function is well-behaved and the initial point is near the actual minimum, then the sequence of minimums of the quadratics will converge to the minimum of the optimized function.

4. Gradient Descent Method (Steepest Descent)

This method starts at an arbitrary point $\mathbf{x}_i$ and moves, as many times as needed, from point $\mathbf{x}_i$ to the point $\mathbf{x}_{i+1}$ minimizing along the line from $\mathbf{x}_i$ in the direction $\mathbf{g}_i$ of the local downhill gradient $-\nabla f(\mathbf{x}_i)$

$$\mathbf{x}_{i+1} = \mathbf{x}_i - \alpha_i \mathbf{g}_i = \mathbf{x}_i - \alpha_i \nabla f(\mathbf{x}_i), \qquad (6.1.8)$$

where the parameter α_i changes to find the lowest point on the trajectory of the downhill gradient (see Figure 6.1.1). Moving in this way we always move along orthogonal directions perpendicular to the corresponding equimagnitude contours (i.e. the contours along which the function has a constant value). The multidimensional problem in this case is reduced to the one dimensional minimization along the gradient direction.
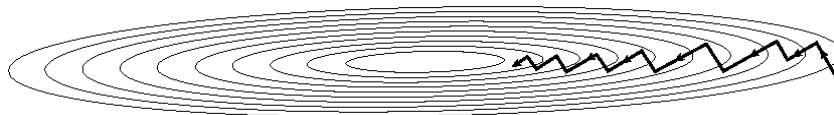
Figure 6.1.1 Converging to the local minimum in the case of Steepest Descent Method. The search directions are orthogonal to each other and to the corresponding equimagnitude contours.

5. Conjugate Gradient Method

This method is based on the gradient descent method but upgraded with an idea of conjugate directions - directions which are independent of each other so that minimizing along each one does not move away from the minimum in the other directions. The conjugate gradient relies on selecting the successive direction vectors as a conjugate version of the successive gradients obtained as the method progresses.
The first step is performed as in the case of the steepest descent method and then the next direction for the line search is constructed to be conjugate to the previous gradient direction, i.e.

$$\mathbf{x}_{i+1} = \mathbf{x}_i - \alpha_i \mathbf{d}_i, \qquad (6.1.9)$$

where

$$\mathbf{d}_0 = \nabla f(\mathbf{x}_0). \qquad (6.1.10)$$

Each next direction is determined as

$$\mathbf{d}_{i+1} = \nabla f(\mathbf{x}_{i+1}) - \frac{\nabla f(\mathbf{x}_{i+1})^T \nabla f(\mathbf{x}_{i+1})}{\nabla f(\mathbf{x}_i)^T \nabla f(\mathbf{x}_i)} \mathbf{d}_i . \qquad (6.1.11)$$

If we minimize along each of a conjugate set of *n* directions we will get closer to the minimum efficiently. If the function has an exact quadratic form, one passing through the set will get us exactly to the minimum. Otherwise we must repeat the cycle a number of times [59].

6. Method of orthogonal directions

This method suggests obtaining conjugate directions without computing the derivative. Sometimes it is not convenient to estimate the gradient $\nabla f(\mathbf{x})$ to obtain the direction in a steepest descent method. As the first guess, it is then suggested to minimize *f(x)* along one first axis, then along second etc. Using minimization along the search direction, move along the first direction to its minimum, then from there along the second direction to its minimum, and so on, cycling through the whole set of directions as many times as necessary, until the function stops decreasing (see Figure 6.1.2).
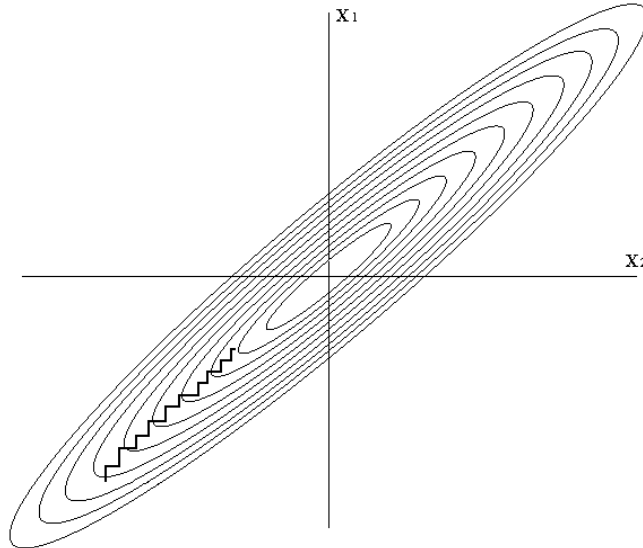
Figure 6.1.2 Converging to the local minimum using the method of orthogonal directions. The search directions are orthogonal to each other and parallel to one of the coordinate axes.

7. Method of Levenberg-Marquardt (Damped Least Squares)

In many cases, in particular in optical design, the error function is defined as a sum of squares of operand functions, which have to be minimized i.e.

$$F(\mathbf{x}) = \sum_{k=1}^{m} w_i [f_i(\mathbf{x})]^2 , \qquad (6.1.12)$$

where w_i are some weight factors.

The damped least squares algorithm makes use of this specific definition of the error function to arrive at a solution to the minimization problem. If we assume that the changes in the operand functions are linearly proportional to the changes in the variables, we can use the following equation to describe the error functions

$$\mathbf{f}(\mathbf{x} + \Delta \mathbf{x}) \approx \mathbf{f}(\mathbf{x}) - J\mathbf{f}(\mathbf{x})\Delta x , \qquad (6.1.13)$$

where $J\mathbf{f}(\mathbf{x})$ is Jacobian of $\mathbf{f}(\mathbf{x})$ and $\mathbf{f} = (f_1, f_2, ..., f_m)$

$$[J\mathbf{f}(\mathbf{x})]_{ij} = \frac{\partial f_i}{\partial x_j} \qquad (6.1.14)$$

The method uses a search direction defined by $\Delta\mathbf{x}$ that is a solution of the linear set of equations

$$(J\mathbf{f}(\mathbf{x})^T J\mathbf{f}(\mathbf{x}) + \lambda I)\Delta\mathbf{x} = -J\mathbf{f}(\mathbf{x})^T \mathbf{f}(\mathbf{x}) , \qquad (6.1.15)$$

where I is the identity matrix and λ is the non-negative damping factor, which is adjusted at each iteration [60].

Global optimization methods

The problem of local optimization is well-developed and usually can be efficiently solved, because there are a number of reliable algorithms. However the problem of the global optimization is not trivial and in the general case does not have a standard solution. Some sophisticated global search strategies are not strictly mathematical but they assume a lot of empirical decisions based on tradition, previous experience and intuition.

Global optimization methods can be divided into deterministic and stochastic methods [61],[62]. Deterministic approaches include analytic and decomposition methods that are usually problem-oriented and cannot be applied to the general case. Analytic methods can find a solution in some simple cases of constrained optimization. The decomposition methods are enumerative methods, they assume a decomposition of a large problem into smaller subproblems that can be easier solved. These methods cannot be applied when constraints are highly nonlinear and cannot be linearized. Finally, decomposition methods are computationally expensive, because they have to enumerate all possibilities of the solution.

Stochastic methods explore a multidimensional space according to some probability distributions. Depending on the dimensionality of the problem and the way of obtaining the best solution, stochastic methods may at best converge to the global minimum with probability one when time approaches infinity. When a certain solution, not necessarily the best one, must be found in finite time, stochastic methods may be better than enumerative methods because they may find a good solution with high probability.

A number of general optimization techniques have been developed that can be applied to a wide range of problems. At the same time, many specific optimization methods have been proposed for different global optimization problems. As in the case of local search we list the most known methods according to Ref. [62]. Note that the items in this list are not necessarily mutually exclusive.

I. Exact approaches

1.   Simple Strategies

This group includes the most well-known sequential or passive (simultaneous) methods of global optimization, for instance, uniform grid search, space covering sampling and even pure random search. These methods are universal, but they can be used only for simple problems, because they are extremely ineffective in the case of high-dimensional problems.

2.   Complete (Enumerative) Search Methods

These approaches are based on a complete enumeration of the possible solutions and can be mostly applied to combinatorial problems, or to some structured problems.

3.   Successive Approximation or Relaxation Techniques

Here the original optimization problem is replaced by several more relaxed subproblems which have a simpler solution. Successive improvement of subproblems to approximate initial problem, for instance by cutting planes, diverse minorant constructions, nested optimization, decomposition strategies etc.

4.   Homotopic and Trajectory Approaches

These methods have the aim to sequentially visit (enumerate) in certain way the stationary points of the error function obtaining possible solutions. This group includes path-following search strategies, fixed point methods, pivoting algorithms, differential equation model based, etc. One of these strategies applied to the optical system design has been developed as a part of this thesis and is discussed in Chapters 7 and 8.

5.   Adaptive Stochastic Algorithms

This is spacious class of approaches, based upon random sampling in the multidimensional space. Basically, it includes various random search strategies that are convergent upgraded with parameter adjustment, clustering and deterministic solution refinement, statistical stopping rules, etc.

6.   Bayesian (Partition) Methods

These methods are based upon some a priori information, which enables a stochastic description of the function-class modelled. After each optimization step, the problem-instance characteristics are adaptively estimated and updated.

7.   Branch and Bound Strategies

These methods have been developed for an exact solution of the global optimization problem. They assume adaptive partition, sampling, and subsequent bounding procedures. These procedures are iteratively applied to the collection of solutions, bounding good 'candidates' remaining within the solution space. Branch and bound methods integrate many specific approaches and may be implemented in many cases. These are methods typically based on a priori knowledge about the problem, e.g. how rapidly each function varies or whether an analytic formulation of all functions is available.

II Heuristic approaches

1.   'Globalized' Extensions of Local Search Methods

In this case the preliminary estimation of the good solution is performed on the base of the experience, analogies or intuition and then the local search is used. These are partially heuristic algorithms, often successful in practice. The starting points for the local optimization are placed in 'promising' domains and even this task should be done in the clever way, in order to allow convergence to different solutions. Very often, sophisticated algorithm enhancements are applied to the basic optimization strategy (see section 6.3 for example).

2.   Genetic Algorithms, Evolution Strategies

These approaches heuristically resemble biological evolution (the 'survival of the fittest' idea and the process of natural selection). They use an adaptive search procedure based on a 'population' of candidate solution points. Each optimization cycle includes a competitive selection that drops the worst solutions. The promising competitors having 'good health' recombine with each other. Also a 'mutation' strategy is used by introducing a small random change to a single component of a candidate. The recombination and mutation modifications are applied successively, to generate new solutions exploring new good regions in the multidimensional space. Different approaches, based on these evolution idea, can be constructed.

3.   Tabu Search

The basic idea of this method is to prevent the optimization to move to points already visited in the search space, at least for the upcoming several steps. This enforces optimization to move far away from the starting point. In tabu search, the optimization can temporarily neglect some constraints or accept new conflicting solutions, to avoid

paths already investigated. This approach leads to exploring new regions of search space.

4.   Approximate Convex Global Underestimation

This strategy attempts to estimate the global convexity characteristics of the error function based on directed sampling in search space.

5.   Sequential Improvement of Local Optima

These strategies usually operate on adaptively constructed auxiliary functions, to assist the search for gradually better optima. This general heuristic principle includes tunneling, deflation, and filled function approaches (see section 6.3 for example).

6.   Simulated Annealing

These methods are based upon the analogy of crystal structure which being cooled spontaneously attempts to become in stable equilibrium configuration (local minimum of potential energy). Mathematically simulated annealing is a generalization of a Monte Carlo method. The approach is based on the manner in which liquid freezes or metal crystallizes during process called annealing. In this process a liquid media, initially at high temperature and disordered, is gradually cooled in the way that the system at any time is near thermodynamic equilibrium. In the cooling process, the media becomes more ordered and finally approaches a "frozen" ground state at zero temperature. However if the melting temperature of the system is not high enough or cooling is performed insufficiently carefully the system may have forming defects or freezing out in metastable states (bad local minima).

The major difficulty in implementation of this method is that there is no always obvious analogy for the temperature T with respect to a free parameter in the certain optimization problem.

7.   Continuation Methods

These techniques replace the original error function with a rougher but smoother function which then has less local minima, and then use a local minimization procedure to get in the vicinity of the global solution (see section Escape function in section 6.3).

6.2.   Optimization in optics. Specifics.

In our days the optical system designer uses highly sophisticated software tools [5]. The personal computer on your desktop is able to trace several million ray-surface intersections per second. However, growing computation speed does not affect proportionally the development time, because the most important part of the design is creative approach. This observation remains true also for other optimization applications.

Nowadays the design of an optical system often starts with the search of similar existing designs because thousands of designs have been created and can be found in the patent literature and lens databases. Alternatively, the designer can start with a rough sketch of an optical system and then the optical software optimizes that sketch to the specific design goal. However, in any case, a good optimization routine is the kernel of modern optical program. The choice of the starting point is extremely important because it defines whether a successful solution can be obtained in certain period of time. This choice is based upon the designer's experience and his insight into the purpose of the optical system.

Most often an optical system, as an object of design, has to satisfy certain specifications (field of view, aperture, wavelength range etc) and must possess the necessary image quality. The optimization merit function in this case is a sum of

weighted values of geometrical or wavefront aberrations by analogy with (6.1.12) [5],[31],[63],[64]. In order to define an error function it is also possible to use the squared differences between current and desired MTF values at certain spatial frequencies. However the MTF optimization converges much slowly and may be used only on the last optimization stage. Another example of the MF construction in optical design is in the optimization of the multilayer coating structure where the minimum (or sometimes the maximum) of the reflectance must be achieved [63].

Generally the optimization of optical systems can be classified as a mixed-integer problem. Usually the parameters of this optimization are the positions of the components in optical system, the optical features of these components that are defined via surface parameters (curvatures, aspheric coefficients etc) and the characteristics of refractive media (refraction indices and dispersion). Most of the variables are continuous, but some of them (e.g. refractive indices and binary coefficients) can be discrete. Normally a number of geometrical constraints and required paraxial characteristics (focal length, magnification, pupil positions, image distance etc) are also introduced. It often happens that the global minimum obtained with global optimization is not acceptable because it may be very sensitive to the tolerances and cannot be produced for affordable price. In this case some compromise between the required image quality and the manufacturability of the optical device should be found.

Most optical design programs use different modifications of the DSL algorithm for local optimization [5],[63],[64]. These methods are very well developed and mostly reliable. Some of global search methods discussed above can be applied to the optimization of optical systems [65]-[70]. However, optical system design software such as Code V® or Zemax® use their own global optimization routines which are usually kept secret. One exception from these (commercially justified) "hidden" approaches is the Global Explorer, an escape function approach, which is implemented into OSLO® optical software [71]. This approach is discussed in more details in section 6.3. The most reliable results in the global optimization of optical systems are obtained with Global Synthesis which is a proprietary global optimization algorithm implemented in Code V [31]. Although little is known about the type of algorithm, it is used by many lens designers and it has proven to be a very powerful global optimization algorithm capable of generating multiple local minima and hopefully also the global minimum.

Optimization of lithographic systems

The issue of optimization of the lithographic objectives is probably the most difficult in optical system optimization. Usually a modern DUV lithographic objective has more than twenty components having aspheric surfaces. That results in more than one hundred optimization variables. The most important constraints are the magnification, total track and telecentricity. The degree of the aberration correction is defined by the resolution limit required by ITRS. For lithographic objectives the strict respect of the orthoscopic condition, i.e. the rigorous observation of dimensional proportions, is required as well. That means that the distortion should be strictly corrected for the whole field [9],[10].

The optical systems for extreme UV lithography have only several components (mirrors) which, all of them, are high-order aspheres. However the NA value and the field size are much smaller, so the aberration balance is different. In the optimization of EUV projection objectives the additional difficulties are related with the occurrence of obscuration [72].

6.3.   Local optimization strategies to escape from poor local minima

The presence of multiple local minima during optimization is one of the major challenges of optical system design. Achievements in global optimization give the optical designer a very powerful tool to escape from poor local minima. These methods tend however to be very time-consuming and therefore designers often attempt to improve solutions converging to unsuccessful local minima by using local optimization strategies. Here we describe three very useful strategies that can be used for local optimization.

Modifying the merit function

One of the empirical strategies to "tunnel" out of bad local minima (or to escape from stagnation) is to modify the conditions under which local optimization algorithms operate. This can be achieved by changing, for instance, the system parameters, some parameters of the local optimization algorithm, or the merit function.

Many computer programs allow an easy switch between MFs based on transverse and wavefront aberrations. Although occasionally successful, this strategy is limited by the fact that when system parameters change the behavior of these two merit functions is often very similar. The experience shows that the chances of success increase when the "old" and "new" MFs both tend to zero for ideal systems but differ sufficiently from another.

A new type of merit function that may be a useful switch partner for the standard merit functions in intermediate stages of optimization can be defined as follows: Consider an arbitrary ray ($A'I'$ in Figure 6.3.1) that has in the image space the direction cosines L and M with respect to the x and y axes, respectively. The two components of the transverse aberration of the ray (defined with respect to the chief ray) are denoted by δx and δy. The ray intersects in I' the image plane and in A' a sphere centered in the intersection point I of the chief ray with the image plane. The radius R of the sphere should be chosen larger, but still of the same order of magnitude as the length II' of the transverse aberration vector. The length R' of the segment $A'I'$ is then given by

$$R'/R = a + \sqrt{1-b} = a + 1 - b/2 - b^2/8..., \qquad (6.3.1)$$

where we have used the abbreviations

$$a = \left(L\delta x + M\delta y\right)/R \qquad (6.3.2)$$

and

$$b = \left[\left(\delta x^2 + \delta y^2\right) - \left(L\delta x + M\delta y\right)^2\right]/R^2. \qquad (6.3.3)$$

Since for ideal imaging R' tends to R, the quantity $R'/R - 1$, averaged over all rays for a given field point, can be used as an intermediate stage merit function (the "radius" MF). The power series expression should be used instead of the exact expression in order to avoid abnormal termination when for certain rays that have large aberrations b becomes larger than 1.

In order to test it we implemented the "radius" MF as a user defined merit function in CODE V. Figure 6.3.2 shows the evolution of the "radius" MF as well as the root mean square (RMS) spot size and RMS wavefront during an optimization driven by the "radius" MF. It can be observed that, while the "radius" always decreases, the other two MFs actually increase beyond point A. Moreover, the RMS spot size and RMS wavefront appear to be strongly correlated i.e. they increase or decrease at the same time. In many other tests we have found that the behavior of the transverse aberration along trajectories in the parameter space is much stronger correlated with

that of the wavefront that with that of the "radius". Therefore, the "radius" may be a more successful switch partner for the RMS spot size than the RMS wavefront.
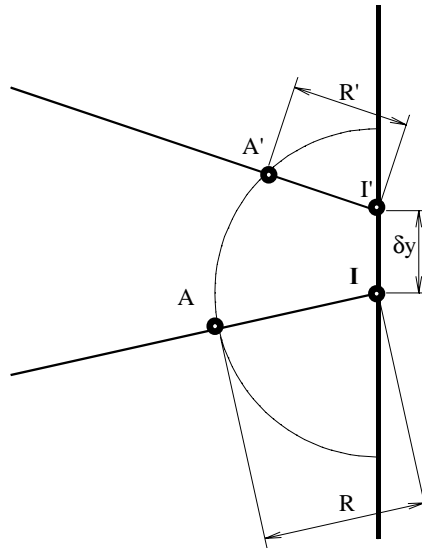
Figure 6.3.1 The definition of the "radius" merit function
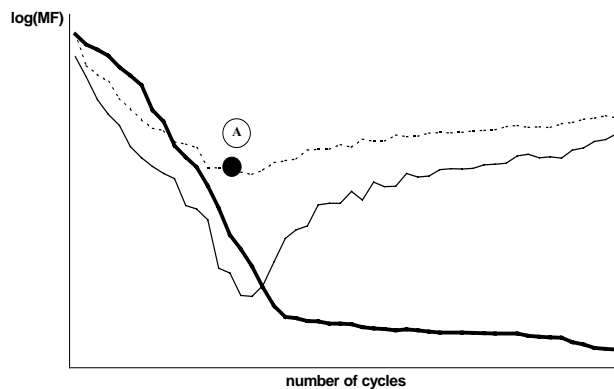
Figure 6.3.2 The evolution during optimization of the merit functions based on the "radius" (thick line), transverse aberration (thin line) and wavefront aberration (dashed).

In fact, switching back and forth between the RMS spot size and the "radius" MFs can sometimes lead to the much better solution even when we start from very unsuccessful initial configuration. For instance, a configuration very close to the well-known Double Gauss objective was obtained by starting from plane-parallel plates (that have a solve on the last surface to keep the required focal length).

Escape function

The basic idea of this approach is to upgrade the initial error function with an escape function in order to prevent the convergence to unsuccessful local minimum [73]. This escape function can be defined as

$$f_{esc}(\mathbf{x}) = \sqrt{H} \exp\left(-\frac{1}{2W^2} \sum_1^N w_i (x_i - x_{LMi})^2 \right), \qquad (6.3.4)$$

where x_{LMi} is the position of the local minimum from which the design is to escape, w_i are weights for design parameters, H and W are height and width of the escape function as shown in figure in Figure 6.3.3.

For a successful escape, the escape parameters H and W have to be determined. However, the choice for these parameters is difficult and they are found by trial and error since the size and shape of the regions of attraction are unknown.
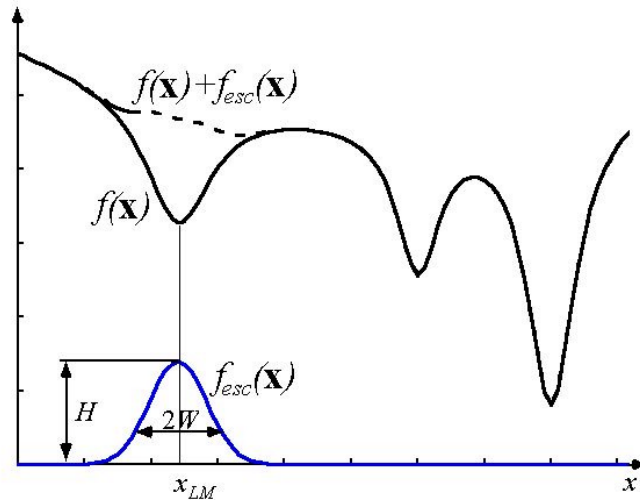
Figure 6.3.3 Usage of an escape function to find a new local minimum. The local optimization converges towards a certain local minimum. To escape from the region of attraction of this minimum, an escape function is added to the error function. The old local minimum then disappears and the local optimization can now escape towards in a minimum.

This algorithm is not as deterministic as it might appear at first sight. The first step of the local optimization starts at the position of the old local minimum. In this point, the gradient of the escape function is also zero (the old minimum is now a local maximum) and all directions are now downward directions. Hence, the direction of the first step will be unpredictable. At the same time constraints can be well satisfied as the algorithm makes use of local optimization.

Over-designing

A different potentially useful strategy to escape from poor local minima is to temporarily over-design the system. The essence of this approach is to make available for optimization more system parameters than a designer may use for the given aperture and field specifications. For instance, it is possible to temporarily relax some requirements for system specifications or change the balance of components of the MF by changing weights of their contributions.

A simple example of this idea is shown in Figure 6.3.4, where the Cooke Triplet is obtained by starting from plane-parallel plates. Using the default Code V RMS spot size and starting in point O (plane parallel plates with a solve on the last curvature to keep the desired focal length) the solution reaches the local minimum A, but the MF in this point is still high. In this point the MF is modified by reducing the off-axis field weights to values close to zero. Thus, between the points A and C the optimization uses all variables only to correct on-axis aberrations of different orders (over-designing). Because off-axis aberrations are (almost) neglected by the optimization algorithm, the transverse aberration in point B becomes very large. Despite this fact, when in point C the MF is switched back to default, the system easily reaches the standard Cooke Triplet shape (D) where the imaging quality is considerably better than in point A. Note, that along the entire trajectory the standard merit functions based on transverse and wavefront aberrations are strongly correlated.
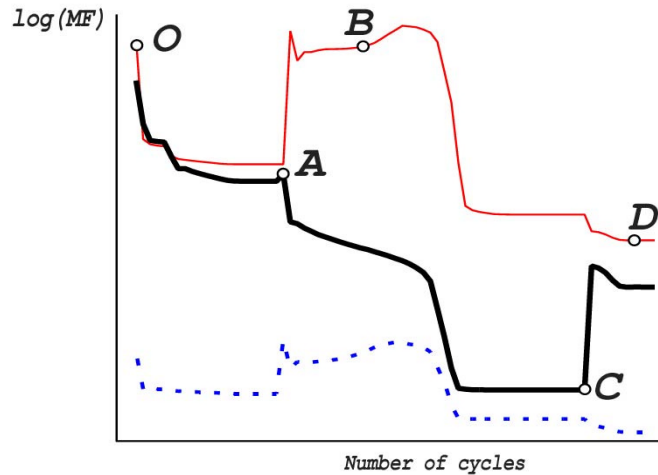
Figure 6.3.4 Evolution of the standard merit functions based on transverse aberrations (thin line) and wavefront aberrations (dashed) as well as the evolution of a merit function with very small off-axis field weights (thick line), in the process of obtaining the Cooke Triplet. Between *O* and *A* and between *C* and *D* the driving merit function is the standard transverse aberration. Between *A* and *C* the driving merit function is the one with reduced field weights.

This strategy turns out to work well also for poor local minima of more complex systems. In more general situations, if the system should have only spherical surfaces, a similar over-designing effect is sometimes achieved by temporarily making the surfaces aspheric, including the aspheric coefficients in the optimization, and then reducing them gradually back to zero. The temporary increase of the dimensionality of the variable space often creates new opportunities for descent directions at the location of the poor local minimum.

6.4.   Conclusions

It this chapter we discussed the general optimization issue and its peculiarities applying to the optical system design. A number of local and global optimization approaches were discussed. The Damped Least Square algorithm is usually credited as the most efficient local optimization algorithm in optics. However, the principle of the most reliable global optimization engine among those presently in use in optics is unknown. Thus it is necessary to provide the optical community with more insight into this problem.

Finally, three optimization strategies based on the local optimization in order to escape from a local minimum are discussed. The first strategy is to radically modify the error function. The old and new error function should both tend to zero for ideal systems but must differ sufficiently from another. The second strategy assumes an upgrade of the MF in order to get out from the undesired local minimum. The third strategy is to temporarily over-design the system, i. e. to make available for optimization more system parameters than a designer would normally use for the given aperture and field specifications.

We have also observed that, when switching between the merit functions, within a certain range on the trajectory, this switching is much more successful than in others. This leads us to the idea that there are points in the MF landscape which, if slightly perturbed, may converge to the different local minima. This fact will be investigated further in the next chapter.

7. Optimization via saddle points

7.1.   Topography of the MF space

A characteristic feature of present-day global optimization methods is that they find local minima only as isolated points in the parameter space of the system, with no information about the MF topography around the separate local minima or in the space between them. The strategies presented in Chapter 6 suffer from the drawback that their success depends to a large extend on serendipity. It is very hard to predict when they will work and when not. Therefore, in this chapter we will discuss a very different strategy, that also offers a deep insight into the peculiarities of the specific design case. We will show that, with some enhancement of the local optimization algorithm, it is possible to move from one local minimum to a neighboring one by locating a saddle point between them. An important issue to be examined is the following: if we are in the vicinity of a given local minimum (in its basin of attraction) can we somehow feel the presence of a neighboring local minimum?

Let us first start with a simple mountain-landscape analogy. A tourist wants to walk from one valley of the landscape to a neighboring one, and spend the least amount of effort in his travel. The optimal path would then be one that passes through a mountain pass. A mountain pass is in fact an intuitive example of a saddle point. Returning to optimization, the strategy we propose is the following: for finding a neighboring local minimum we find first a saddle point that leads to it. It is very difficult to find some order in the topography of nonlinear merit function. In our view the saddle points are the necessary element for understanding the MF structure. In this chapter we show that, when certain quite general conditions are satisfied, the MF landscape has a remarkable property, which we could not find mentioned in earlier literature. The local minima then form a network in which all nodes are connected via links that contain a special type of saddle point. On the other hand, it is known for several decades that a way to find a new local minimum is to identify a saddle point on the boundary of its region of attraction [74],[75].

Figure 7.1.1 shows a two-dimensional saddle point. As for local minima the gradient of the merit function vanishes at the saddle point. However, while in one direction the saddle point is a minimum, in the other direction it is a maximum.

a)   b)
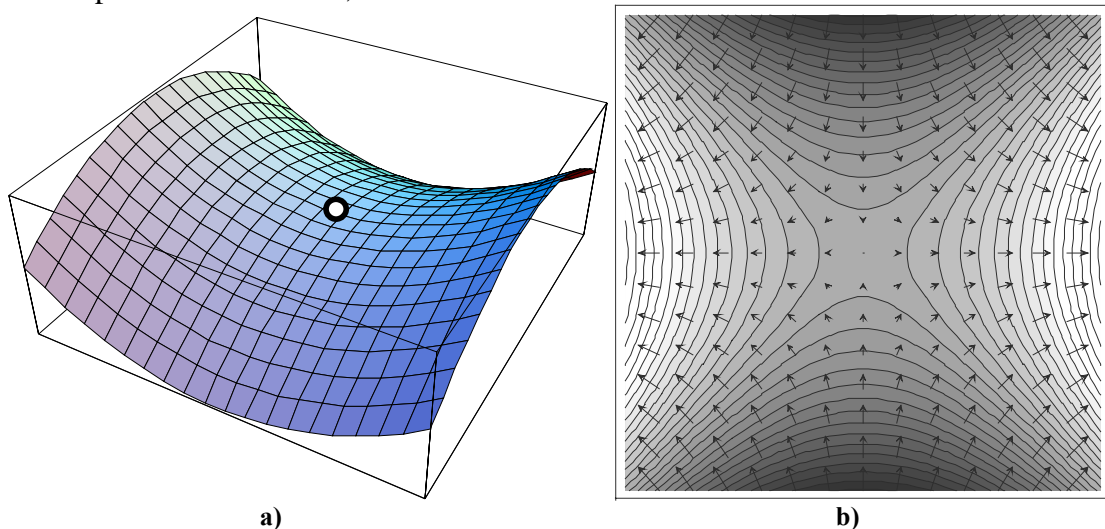
Figure 7.1.1 a) Saddle point in a two-dimensional solution space. At the saddle point, the merit function has a minimum in one direction and a maximum in the direction perpendicular to the first one. b) The equimagnitude contour plot together with the gradient plot.

7.2.   Saddle points: Morse index

In our discussion we consider for simplicity a global optimization problem with continuous variables, having no constraints or only equality constraints, and assume a MF of the form

$$f(\mathbf{x}) = \sqrt{\frac{\sum w_i \left(a_i(\mathbf{x}) - \tilde{a}_i \right)^2}{\sum w_i}} \,, \tag{7.2.1}$$

where a_i are image defects computed with ray tracing, w_i the corresponding weights and the tilde denotes the target values for the corresponding a_i. A point in the solution space is described by the vector $\mathbf{x} = (x_1, x_2,..., x_N)$ whose components are the N optimization variables. The critical points in the N-dimensional solution space are those points for which the gradient of f vanishes

$$\nabla f(\mathbf{x}) = \left(\frac{\partial f}{\partial x_1}, \frac{\partial f}{\partial x_2}, ..., \frac{\partial f}{\partial x_N} \right) = 0 \,. \tag{7.2.2}$$

In this section we will focus on the behavior of the equimagnitude surfaces of f, which are N-1 dimensional hypersurfaces in the solution space along which f is constant. In a small neighborhood around a critical point, the equimagnitude surfaces are given by

$$\sum [Hf(\mathbf{x})]_{ij} \hat{x}_i \hat{x}_j = const \,, \tag{7.2.3}$$

where the circumflex denotes the values of the optimization variables in a translated coordinate system that has its origin at the critical point, and where $Hf(\mathbf{x})$ is the Hessian matrix of $f(\mathbf{x})$ defined according (6.1.7).

As known from linear algebra, the coordinate system can be rotated in such a way that the quadratic form on the left-hand side of Eq. (7.2.3) contains only squares of the variables (denoted below by a bar) in the new coordinate system. The equimagnitude surfaces around the critical point now become

$$\sum \lambda_i \bar{x}_i^2 = const \,. \tag{7.2.4}$$
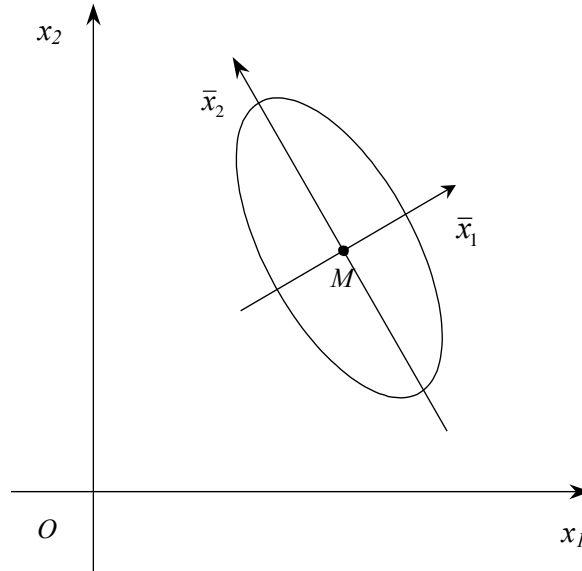
Figure 7.2.1 In a small neighborhood around a local minimum or maximum, the equimagnitude surfaces are ellipsoids having their axes oriented along the eigenvectors of the matrix A.

The axes of the new coordinate system are then oriented along the eigenvectors of $Hf(\mathbf{x})$, and the factors λ_i in Eq. (7.2.4) are the corresponding eigenvalues. Thus, as shown in Figure 7.2.1, in the case of local minima or local maxima the equimagnitude

surfaces around these points are ellipsoids with axes oriented along the eigenvectors. The way to perform the rotation of the coordinate system will be discussed in more detail in this chapter.

An important characteristic of critical points for which the Hessian of f has a nonzero determinant is the number of negative eigenvalues of the Hessian (the so-called Morse, or Hessian, index) [76]. A negative eigenvalue means that along the direction defined by the corresponding eigenvector of the Hessian the critical point is a maximum. Thus, local minima have Morse index 0 (all eigenvalues are positive), maxima have Morse index N (all direction are downward), and for saddle points the Morse index has values between 1 and $N-1$. Equimagnitude surfaces around a saddle point with MI=1 consist of one surface for MF values higher than that of the saddle point while they consist of two separated surfaces for equimagnitude values lower than that of the saddle point (see Figure 7.2.2). Note that equimagnitude surfaces having some value $f=f_0$ of the MF encircle regions in the solution space for which $f<f_0$. If for instance f_0 is the MF of a local minimum then the equimagnitude surface (or the part of it situated near the minimum) reduces to one point, the minimum itself. For slightly larger values of f_0 (a part of) the equimagnitude surface encircles a small ellipsoidal region around the local minimum. If the value of f_0 continues to increase then the encircled volume also increases.

a)   b)   c)
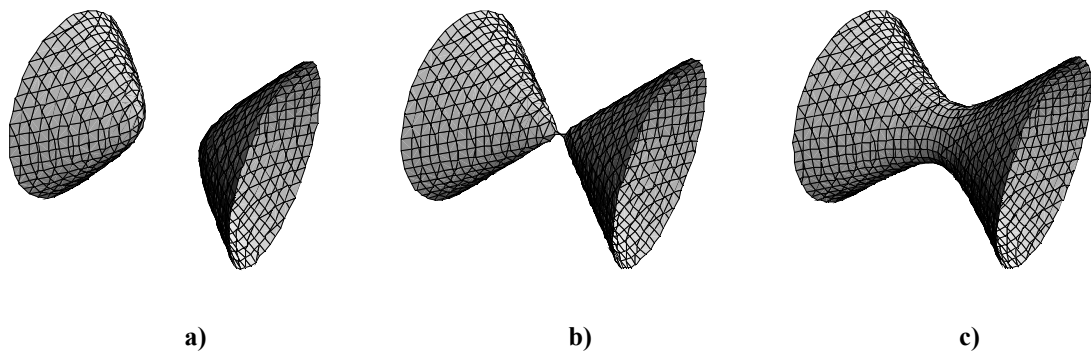
Figure 7.2.2 Typical behavior around a saddle point having a Morse index of one. The merit function value at the saddle point is f_{sp}. a) for $f<f_{sp}$, we have two surfaces. b) for $f=f_{sp}$ the two surfaces only touch at the saddle point and encircle the surfaces drawn in a). c) for $f>f_{sp}$ one surface encircles the saddle point and all other surfaces with smaller equimagnitude values.

As will be shown below, if we are interested in the detection of local minima, the saddle points with a Morse index of one (SPMI1) play a special role. For the present discussion it is sufficient to keep in mind that a SPMI1 is a maximum in one direction (the downward direction), and a minimum in a $N-1$ -dimensional hyperplane orthogonal to that direction. If, for instance, $N = 2$, then every saddle point is a SPMI1. Intuitively, in the case of many dimensions, the downward directions of a SPMI1 are similar to the downward direction of a two-dimensional saddle point, and each of the $N-1$ upward directions is similar to the upward direction of a two-dimensional saddle point.

Figure 7.1.1 b) and the enlarged detail of Figure 7.2.3 show the contour plot of the merit function in the neighborhood of a two-dimensional saddle point. Close to the saddle point, the equimagnitude contours are hyperbolas, whereas for the value of the MF corresponding to the saddle point itself the equimagnitude contours degenerate into a pair of straight lines (the asymptotes of the hyperbolas).
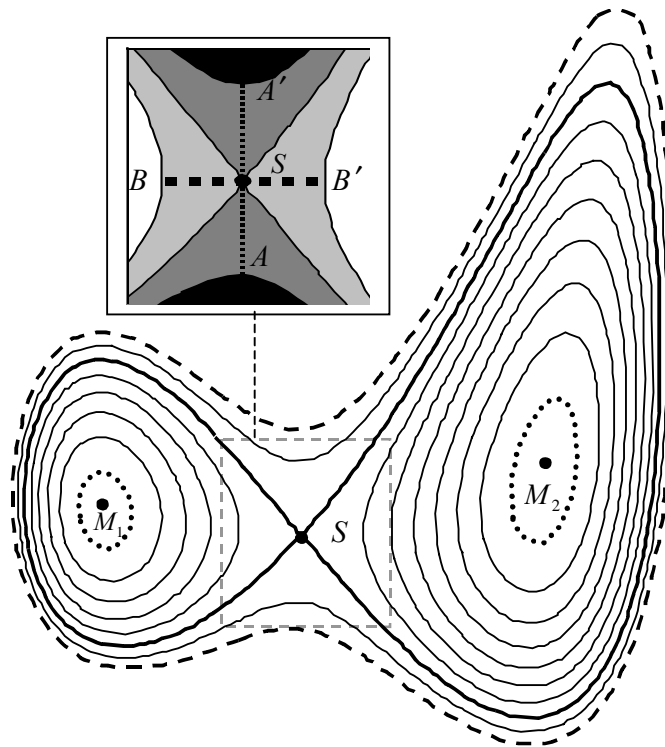
Figure 7.2.3 Two local minima and a saddle point. In the enlarged detail, light gray indicates lower and dark gray indicates higher values of the merit function (obtained by two-dimensional cut through the 5-dimensional merit function landscape of a Cooke triplet).

7.3.   Networks of local minima

We will now show in an intuitive way that the local minima within an arbitrary equimagnitude surface form a connected network, i.e. that there is a well-defined path from any local minimum to any other local minimum in the solution space. Consider first the situation shown in Figure 7.2.3, two local minima in an *N*-dimensional solution space. We assume the existence of a surface with $f_0 = f_a$ that encircles both minima (the thick dashed curve). Then, for a sufficiently small value $f_0 = f_b < f_a$ (for instance for f_b slightly larger than the largest of the two MF values corresponding to the local minima) the equimagnitude surface consists of two separate parts (the thick dotted curves), whereas for $f_0 = f_a$ we have only one encircling surface (thick dashed). Assuming that the MF landscape is free of pathologies, for some value f_S with $f_b < f_S < f_a$ we will encounter the limiting case when the two separate parts of the encircling surface will touch each other in one point *S*. We now show that the split point *S* is in fact a saddle point with *MI=1*. If we consider a value of the MF $f_B = f_{B'}$ slightly lower than f_S, the corresponding equimagnitude surface will be split. Let then *B* and *B'* be the two points on the separate parts of the equimagnitude surface for which the length of the segment *BB'* is minimal. (See enlarged detail in Figure 7.2.3.) Obviously, along the line *BB'* the split point *S* is a maximum. We now consider an equimagnitude surface with a MF $f_A = f_{A'}$ slightly larger than f_S. Since this equimagnitude surface encircles the one with $f_0 = f_S$, any line perpendicular to *BB'* and passing through *S* will intersect it in two points, denoted by *A* and *A'* in Figure 7.2.3. Along *AA'* the point S is then a minimum. Since this is valid for any choice of the line *AA'* in a *N-1* dimensional hyperplane orthogonal to *BB'*, *S* is a minimum in *N-1* directions, and is thus a saddle point with *MI=1*. If we now choose the points *B* and *B'* as starting points, local optimization will generate two paths in the solution

space that will lead to the two minima. Together with the saddle point, these two paths form the link between the two local minima.

Assume now that we have an equimagnitude surface with some (large) value of $f_0 = f_a$ that encircles an arbitrary number p of local minima. (In Figure 7.3.1. where $p=3$, this is the outermost contour.) If we decrease f_0, at some value $f_{S1} < f_a$ the encircling surface will split into two surfaces that will now encircle p_1 and $p-p_1$ local minima, respectively. (In Figure 7.3.1. we have $p_1=1$.) Using the same reasoning as above, it can be seen that the point S_1 in Figure 7.3.1 is also a saddle point with $MI=1$. By starting local optimizations at a pair of points obtained be slightly perturbing the saddle point on both sides along the eigenvector with negative eigenvalue, we obtain a link between one local minimum in the group of p_1 encircled local minima, and one in the group of $p-p_1$ local minima. By further decreasing f_0, we obtain successive splits of the encircling surfaces. Each such split generates an additional link between two local minima situated in the two different groups resulting from the split. When f_0 has reached a value that is lower than the MF of the lowest $MI=1$ saddle point (S_2 in Figure 7.3.1) all local minima encircled by the equimagnitude surface with $f_0 = f_a$ are linked together in a network via links that contain each a $MI=1$ saddle point.
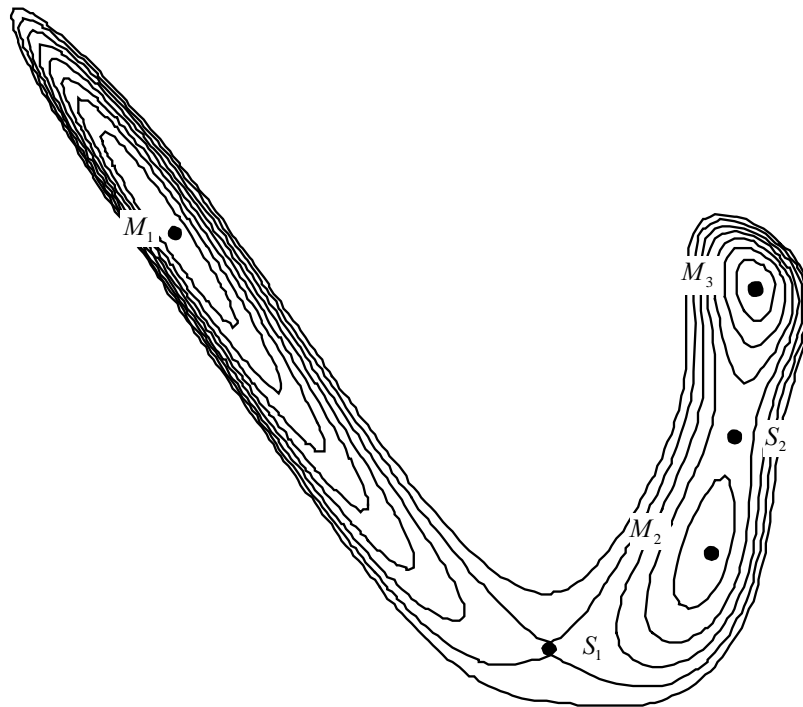
Figure 7.3.1 Several local minima and the saddle points between them (obtained by two-dimensional cut through the 5-dimensional merit function landscape of a Cooke triplet).

We have thus shown that the local minima encircled by an arbitrary equimagnitude surface (without critical point on it) form a connected network In some special situations, it may be useful to modify this statement. If we have for instance a positive MF that decreases to zero when any variable (or linear combination of them) tends to infinity, then, in addition to the "usual" local minima we also have a continuum of minima at infinity. For practical purposes we may be interested in a network in which the links between "usual" local minima do not pass through infinity. Such a network is formed for instance when a pair of equimagnitude surfaces exists such that both surfaces encircle the "usual" local minima, and when the surface having the larger value of the MF also encircles the other one.

For our purposes, it is important to know whether in typical situations occurring during optical system optimization we can always find such equimagnitude surfaces that encircle all (useful) local minima. At the time of printing this thesis, we have examined only a limited number of situations and further research is certainly necessary. However, our results, presented in the next chapter, make us believe that either this desirable property of the landscape of the MF (7.2.1) is satisfied automatically, or that it can be achieved by modifying the optimization problem adequately (e.g. by using inequality constraints). It is well known to optical designers that outside some useful regions in the solution space the optical system configurations tend to suffer from ray failure because some rays either miss surfaces or suffer from total internal reflection. Close to ray-failure situations, the incidence angles of those rays at the critical surfaces are large, therefore the aberrations and the MF (7.2.1) of the given optical system configuration tend to be large. Therefore, close to the ray failure borders we can expect in the solution space equimagnitude surfaces having a large value of the MF. The local minima encircled by these surfaces form then a network. The possibility of enforcing the desirable properties of the MF landscape when these properties are not automatically satisfied should be further researched.

It is important to note that this linking network is independent of the exact shape of the equimagnitude surfaces and the dimensionality of the MF space. From a topological point of view, two surfaces are considered equivalent if there exists a continuous deformation that transforms one surface into the other one. Therefore, the network of minima represents changes in the topology of the MF landscape. However, we only consider topological changes for which the equimagnitude surfaces are split for decreasing MF values (saddle points with MI=1) and topological changes for which equimagnitude surfaces vanish (local minima). Other topological changes, which might be of interest for other purposes, occur at critical points having a Morse index higher than 1.

7.4.   Locating saddle point: simple example

In order to illustrate a simple method for locating saddle points, let us first examine the equimagnitude contours of the two-dimensional function shown in Figure 7.4.1. This function has three local minima, A, B and C. It was already shown that in a very small neighborhood of a local minimum the equimagnitude contours are always ellipsoids. We can take one of them, as a reference, and call this ellipse the "reference ellipse" for the given minimum. If some scale parameter is used (e.g. one of the half-axes) it is possible to rescale the reference ellipse to any desired size, by keeping its shape unchanged. The dashed lines in Figure 7.4.1 show the reference ellipse of the minimum A, rescaled to four different sizes.

Let us now compare the shapes of the real equimagnitude contours with those of the reference ellipses. The point S in Figure 7.4.1 is a saddle point. We observe that far away from saddle points the shapes of the equimagnitude contours are close to those of the ellipses. Close to the saddle point however, the shapes of the equimagnitude contours deviate strongly from the ellipses. Our working assumption is that the deviation of the shape of an equimagnitude contour from the reference ellipse is maximal in the direction of a saddle point. A closer inspection of Figure 7.4.1 reveals that there where this deviation of shape is maximal, the MF along the reference ellipse has a minimum. Therefore, the simple method to sense the direction of a saddle point would be to compute the minimum of the MF along rescaled reference ellipses. This

means basically to do local optimization by imposing the reference ellipse as an equality constraint.

If we are in the local minimum *A* and compute the MF along the smallest dashed ellipse in Figure 7.4.1 we obtain the results shown in Figure 7.4.2. Since we are on an ellipse, for each value of one Cartesian coordinate (e.g. *x*) we obtain two different values of the other coordinate (*y*) and therefore two values for the merit function. The two MF curves form together the closed curve shown in Figure 7.4.2. Note that we have a minimum of the MF in the right part of the lower curve. The pair of coordinates that corresponds to this local minimum is plotted in Figure 7.4.3 as the right large dot. We observe that this dot points, as expected, in the direction of point *B*.
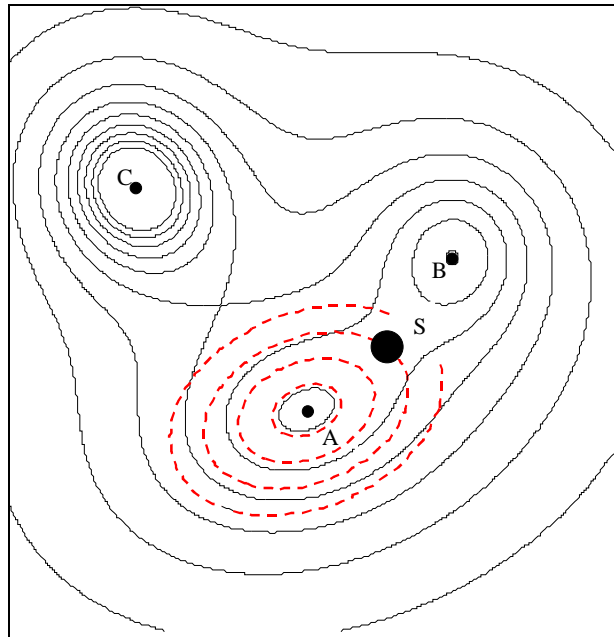
Figure 7.4.1 The deviation of the shape of the equimagnitude contours (continuous lines) from (properly rescaled) reference ellipses (dashed lines) is maximal in the direction of saddle points (*S*).

It is sometimes possible to find several local minima around reference ellipses, which then point towards different saddle points. For instance, by slightly increasing the size of the reference ellipse around point *A* in Figure 7.4.3, it becomes possible to sense the presence of point *C* (left large dot). Similarly, when we started in the local minima *B* and *C* and optimized around (sufficiently large) reference ellipses we could sense the presence of the two other minima, while still being in the basin of attraction of the start minimum.
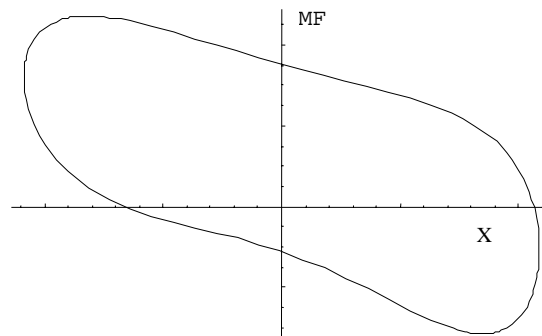
Figure 7.4.2 The two merit function curves corresponding to the upper and lower half ellipse form together a closed curve.

Once the direction of the saddle point has been determined, the saddle point itself can easily be found. Figure 7.4.4 a) shows a two-dimensional landscape of the default CODE V MF (which is based on the transverse aberration). The local minimum M_1 corresponds to the triplet shown in Figure 7.4.5 a). The optimization variables are the curvatures of the 3rd and 5th surfaces.
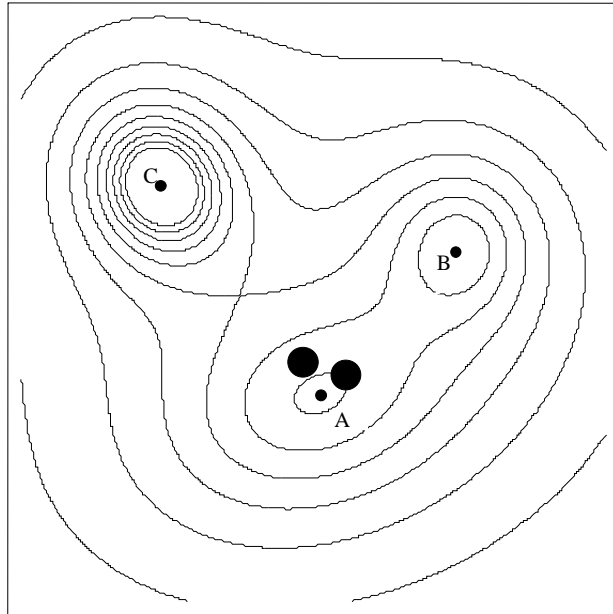
Figure 7.4.3 Sensing the directions of the saddle points that lead to the local minima *B* and *C* from the neighborhood of the local minimum *A*.

a)	b)
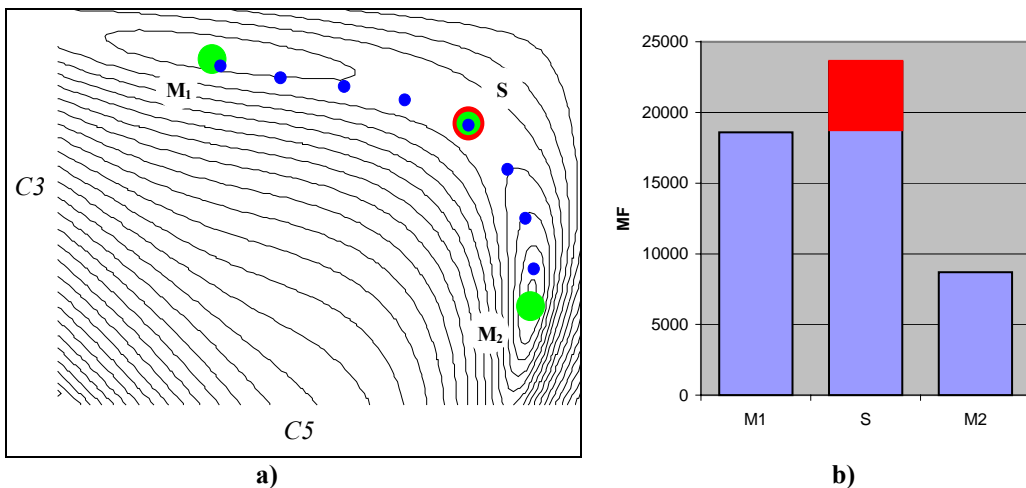
Figure 7.4.4. a) Two-dimensional merit function landscape for a triplet, with two local minima *M₁* and *M₂* and the saddle point *S* between them. The two variables are the curvatures of the 3rd and 5th surfaces. b) Bar chart indicating the values of the merit function for *M₁* , *M₂* and *S*.

We determine first the direction of the saddle point as discussed previously (the small dot closest to M_1). Then we track this minimum by gradually increasing the size of the reference ellipse and reoptimizing after each step (the succession of small dots between M_1 and S). At each step (small dot) we compare the value of the minimal MF with the minimal MF at the previous step. As long as the minimal MF increases from one step to another, we keep increasing the ellipse. When the MF starts to decrease, we have passed the saddle point. Then we are already in the basin of attraction of the

new local minimum and if we remove the ellipse constraint and optimize as usual we obtain the new local minimum M_2, which in this case is the well-known Cooke Triplet (Figure 7.4.5 c)). The system corresponding to the saddle point S is shown in Figure 7.4.5 b).

In the bar chart shown in Figure 7.4.4 b) the bars represent the default CODE V merit function for the starting local minimum, the saddle point and the final Cooke Triplet. The difference between the heights of the first two bars (shown in dark) indicates the height of the MF barrier that must be tunneled.

This basic strategy can be generalized and extended to a multidimensional parameter space as is discussed in the next section.

| a | b | c |
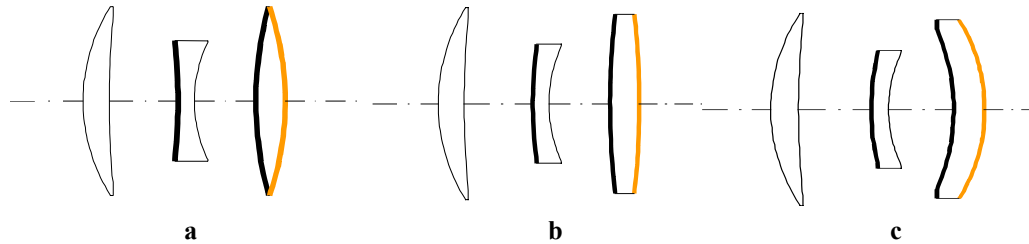
Figure 7.4.5 The triplets corresponding in Figure 7.4.4a) to the points M_1 (a), S (b) and M_2 (c). The 3rd and 5th surfaces, whose curvatures are the optimization variables, are shown with thick black lines. The 6th surface, which is controlled by a solve, also changes and is shown with a thick gray line.

7.5.   General algorithm for detection of the saddle points

A first practical utility of the discussed network structure is for global optimization. This generally very difficult task can now be divided in three separate steps (see Figure 7.5.1):

1. For a given local minimum, detect the *MI=1* saddle points that connect it with the neighboring local minima,

2. Starting from some arbitrary local minimum, find the rest of the network

3. When the network is known, select the best solution(s) or identify entire branches along which the imaging performances of the nodes are satisfactory.

This procedure for global optimization is essentially different from other global optimization strategies as the search for the global minimum is now split in two distinct stages: a local minimization from saddle points and a local saddle point search from minima (i.e. a search for the saddle points connected to the given minimum). Ideally, repeated use of these two stages would find all Morse index one saddle points and all minima. We thus try to find all minima in a structured manner where we only consider direct connections between minima and saddle points. For a given minimum, we only need to detect those saddle points for which the optimization paths lead towards that minimum. Other saddle points can then be located from the other minima. In Figure 7.3.1 it is thus not required to find S_2 while using M_1 as initial point for the saddle point detection. It is sufficient to find S_1 so that the local optimization from S_1 results into the location of M_2. However, while initiating a search from M_2, it is required to find both S_1 and S_2.

In this section, we discuss our attempt to develop a global optimization method based on this strategy. First, we will focus on the first step, the saddle point detection. Fortunately, we have to detect only the saddle points with *MI=1,* while those with a higher Morse index, which are more difficult to be detected, can be safely ignored for the present purpose. For shortness, in the rest of this thesis a *MI=1* saddle point will be referred to as a "saddle point".

```
                          ┌─────────────┐
                          │    Start     │
                          └─────────────┘
                                 │
                          ┌─────────────┐
                          │ Initiate a local │
                          │ optimization from │
                          │ an arbitrary point │
                          │ and find a local │
                          │   minimum    │
                          └─────────────┘
                                 │
                          ┌─────────────┐
                          │Detect the saddle points │◄──────┐
                          │with MI=1 connected to │       │
                          │the current minimum │        │
                          └─────────────┘               │
                                 │                       │
                          ┌─────────────┐        ┌─────────────┐
                          │Perturb all newly found │   │Pick new unexplored │
                          │ saddle points and │      │   minimum    │
                          │optimize on both sides │   └─────────────┘
                          └─────────────┘               ▲
                                 │                       │
                              ◇                          │
                       Saddle point                      │
                       detection performed    No ────────┘
                       for all minima?
                              ◇
                               │ Yes
                          ┌─────────────┐
                          │Select lowest minimum │
                          └─────────────┘
```
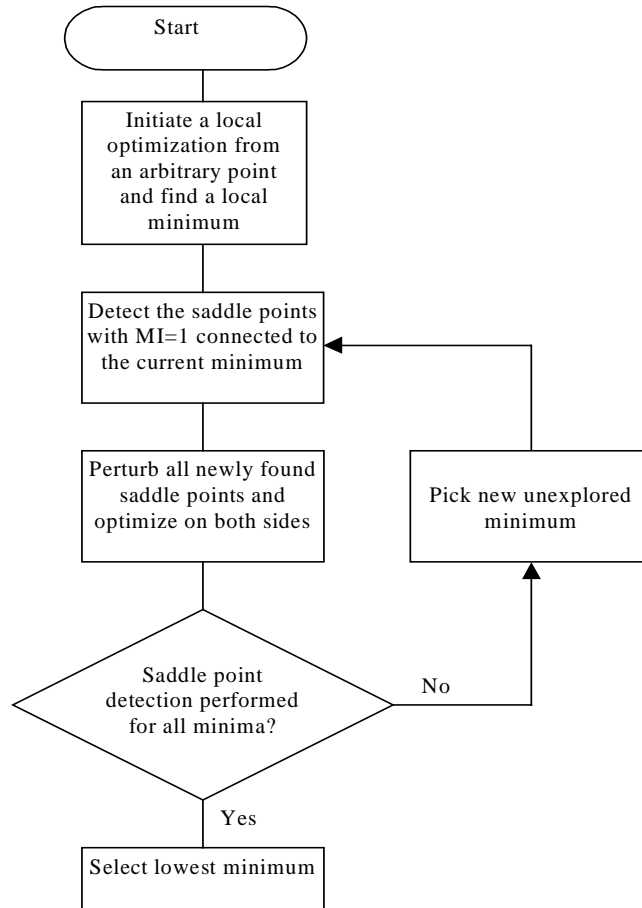
Figure 7.5.1 Flow chart for saddle point based global optimization

Although we may safely ignore saddle points having a Morse index higher than one, detecting all saddle points that connect a given minimum to the rest of the network remains a challenging task. Due to the high dimensionality of the optical MF space and the non-analytical form of the MF, methods that require the frequent computation and inversion of the Hessian matrix are not well suited, as they are too intensive computationally. Furthermore, the frequent usage of constraints in optics requires an algorithm for saddle point detection that is capable of efficiently dealing with (in-) equality constraints.

As it was shown, the local minima within an encircling equimagnitude surface are all connected through optimization paths generated from the saddle points that have a Morse index of 1. Starting from such a saddle point, two distinct local minima can be obtained by means of local optimization only. By detecting the saddle points that connect a given minimum with the remainder of the network, we can in principle systematically detect the complete network of minima (in practice, this strategy works when the number of local minima is not exceedingly large). Once the complete network has been detected, not only the global minimum is known but also the relation between the various minima. A basic algorithm for the detection of the complete network of minima is presented in Figure 7.5.1. Algorithms for finding new local minima based on saddle point detection that have some similarities with our method can be found in papers by Barkema and Mousseau [77]-[79] and by D. Wales [80],[81] where the energy landscape of many atoms is studied.

Search method

We have developed an algorithm for saddle point detection that is based on constrained local optimization. First, a new coordinate system is defined with the origin at an arbitrary local minimum M. In order to detect the saddle points that connect this local minimum with neighboring local minima, we define a set of directions, each characterized by an unit direction vector **s**. (Possible ways to define these directions are discussed further.) For each such direction, we consider the set of hyperplanes orthogonal to **s**

$$s_1 \hat{x}_1 + s_2 \hat{x}_2 + ... + s_N \hat{x}_N = t, \qquad (7.5.1)$$

where t gives the distance between the hyperplane and M along the normal that passes through M. For a given value of t we compute the constrained *minimum* of merit function in the hyperplane given by (7.5.1). Then for an appropriate choice of **s**, these constrained minima form a continuous path connecting the saddle point with the minimum as shown in Figure 7.5.2. Let $\hat{\mathbf{x}}_\mathbf{s}(t)$ and $F_\mathbf{s}(t)$ be the position vector and the value of MF corresponding to this minimum, respectively. Then the points on a given trajectory are uniquely defined by the requirement that the gradient of MF is parallel to **s** for all $\hat{\mathbf{x}}_\mathbf{s}(t)$. Consider now a trajectory $\hat{\mathbf{x}}_\mathbf{s}(t)$ generated with a minimum as initial point. At a minimum, any direction **s** leads initially to an increase of $F_\mathbf{s}(t)$. For a given direction, if we start from the position of M at $t=0$ and increase t gradually, at the beginning $F_\mathbf{s}(t)$ increases. A neighboring saddle point is detected when $F_\mathbf{s}(t)$ reaches a maximum for some value t_{max}, provided that $\hat{\mathbf{x}}_\mathbf{s}(t)$ is continuous for the range $0 < t < t_{max}$ (i.e. no jumps have been observed during the gradual increase of t). This procedure is illustrated in Figure 7.5.3 where the hyperplanes are shifted into an arbitrary direction. It is important to note that not all such searches lead to saddle points; some of them will terminate in dead ends.
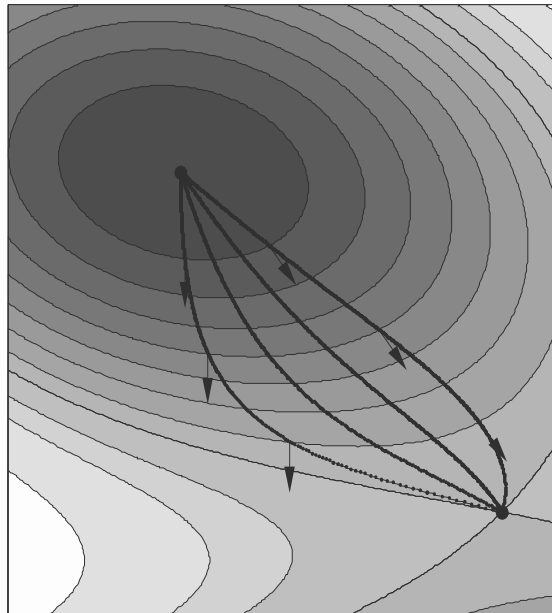
Figure 7.5.2 Paths between a local minimum and a saddle point generated by means of a constrained local minimization orthogonal to a direction s. Each of these paths is defined with a different search direction. Due to the local minimization in a plane orthogonal to s, the gradient direction is constant and parallel to s for all points on a given path. The arrows indicate the direction of the gradient for some points on the paths.

However, a saddle point can only be reached if **s** is such that the saddle point is a maximum into the direction of **s** while it is a minimum orthogonal to that direction. For a saddle point with a given Hessian matrix $Hf(\mathbf{x})$ the search is successful and $\hat{\mathbf{x}}_s(t)$ passes through the saddle point only if

$$\sum [Hf(\mathbf{x})]_{ij}\hat{x}_{s_i}\hat{x}_{s_j} < 0 . \tag{7.5.2}$$

If this condition is not met, the path becomes discontinuous and does not lead to a neighboring saddle point. However, new local minima (situated further away in the network) can still be discovered in this way.
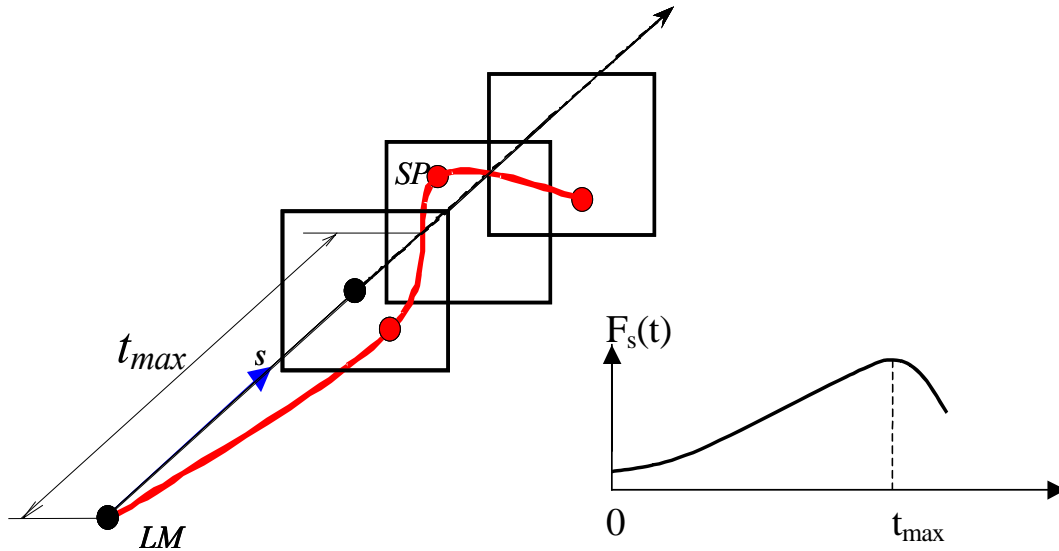
Figure 7.5.3 Saddle point detection by using constrained local minimization. Starting at a local minimum, $F_s(t)$ increases until it reaches a maximum at a saddle point. Although x$_s$(t) may be a complicated trajectory through the design space, the saddle point detection is now effectively a one dimensional maximization problem for $F_s(t)$.

Search directions

One of the most important aspects for successful saddle point detection is a proper initialization of the algorithm. The number of searches performed at each minimum has to be determined as well as the search directions. We will show that choosing search directions randomly is not an optimal solution because the resulting trajectories will be initially concentrated in a narrow cone around the eigenvector with smallest eigenvalue. We first discuss the appropriate choice of search directions and after that, the required number of searches will be considered.

Since the equimagnitude ellipsoids in the immediate vicinity of the point M are often strongly elongated, a useful set of search directions **s** can be determined on the basis of the eigenvectors of the Hessian matrix computed at M. We will show that if we start with an uniformly distributed set of directions **s** (Figure 7.5.4 a), for most directions **s** the corresponding vectors $\hat{\mathbf{x}}_s(t)$, following the MF landscape, will then be concentrated in a narrow cone around the first eigenvector (Figure 7.5.4 b). We also show that if the directions **s** are oriented along eigenvectors the algorithm escapes from this cone and can explore different regions of the solution space.
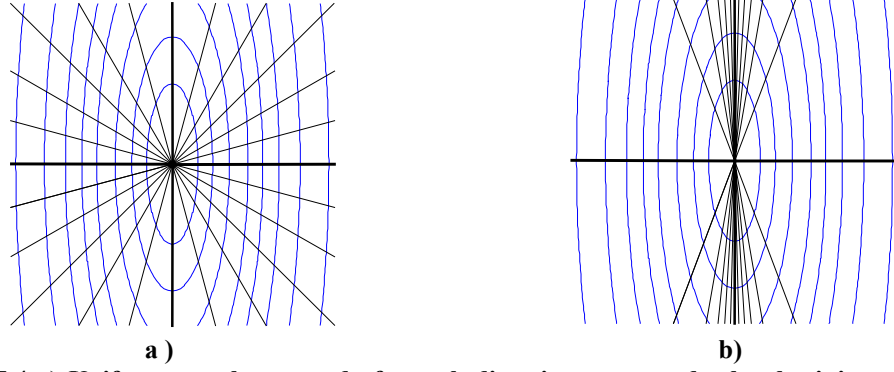
Figure 7.5.4 a) Uniform angular spread of search directions s around a local minimum. b) The corresponding search trajectories $\hat{\mathbf{x}}_s(t)$ for small values of t in the case of elongated equimagnitude surfaces. The search trajectories are oriented in the direction of the corresponding s only if s if oriented along eigenvectors (thick lines), otherwise they tend to be concentrated in a narrow cone along the longest axis of the ellipsoid.

Without prior knowledge of the location of the connecting saddle points, any direction of search may be defined for starting the search at a minimum. However, by initiating multiple searches from a given minimum, we want to explore different regions of the MF space. The probability of detecting all connecting saddle points can then be maximized by generating paths with a maximum spatial separation. To study the spatial separation between paths generated with different directions of search, we consider the quadratic region around a minimum where the equimagnitude surfaces may be approximated by ellipsoids. In this region, the behavior of the MF is completely determined by the Hessian matrix at the minimum. For a given Hessian, $Hf(\mathbf{x})$, the gradient is then given by

$$\nabla f(\mathbf{x_M} + \mathbf{\Delta x}) = Hf(\mathbf{x})\mathbf{\Delta x} = \Lambda \overline{\mathbf{x}}, \qquad (7.5.3)$$

where the diagonal matrix Λ contains the eigenvalues of the Hessian matrix and the components of the vector $\overline{\mathbf{x}}$ are measured along the directions of the eigenvectors of the Hessian matrix.

The minimization orthogonal to **s** ensures that all points on a path generated with a given direction of search have a gradient direction given by **s**. Hence, these points are given by

$$\overline{\mathbf{x}}_s(t) = \gamma(t)\Lambda^{-1}\mathbf{s}, \qquad (7.5.4)$$

where γ is a scaling factor depending on the distance, t as defined in Eq. (7.5.1). In the eigenvector basis, the components of the path vector are then given by

$$\overline{x}_{si}(t) = \gamma(t)\lambda_i^{-1}s_i, \quad i = 1, 2, ..., N. \qquad (7.5.5)$$

Note that when some eigenvalue is very small, the component of the path vector along the corresponding eigenvector tends to be much larger than the other components.

In the two-dimensional example shown in Figure 7.5.5, a search direction **s** is defined with an angle α with respect to the first eigenvector, i.e. the eigenvector with smallest eigenvalue. The corresponding search path $\hat{\mathbf{x}}_s(t)$ is now given by (7.5.4) and this path makes an angle θ with respect to the first eigenvector.

With these definitions we have

$$\tan\theta = \frac{\overline{\mathbf{x}}_2}{\overline{\mathbf{x}}_1}, \tan\alpha = \frac{\mathbf{s}_2}{\mathbf{s}_1}. \qquad (7.5.6)$$
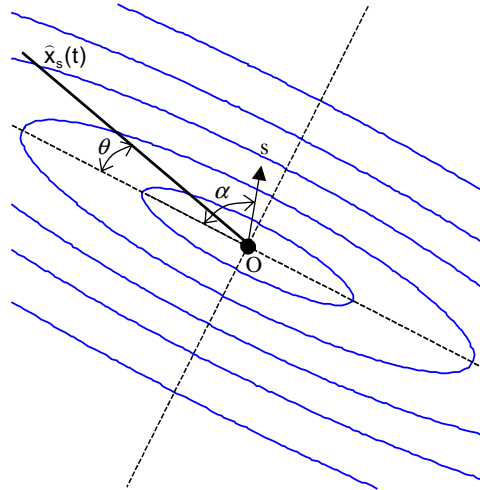
Figure 7.5.5 Path $\hat{\mathbf{x}}_s(t)$ generated with an arbitrary direction s. The angles α and θ are defined with respect to the eigenvector with smallest eigenvalue (the longest axis of the ellipse).
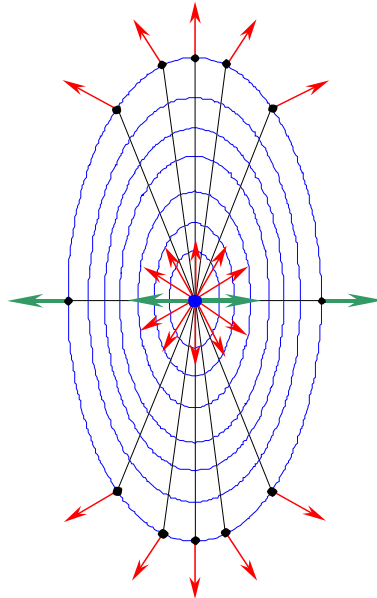
Figure 7.5.6 Paths generated for a set of directions s defined with an angular separation of 30 degrees between them. The arrows indicate the direction of search. Note that most paths are concentrated around the eigenvector with smallest eigenvalue.

It follows then from (7.5.5) that the two angles are related through

$$\tan \theta = \frac{\lambda_1}{\lambda_2} \tan \alpha, \tag{7.5.7}$$

where λ_1 and λ_2 are the eigenvalues of the Hessian matrix at the local minimum. It follows from Eq. (7.5.7) that for very elongated ellipsoids (i.e. $\lambda_1 \ll \lambda_2$) most paths tend to concentrate in a narrow cone around the eigenvector with smallest eigenvalue (see Figure 7.5.6). However, we can use the direction of the second eigenvector of the Hessian matrix (thick horizontal arrow) to escape from the narrow cone around the first eigenvector in order to explore different regions of the MF space. For each eigenvector two searches in opposite directions can be performed so that we have a total number of four independent searches in two dimensions.

In general it follows from Eq. (7.5.5) that by defining the search directions such that they correspond with the directions of different eigenvectors of the Hessian matrix the paths are independent of the eigenvalues of the Hessian matrix. The paths then

initially follow the directions of the eigenvectors and they are mutually orthogonal. In the case of an N-dimensional design space, we can thus define N directions of search corresponding with the directions of the eigenvectors. For each of the eigenvectors, the search can be performed in opposite directions so that the total number of searches is given by 2N. As will be shown below, the directions of the eigenvectors at a minimum can be determined by means of local optimization.

Although a number of only 2N searches might seem insufficient when compared to the number of saddle points that can be encountered in a typical design problem, it should be realized that these 2N searches are performed at each minimum. As noted earlier, at each of these minima, only those saddle points having a direct linkage with the minimum need to be detected. According to our present experience with optical system optimization, most saddle points have been detected several times indicating that 2N searches are usually sufficient. If more than 2N searches are desired, Eq. (7.5.5) can also be used to maximize the separation between these paths by taking into account the eigenvalues at a minimum. However, for complex optimization problems, it might be more efficient to use less than 2N search directions. As the main difference between the Hessian matrix at a minimum and at a saddle point with a Morse index of 1 is the sign of one of the eigenvalues, it might be sufficient to use only those eigenvectors for which the eigenvalues are relatively low as we can expect that those eigenvectors have a higher probability of becoming negative. In our algorithm we use two searches in opposite directions for each eigenvector, i.e. a total of *2N* independent searches for each local minimum.

Original approach to the computation of eigenvectors

As discussed above an important step of the saddle point detection process is the computation of the eigenvectors of the matrix given by Eq. (6.1.7) for the given local minimum, i.e. the orientation of the axes of the ellipsoid shown in Figure 7.2.1. Since this goal must be achieved within an optical design program, we have chosen a technique based on local optimization. We have therefore transformed into a computer algorithm a mathematical idea that is usually used to describe the rotation of axes (shown in Figure 7.2.1) that diagonalizes the matrix $Hf(\mathbf{x})$ [23].
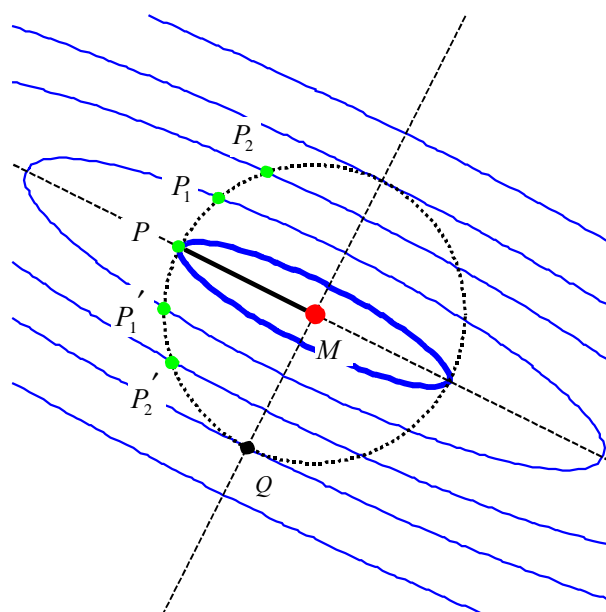

Figure 7.5.7 Computation of the eigenvectors based on local minimization.

Consider around the local minimum M a hypersphere whose radius $r = MQ$ is sufficiently small so that the equimagnitude surfaces that intersect it are ellipsoids given by Eq. (7.2.3) (see Figure 7.5.7). We first compute the direction of the eigenvector that has the smallest eigenvalue, i.e. the direction of the longest axis of the ellipsoids. Since smaller ellipsoids have smaller values of f_0, for the MFs of the points P, P_1 and P_2 in Figure 7.5.7 we can write $f(P_2) > f(P_1) > f(P)$. Therefore, a local minimization of the merit function, constrained on the hypersphere of radius r, will produce as a result one of the two points in which the inscribed ellipsoid (thick curve) touches the hypersphere. Each of these two points can be used to define the direction MP of the eigenvector. In order to improve the precision in our algorithm we find both of these points. First we find one direction (MP) and then we take an opposite direction (PM) as the first iteration in the hypersphere optimization in order to find an independent estimate of the direction of the second half-axis. In order to compute the remaining eigenvectors, we use the fact that they are all orthogonal to each other. We will now use a coordinate system having its origin in M. Thus, if P has the coordinates $\hat{x}_1^1, \hat{x}_2^1, ... \hat{x}_N^1$, the other eigenvectors must be situated in the *N-1* dimensional hyperplane orthogonal to MP, which is given by

$$\hat{x}_1^1 \hat{x}_1 + \hat{x}_2^1 \hat{x}_2 + ... + \hat{x}_N^1 \hat{x}_N = 0 \tag{7.5.8}$$

(In two dimensions, Eq. (7.5.8) is the equation for the direction MQ in Figure 7.5.7) Adding Eq. (7.5.8) as a second constraint and reoptimizing along the hypersphere we obtain the direction of the second eigenvector. By adding for each newly found eigenvector an additional constraint similar to Eq. (7.5.8) and reoptimizing, all eigenvectors are found one after the other.

7.6.   Two-dimensional plots of merit function landscape

In this chapter we focused on the topography of the merit function landscape. Two-dimensional MF plots of equimagnitude contours can be widely used for the analysis of the behavior of the merit function. These plots can provide an additional information about features of MF landscape, such as pathologies (e.g. MF discontinuity), and can explain stagnation regions, SP stability, etc. However it is not trivial to visualize a multidimensional landscape in two dimensions. For this purpose we developed a special tool for generating two-dimensional cuts trough N-dimensional space.

We compute the MF in the plane containing the most important points within the certain region of the merit function landscape. It is known from geometry that each plane can be defined via three points. In our case these three points can be two neighboring local minima (M_1 and M_2) and the corresponding saddle point (S) via which they are connected (see Figure 7.6.1). Sometimes, it is also useful to take a local minimum (LM) and two close points (S_1 and S_2) on opposite sides of a saddle point connected to LM. In this case another local minimum may not be shown. Each point is defined by the set of coordinates like $S(x_1, x_2, ..., x_n)$.

First of all we define two vectors $\vec{V}_1 = M_1 S$ and $\vec{V}_2 = M_2 S$ (see Figure 7.6.1a). Because the length of these vectors can differ substantially, in order to increase precision, the length of the smaller vector should be normalized to the length of the long one (Figure 7.6.1b):

$$\vec{V}_2' = \vec{V}_2 |\vec{V}_1| / |\vec{V}_2| . \tag{7.6.1}$$
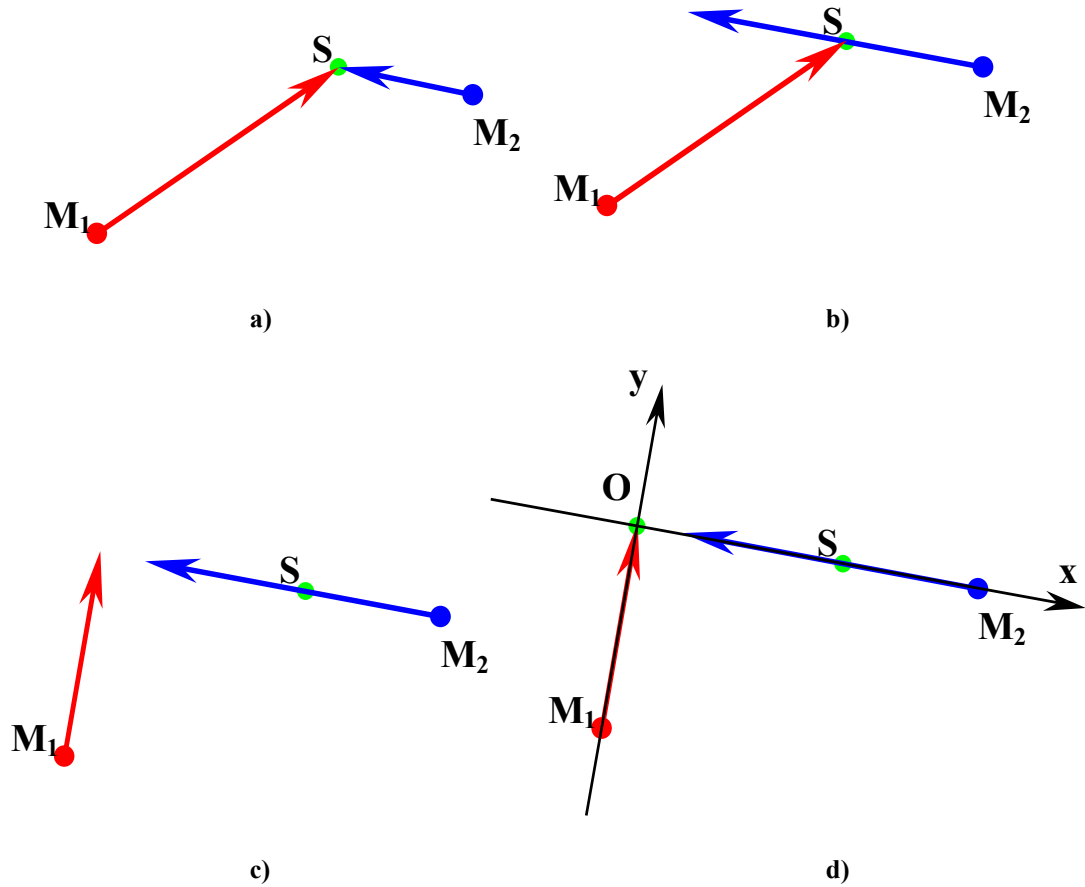
Figure 7.6.1 Definition of the coordinate system for the two dimensional MF plot: a) tree points defining a plane; b) normalizing small vector; c) obtaining orthogonal components; d) introduced coordinate axes.

Sometimes it turns out that directions defined by two vectors are almost collinear and it is useful to choose a new coordinate set by taking orthogonal directions. It can be done by replacing one vector by its component orthogonal to second vector (Figure 7.6.1c):

$$\overrightarrow{V_1}' = \overrightarrow{V_1} - \overrightarrow{V_2}'\left(\overrightarrow{V_1}\cdot\overrightarrow{V_2}'\right)/\left|\overrightarrow{V_2}'\right|^2. \tag{7.6.2}$$

Finally, a new coordinate system is introduced (Figure 7.6.1d). The saddle point and one local minimum are situated on one axis and the second local minimum is situated on another axis. An arbitrary point P in the plane can then be defined as

$$P = x\overrightarrow{V_1}' + y\overrightarrow{V_2}', \tag{7.6.3}$$

where x and y are coordinates in the new coordinate system. In order to draw a two dimensional plot, the MF value should be computed for x and y changing in predefined limits.

In the general case we will observe the two starting local minima with one saddle point between them, but occasionally the presence of other critical points can be observed in the drawing region (see Figure 7.6.2). In principle this cutting plane can be generalized to a more complicated surface, defined not by three but by more crossing point.

We have used this visualization tool whenever we have encountered unexpected behavior in our saddle points detection. The insight obtained in this way has helped us to improve our algorithms.
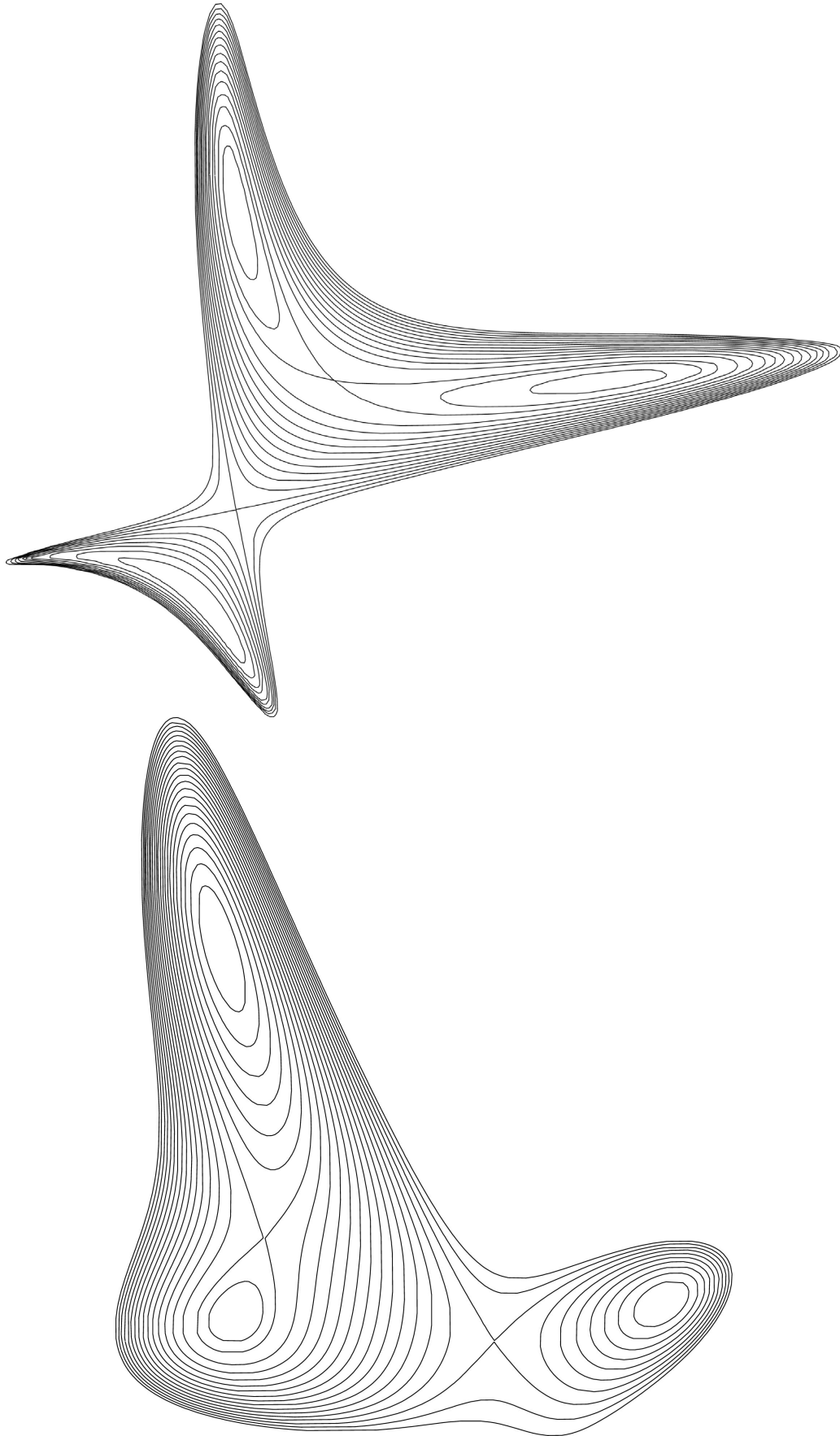
Figure 7.6.2 Examples of two dimensional cuts through multidimensional merit function space.

7.7.   Conclusions

In this chapter we have examined the properties of the optimization solution space from what mathematicians might call a topological perspective. Because this high-dimensional space is usually very complicated, it is unmanageable without focussing on particular features.

We have shown a special role of the saddle points in the merit function landscape in optical system design. By analyzing the splitting or merging of the equimagnitude surfaces when the corresponding MF value changes, we have observed that the local minima of the merit function landscape in optical system design form a network. Based on this idea, a new type of global optimization algorithm has been proposed. The detailed techniques for the saddle point detection and choice of the search directions were discussed. A simple saddle point detection example and an original method for the computation of eigenvectors were presented as well. A special tool for the visualization of the multidimensional merit function landscape in two dimensions has been developed.

The algorithms based on this new "saddle point" concept might, in principle, not only reproduce or supplement the results of presently known global optimization algorithms, but also provide additional insight into the topography of the MF landscape, as will be discussed in the next chapter.

8. Optical system networks

We have shown in the previous chapter that, when certain quite general conditions are satisfied, the MF landscape in optical system design has a remarkable property. The local minima form then a network in which all nodes are connected via links that contain a special type of saddle point. We will illustrate our idea and show in this chapter examples of networks of optical systems. First we start with simple systems and analyze the topography of the merit function landscape, then we pass on to the optical systems with many variables. Because there are plenty of known optical systems we will focus on the features of the most well known objectives. As will be seen the regularities for these systems observed by us were not reported before and they are valid for more sophisticated optical systems as well.

In the preceding chapter we have also described the algorithm exploring link by link the entire network of local minima with the help of constrained local optimization for detecting the SPMI1. We have implemented this algorithm in our computer program NETMIN which uses for the local optimization and ray tracing the commercial optical design program CODE V. These two programs communicate via the Windows COM interface. Our program is also able to work in stand alone mode and to find saddle points and local minima of arbitrary continuous mathematical function of many variables. In this case we use the local optimization algorithm of IMSL Numerical Library [82]. Here, we present results obtained for MF spaces of simple optical systems consisting of several elements.

We will also study the properties of the robust SPMI1 in the case of lens systems consisting of spherical surfaces in which the distances between surfaces are negligibly small. As will be shown in section 8.3, these systems are simple enough so that basic properties of the set of saddle points can be predicted analytically.

8.1. Single lens

The simplest optical system, which has one free significant parameter for optimization is a singlet. In this case, if we limit the design by using only spherical surfaces, we have only the following optimization options: two curvatures, one lens thickness and choice of glass type. Moreover in the case of a thin component (when the lens thickness is much smaller than the focal length) the thickness does not influence the merit function significantly. The proper choice of the glass type and a slight defocus allow to change the magnitude of the merit function but not the topography of the MF landscape. Normally one of curvatures is used to keep required focal length or magnification constant and we finally can change only one curvature to optimize for the better image quality. Usually, because of large aberrations, this system can be used for the imaging purposes only in the case of small aperture and field. In the case of infinite object distance and using the merit function of Code V (in which the image defects are transverse ray aberrations computed with respect to the chief ray), we have only one solution, which is an almost plane-convex lens oriented as shown in Figure 8.1.1. The unicity of solution is shown by the merit function plot in Figure 8.1.2, which has only one minimum within the possible change of the first curvature, without ray failure.

Optical system networks
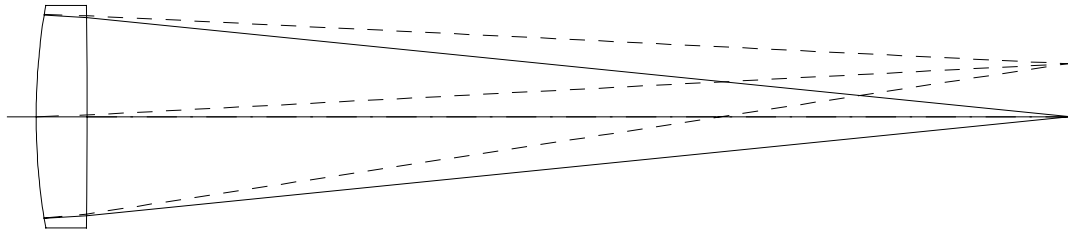
Figure 8.1.1 The unique local minimum for a lens singlet with an object in infinity. The system specifications are as follows: focal length 100 mm, F number 1:5, field of view 10 degrees, working wavelength range 656…486 nm.
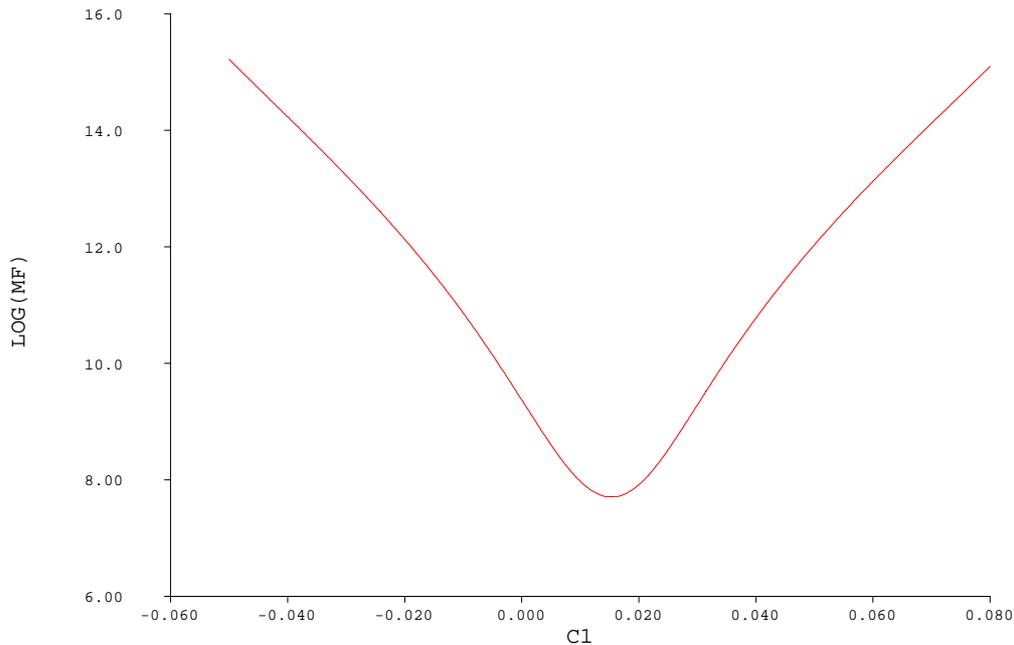
Figure 8.1.2 The merit function plot corresponding to the optical system shown in Figure 8.1.1. The first curvature is used as optimization variable and the second curvature is used to keep the focal length constant.

8.2. Cemented Doublet

If we add optimization variables one by one the next step will then be the cemented doublet: two lenses with different glass types, having one common surface. In this case we have three curvatures (two free parameters if thickness are frozen) but still only one solution has been found because the internal surface allows to compensate only the longitudinal chromatic aberration. However the shape of lenses in this single solution depends on choice of glass for the components. Thus, if the combination of glasses crown-flint is used for the first and second lenses correspondingly then the optimization leads to the solution shown in Figure 8.2.1a. In the flint-crown case we have another solution shown in Figure 8.2.1b. The contour plot of 3D MF landscape is shown in Figure 8.2.2. It can be seen that we have only one local minimum for each glass combination and the topography of the MF landscape is almost symmetric. The merit function landscape is very robust to the aperture and field change. It can be observed from Figure 8.1.2c and Figure 8.1.2d that the shape of the MF function landscape does not change significantly even for increased values of aperture and field.

a)

b)
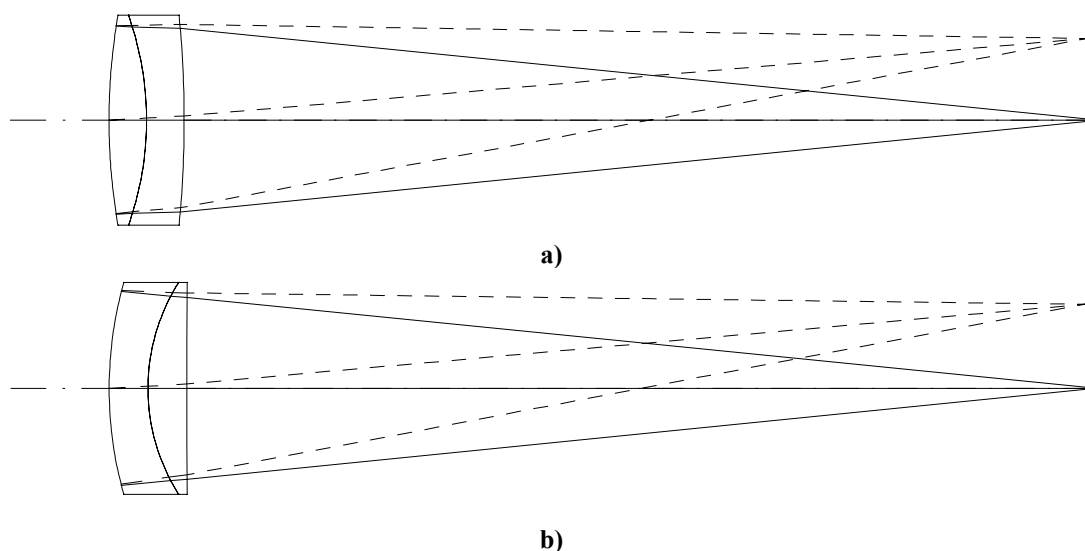
Figure 8.2.1 The two solutions of cemented doublet (focal length 100 mm, F number 1:5, field of view 10 degrees, working wavelength range 656…486 nm). a) crown-flint combination (glasses BK7 and F2 from Schott catalog are used); b) flint-crown combination (F2/BK7).

a)

b)

c)

d)
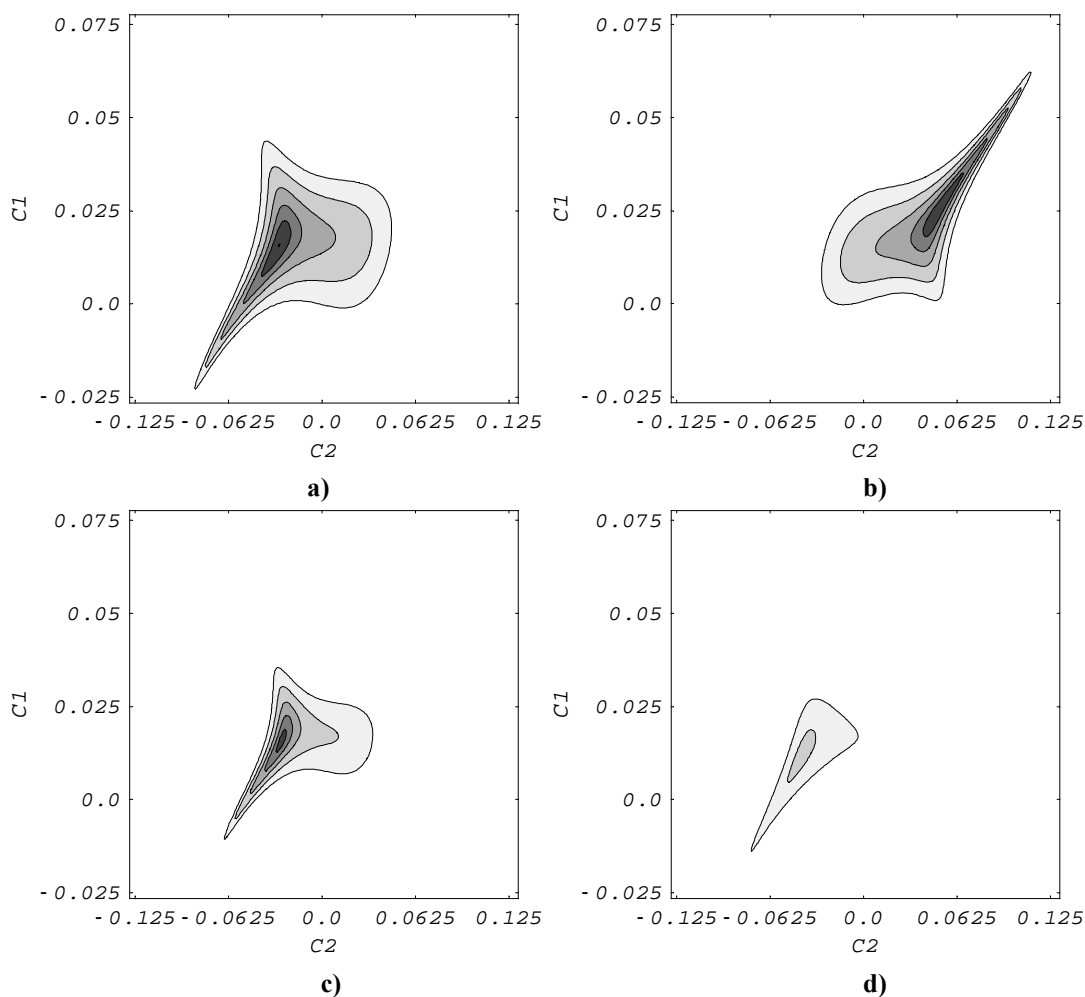
Figure 8.2.2 The contour plot of the merit function landscape in the case of the cemented doublet shown in Figure 8.2.1: a) crown-flint combination (BK7/F2); b) flint-crown combination (F2/BK7); c) aperture increased up to 1/4, d) field size increased up to 20 degrees.

8.3. Saddle points in the MF landscape of systems of thin lenses in contact

In order to understand the features of the saddle points we will analyze in this section the simplest possible optical systems: lens systems consisting of spherical surfaces in which the distances between surfaces are negligibly small. We will show that the MF landscape of these systems has surprising regularities, which can be modeled by thin-lens theory.

Two-dimensional analysis of a doublet

Remarkable properties of the MF landscape of systems of thin lenses in contact can already be observed for separated doublets if two-dimensional plots of the equimagnitude contours are carefully analyzed. In Figure 8.3.1 such a plot is shown for a doublet which, for simplicity, is monochromatic. (Axial color correction will be included for systems discussed in the next section.) As in the other cases, discussed in this chapter, the object is at infinity and the merit function is the default error function of CODE V. If we use the curvature c_4 of the last surface to keep the focal length constant and use the curvature c_1 of the first surface as a control parameter, the two remaining curvatures can be used as variables. (In all MF plots in this section the curvature c_2 of the second surface is along the vertical axis and c_3 of the third surface is along the horizontal axis.) A plot very similar to Figure 8.3.1 has also been shown by Sturlesi and O'Shea [83].

In Figure 8.3.1 we see four MF local minima and three MF saddle points. As expected, the best three local minima are located almost on the contours for third-order spherical aberration (SA) equal to zero and close to the zero coma contours. These local minima are also obtained by optimizing downwards from the three MF saddle points. In two-dimensional plots, the saddle points can be easily recognized. As shown in Chapter 7, close to the saddle point, the equimagnitude contours must be hyperbolas. For the value of the MF, corresponding to the saddle point itself, the contours degenerate into a pair of straight lines (the asymptotes of the hyperbolas).

Note that the saddle points of the MF (the small black points in Figure 8.3.1) are situated very close to the SA saddle points (the points where the thick gray lines cross in Figure 8.3.1b). A first remarkable property of the saddle points in this landscape is that they are situated at the intersection points of three almost straight SA equimagnitude contours. In order to explain this and other surprising properties of the MF SPMI1, we use here a simplified merit function model in which:

- Only SA, the dominant aberration for the systems under investigation, is considered;
- The imaging is monochromatic and all glasses are identical;
- Thin-lens theory will be used, i.e. in all formulas the distances between lens surfaces will be put equal to zero.

If in a power series expansion for the transverse aberration of a given ray we keep only the SA contribution and neglect the rest, then for all rays the transverse aberration will be proportional with SA. If MF is a weighted sum of squares for the transverse aberrations of a given set of rays, it will be proportional with SA^2. Assuming that for MF SPMI1 the SA is nonzero, in our model these points, which are solutions of the system of equations $\nabla MF=0$, will also have the property $\nabla SA=0$. (The nabla operator ∇ has as components the partial derivatives with respect to the variables according to (7.2.2))
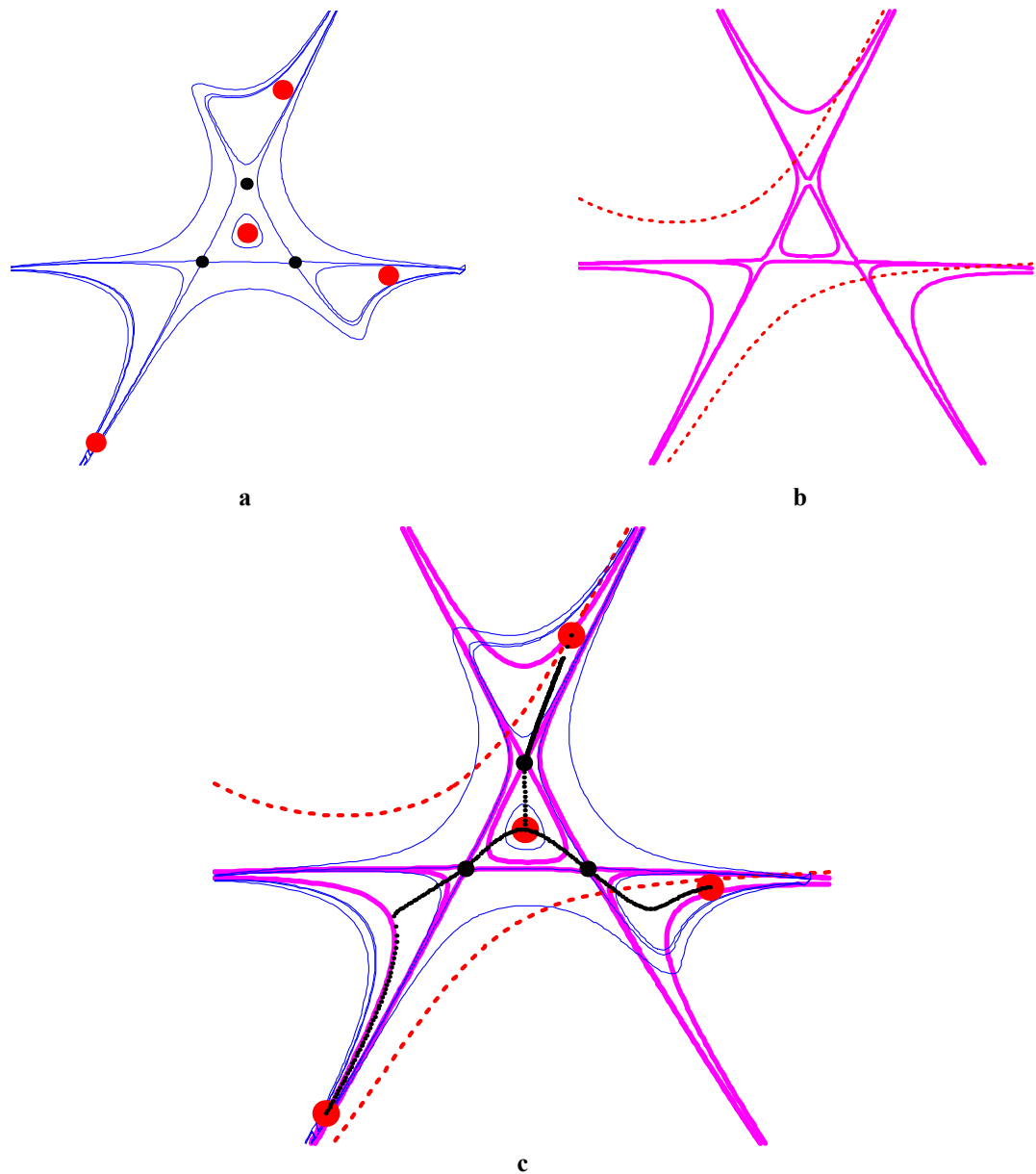
Figure 8.3.1 Topography for typical values of c_1 of a two-dimensional monochromatic doublet landscape (focal length is normalized to 1, F number 3, field of view of 6 degrees, and the lens thicknesses are small). a) MF equimagnitude contours , local minima (large gray points) and saddle points (small black points). b) The contours for zero SA and the contours that correspond to the saddle points (thick gray lines). The contours for third-order coma equal to zero are shown as well (thin dashed lines). Note how the saddle point SA contours separate the zero SA contours (the strongly curved ones) in three different branches. c) Figures a) and b) superimposed. In addition, the network links between saddle points and local minima are shown (dotted curves).

In the thin-lens approximation, we can write the third-order spherical aberration of a doublet as

$$SA = h^4 \left(f_0 + \alpha f_1 f_2 f_3 \right), \tag{8.3.1}$$

where we have used the abbreviations

Optical system networks

$$f_0 = \frac{n^2}{(n-1)^2} + \frac{c_1^2(n+2)}{n} - \frac{c_1(2n+1)}{n-1}, \tag{8.3.2}$$

$$f_1 = c_1 - c_2 - \frac{1}{n-1}, \tag{8.3.3}$$

$$f_2 = c_2 - c_3, \tag{8.3.4}$$

$$f_3 = 2c_2(n^2-1) + c_3(n+2) - \frac{n(2n+1)}{n-1} + c_1(n-2n^2+4), \tag{8.3.5}$$

and

$$\alpha = \frac{n-1}{n}. \tag{8.3.6}$$

The fourth curvature, which does not appear explicitly in Eqs. (8.3.1-8.3.6), is used to keep the total power equal to 1. In these formulas n is the refractive index of the two glasses and h is the marginal ray height at the lens. (Since the aperture stop is placed at the lens, h is equal to half the stop diameter.) One way of obtaining these equations is by using for the doublet the well-known Coddington thin-lens formulas [84], [85]. Alternatively, these equations (and especially their equivalents for a larger number of lenses, which will be discussed in subsequent section) can be directly obtained with computer algebra software by putting the distances between surfaces equal to zero in the well-known formulas [85] that give the surface by surface contributions to SA for lenses with finite thickness and rearranging the result. Also, these equations can be directly verified by computing the SA with commercial optical design software (again by putting the distances between surfaces equal to zero). For instance, CODE V lists the quantity SA/(-2h).

The condition ∇SA=0 with $\nabla = (\partial/\partial c_2, \partial/\partial c_3)$ leads to a system of two nonlinear equations for the two unknowns c_2 and c_3. (Recall that c_1 is used in this section as a control parameter, not as a variable.) It follows after some simple algebra that this system of equations has four solutions. An examination of the eigenvalues of the Hessian at the solutions shows that three of them are saddle points. It turns out that the three saddle points are the solutions of the linear systems of equations f_1=0 and f_2=0, f_1=0 and f_3=0, f_2=0 and f_3=0, respectively. (Note that f_1, f_2, and f_3 are linear functions of the curvatures.)
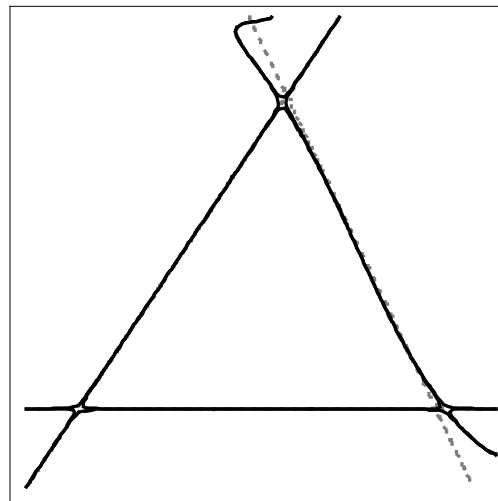
Figure 8.3.2 MF and SA equimagnitude contours that pass through the saddle points (MF drawn in black line, SA drawn in gray dashed line) for a doublet with zero thickness, n=1.5, F number 3 and field of 6 degrees.

Thus, in the two-dimensional SA plots the saddle points are located at the three intersections of the straight lines $f_1=0$, $f_2=0$, and $f_3=0$, taken in pairs of two. It follows from Eq. (8.3.1) that within the frame of our approximate model, along these lines SA remains unchanged, $SA = h^4 f_0$, i.e. these lines form an equimagnitude contour. In fact, the existence of two of these straight equimagnitude lines can be understood from basic principles even without using Eqs. (8.3.1)-(8.3.6). It can be easily shown from the fact that the fourth curvature is used to keep the total power equal to 1, that the condition $f_1=0$ means that along this line we have $c_3 = c_4$. The condition $f_2=0$ means $c_2 = c_3$. Since the distances between the surfaces are zero, in both cases all light rays pass undeviated through the corresponding pair of surfaces, regardless of the common value $c_3 = c_4$ or $c_2 = c_3$. Therefore, for zero thickness $f_1=0$ (horizontal line in Figure 8.3.2) and $f_2=0$ (left oblique line), remain equimagnitude contours even if other aberrations, including higher order ones, are included, i.e. these lines are MF contour lines as well. On the other hand the right oblique line is straight only for SA ($f_3=0$). Note that in Figure 8.3.1 the SA contour lines passing through the saddle points are slightly curved because of small but nonzero lens thickness.
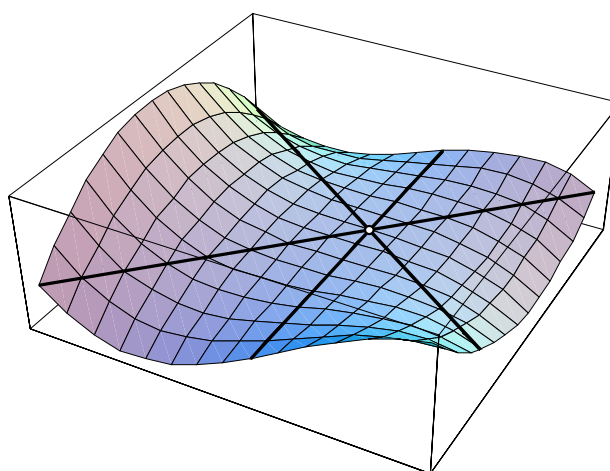
Figure 8.3.3 The SA "monkey saddle" point and the three straight equimagnitude lines that pass through it. At this point all elements of the Hessian matrix are zero, and the shape of the "monkey saddle" is determined by cubic terms.
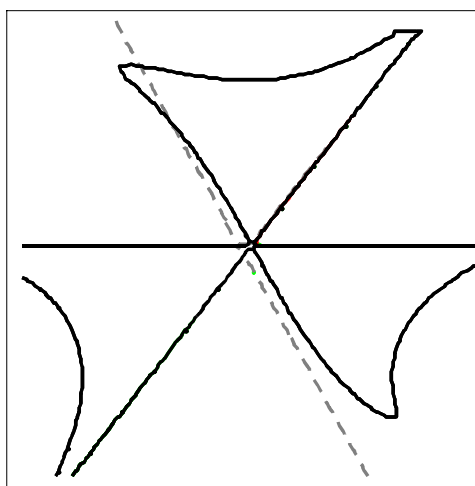
Figure 8.3.4 MF "monkey saddle" (black lines) for $c_{1,crit}=3.55$ in the same doublet as in Figure 8.3.3. Because the MF critical value is slightly different from the value given by Eq. (8.3.7), the SA line $f_3=0$ (dashed gray line) does not pass exactly through the MF monkey saddle.

In the middle of the triangle formed by the three saddle points we find a fourth solution with $\nabla SA=0$. (See Figure 8.3.1.) For values of the control parameter c_l that are not too large, this point (which will be called in what follows the "hub" of the network) is a minimum. Despite the fact that MF of the hub is poor, this minimum plays an essential role for the connectivity of the network. On one side, all three saddle points are linked with the hub.

When c_l increases, the distances between the saddle points decrease and for values of c_l larger than a critical value the hub becomes a maximum. (The network is then linked in a way that is different from the one shown in Figure 8.3.4) Within the frame of the simplified model the critical value is given by

$$c_{l,crit} = \frac{n(2n+1)}{(n-1)(n+2)}.$$ (8.3.7)

For example, for $n=1.5$ we have $c_{l,crit} = 24/7 = 3.43$. When $c_l = c_{l,crit}$ the three equimagnitude lines pass through the same point. The three saddle points and the hub merge then into that single point. The SA landscape around this point takes then the peculiar shape sometimes called a "monkey saddle" [86]. (See Figure 8.3.3. Note the difference between this figure and Figure 7.1.1) For doublets with zero thickness, for a slightly shifted critical value of c_l the "monkey saddle" can also be observed for the MF, where aberrations other than SA play a role as well (Figure 8.3.4).

Network of local minima and saddle points for the doublet

For a monochromatic split doublet search, the network of MF local minima and SPMI1 detected with the program NETMIN is shown in Figure 8.3.5. The systems have small equal distances between surfaces and all three independent curvatures are used as variables. In the three-dimensional variable space, the local minima LM1 and LM5 and the saddle point S5 between them are situated close to the same SA=0 surface branch and the MF differences between them turn out to be low.

In the network, the pair of systems formed by saddle point S5 and local minimum LM1 is therefore less robust than the rest of the network. As mentioned in Chapter 7, such points can appear or disappear more easily when specifications or the MF type are changed. When a saddle point disappears, one of the two local minima linked to it always disappears as well. The local minimum and the saddle point situated on the other side of the pair which has disappeared will then be linked together, so that such appearances or disappearances do not affect the connectivity of the network. A typical example for this behavior can be found in the Cooke triplet global search (see section 8.4).

The other systems in Figure 8.3.5 are robust. For instance, their shape and the links between them are not affected by minor changes in the merit function definition. As mentioned before, for determining the links of a saddle point we use two points situated close to it on both sides along the downward direction. We have also converted the pairs of CODE V files for the saddle points to the ZEMAX and OSLO optical design programs [71], [87]. Optimizing the converted files with the RMS Spot Radius merit function in ZEMAX and the standard optimization function of OSLO leads to local minima that strongly resemble the corresponding local minima in Figure 8.3.5. (The files for the systems in the network are made available in all formats via the web site [88].)

Optical system networks
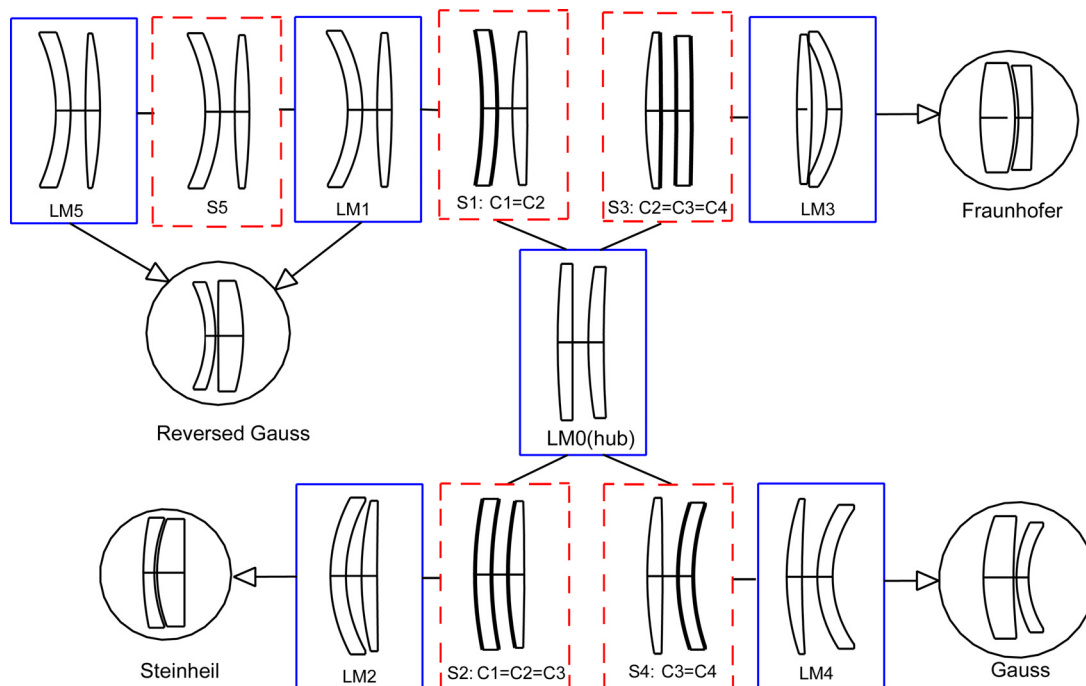
Figure 8.3.5 Local minima (drawn within continuous-line rectangles) and saddle points (within dashed rectangles) for a monochromatic doublet search with F number 5, field of view 6 degrees, and *n*=1.5. The lines between rectangles show how these systems are linked in a network. For the saddle points, the surfaces with nearly equal curvatures have been drawn with thick lines. The basic achromatic doublet shapes are shown within circles. The arrows indicate which monochromatic local minima leads to them, after local reoptimization for color correction. For the Reversed Gauss and Steinheil systems, the V values of the two glasses are 30 and 55 respectively. For the Gauss and Fraunhofer systems, the glass order has been reversed. At this stage, the thicknesses of the achromatic doublets have also been adjusted.

The existence of the robust systems in Figure 8.3.5 can be explained with our simplified SA model. If all three independent curvatures of the thin doublet are used as variables, the equation ∇SA=0 with $\nabla = \left(\partial / \partial c_1, \partial / \partial c_2, \partial / \partial c_3 \right)$ has as solutions four SA SPMI1 and a minimum, the hub, at the center of the tetrahedron formed by the SPMI1. In the three-dimensional variable space, for each SPMI1 the downward direction (i.e. the direction of the eigenvector of the Hessian that has a negative eigenvalue) is approximately given by the line that passes through the given saddle point and through the hub. Along this direction, the SPMI1 is a maximum, whereas in a plane perpendicular to it the SPMI1 is a minimum. All SA SPMI1 have the same SA value. Interestingly, the SA value is also constant along all edges of the tetrahedron having the four SA SPMI1 as vertices.

In the two-dimensional analysis of the previous section we have found three saddle points, one at the crossing of the lines $c_2 = c_3$ and $c_3 = c_4$ and two others, one on each of these lines. One of the two-dimensional saddle points has thus three equal curvatures $c_2 = c_3 = c_4$, and the other two have two equal curvatures, $c_2 = c_3$ and $c_3 = c_4$, respectively. With the first curvature now variable, the four SPMI1 follow the same pattern. For two of them three successive curvatures are equal and for the other two SPMI1 two curvatures are equal, the first two curvatures and the last two curvatures, respectively. (See Table 8.3.1.) Note that in Figure 8.3.5 the robust MF saddle points, which have been detected numerically, have these properties as well. As predicted by the simplified model, on one side all the robust saddle points are linked with the hub. Although this local minimum is a poor one (the Seidel aberrations are not corrected), it is an interesting example of a relaxed optical

configuration [89]. On the other side, the robust SPMI1 are linked with local minima that begin to resemble the familiar achromatic doublet shapes.

Table 8.3.1 The curvatures of the four SA SPMI1 for a thin-lens doublet with n=1.5

	Equal curvatures	c_1	c_2	c_3	c_4
S1	$c_1 = c_2$	-12/7	-12/7	12/7	-2/7
S2	$c_1 = c_2 = c_3$	12/7	12/7	12/7	-2/7
S3	$c_2 = c_3 = c_4$	12/7	-2/7	-2/7	-2/7
S4	$c_3 = c_4$	12/7	-2/7	22/7	22/7
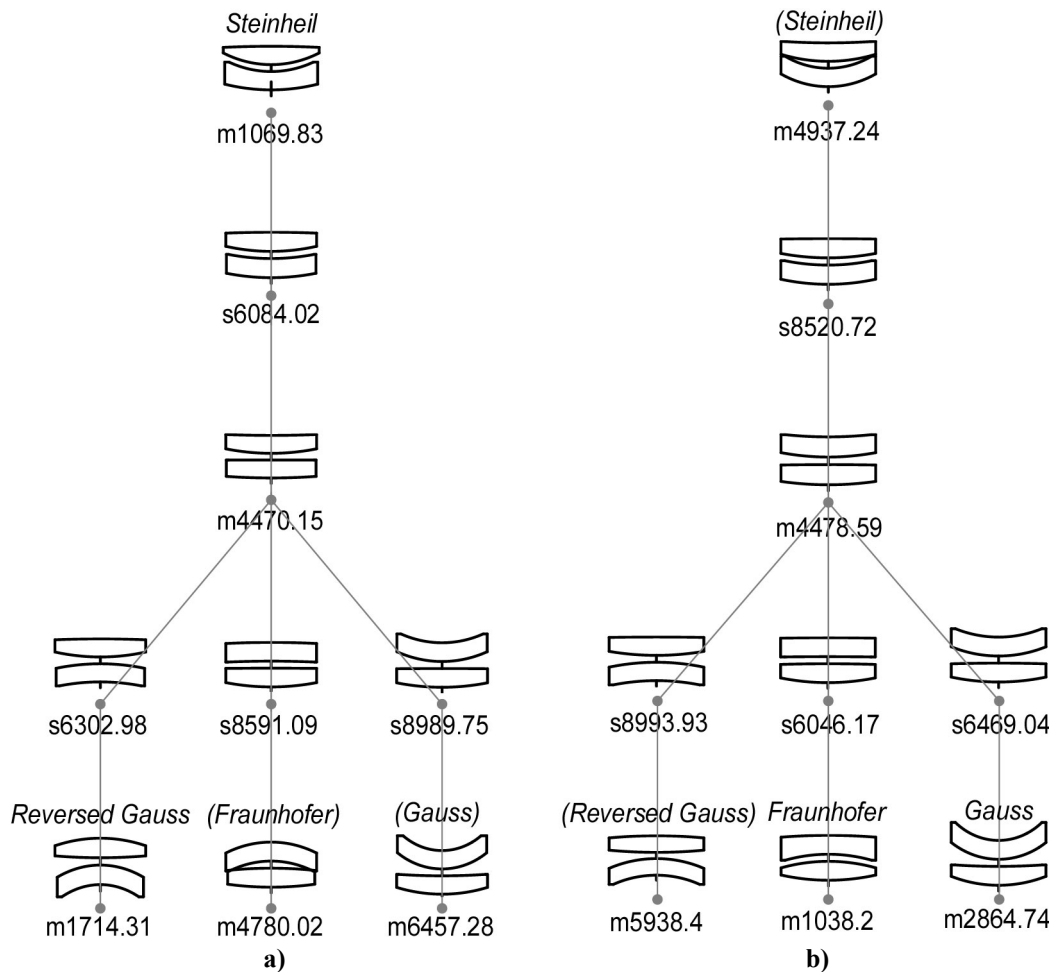
Figure 8.3.6 The networks of local minima and saddle points for a separated doublet with corresponding MF values (object distance is infinity, focal length 100 mm, F number 1:5, field of view 10 degrees, working wavelength range 656…486 nm, lens thicknesses of 4 mm). The "m" systems are local minima, and the "s" systems are saddle points with Morse index 1: a) flint-crown glass combination (F2/BK7); b) crown-flint glass combination (BK7/F2).

For practical purposes, doublets have to be corrected for axial color as well. As well known, there are four basic shapes for split achromatic doublets [90], [91]. These shapes result from thin-lens theory as the possible ways to correct SA, coma and axial color with the three available curvatures. Interestingly, as shown in Figure 8.3.5, the basic shapes can be obtained from the monochromatic local minima by locally reoptimizing them for color correction with appropriate glasses. The zero-power meniscus lenses of the thin-lens SA saddle points become then negative power lenses, as required for correcting axial color.

An example of a network of doublet with real thicknesses and increased field of view obtained with our NETMIN program is shown in Figure 8.3.6. As we will see later a two-dimensional graph captures the essentials of the topography in a MF landscape having a high dimensionality. The lines between systems show how the systems are linked together via "minimum elevation" paths. For each such path, the MF difference between the saddle point and the local minimum gives the height of the MF barrier that must be overcome in order to reach from a given local minimum the basin of attraction of a neighboring one. If desired, the regions of interest in the network can be studied link by link, for instance by examining the way the optimization variables change along the links. In this way, additional insight in the highly complex MF topography can be obtained.

It is seen from Figure 8.3.6 that the theoretically predicted network is robust enough and remains even for real working parameters. However the merit function landscape changes depending on the chosen glass combination because the chromatic aberration is included. It is obvious that Steinheil and Reversed Gauss solutions are preferable in case of flint-crown combination with negative first lens whereas Fraunhofer and Gauss solutions are preferred in case of crown-flint combination where the first component is positive. Remarkably, at the same time the MF value for the hub almost does not change and the MF value of the saddle points interchange crosswise (Steinheil - Fraunhofer and Gauss - Reversed Gauss). The systems corresponding to the saddle points are very similar to those obtained in the case of the thin monochromatic doublet in Figure 8.3.5.

Systems of more than two thin lenses in contact

For thin lenses in contact, the simplified zero-thickness SA model predicts that the robust SPMI1 in the corresponding networks form an amazingly regular pattern. For $m>1$ lenses, $2m-1$ curvatures from the total set of $2m$ curvatures are independent variables. It turns out that there are $2m$ SA SPMI1 that form a hyper-tetrahedron having again a hub at its center. When the total power is 1, the sets of curvatures for the saddle points can be obtained as follows:

Consider first the sequence of points $p_1, p_2, p_3, ...$ given by

$$p_{2k} = p_1 + (k-1)d, \qquad p_{2k+1} = -p_1 + (k-1)d \qquad (8.3.8)$$

with $k = 1,2,3,...$ and

$$p_1 = -\frac{n(2n+1)}{2(n-1)(n+2)}, \qquad d = \frac{2(n+1)}{n+2}. \qquad (8.3.9)$$

Table 8.3.2 The curvatures of the six SA SPMI1 for a thin-lens triplet with n=1.5

	Equal curvatures	c_1	c_2	c_3	c_4	c_5	c_6
S1	$c_1 = c_2$	**-6/7**	**-6/7**	**6/7**	**-1/7**	11/7	4/7
S2	$c_1 = c_2 = c_3$	**6/7**	**6/7**	**6/7**	**-1/7**	11/7	4/7
S3	$c_2 = c_3 = c_4$	**6/7**	**-1/7**	**-1/7**	**-1/7**	11/7	4/7
S4	$c_3 = c_4 = c_5$	**6/7**	**-1/7**	**11/7**	**11/7**	11/7	4/7
S5	$c_4 = c_5 = c_6$	6/7	-1/7	11/7	4/7	4/7	4/7
S6	$c_5 = c_6$	6/7	-1/7	11/7	4/7	16/7	16/7

The first SA SPMI1, S_1, has then the curvatures $c_{1i} = p_i/(m-1)$, with $i=1,...,2m$. For $k>1$, the curvatures of the saddle point S_k are given by $c_{k,k-1} = c_{kk} = p_{k+1}/(m-1)$ and $c_{ki} = c_{k-1,i}$ for $i \neq k-1$ and $i \neq k$. Table 8.3.1 and Table 8.3.2 show the resulting values for the curvatures of the SPMI1 in the case of a doublet and a triplet, respectively. Note that

the 4x4 curvature matrix in Table 8.3.1 differs from the corresponding 4x4 submatrix (shown with bold italic font) in Table 8.3.2 only by a factor 2 (that results from the division with m-1).

In the general case, we encounter a structure that is a generalization of the one for the doublet. The first SA SPMI1 has $c_1 = c_2$, for $2m>k>1$ S_k has $c_{k,k-1} = c_{kk} = c_{k,k+1}$, and S_{2m} has $c_{2m,2m-1} = c_{2m, 2m}$.
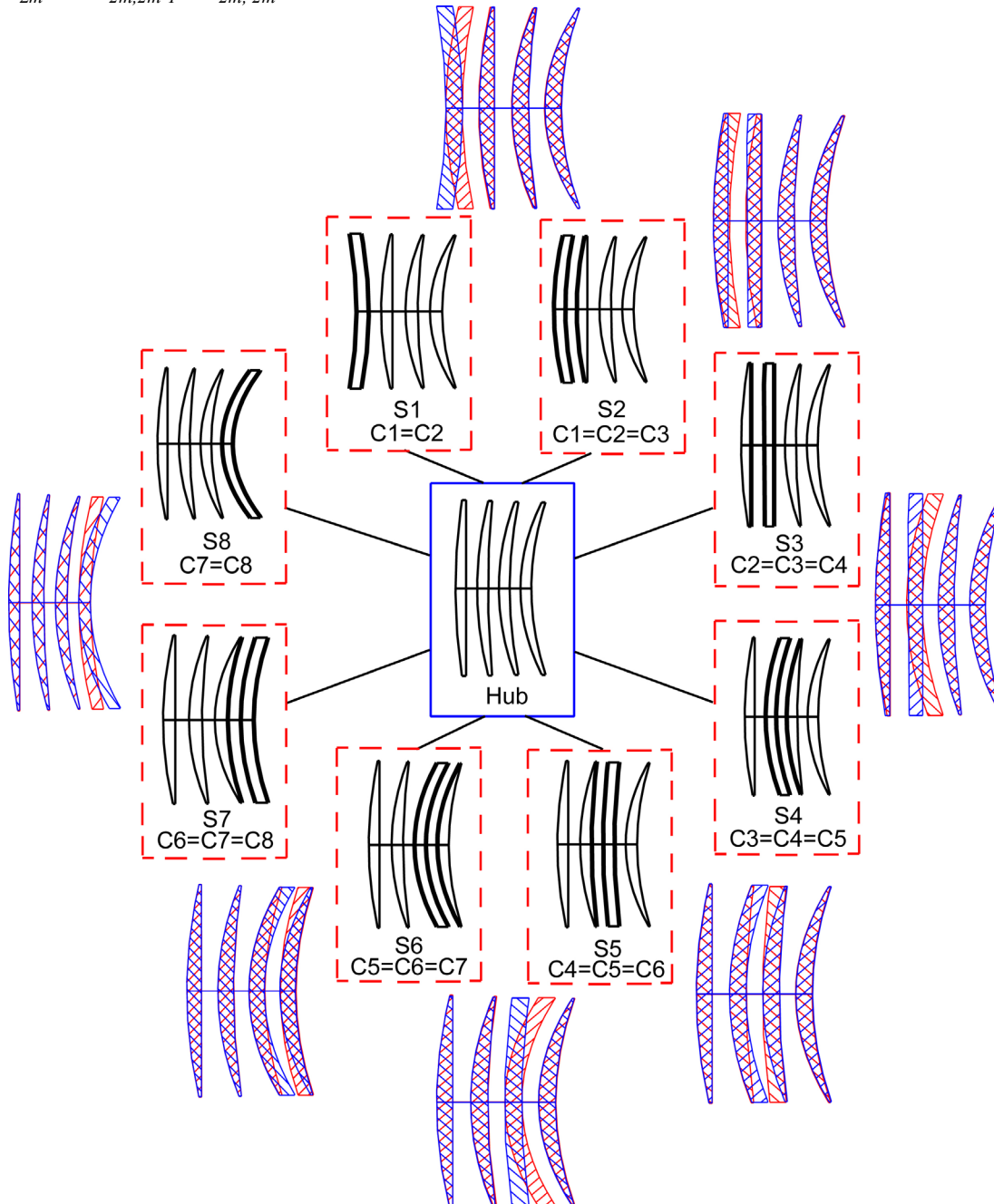
Figure 8.3.7 The hub and the eight robust MF SPMI1 around it in the case of a monochromatic quartet topography. All systems have been detected numerically. The systems have F number 5, field 6 degrees, and n=1.5. The distances between consecutive surfaces are equal, such that the total distance between the first and the last surface is 14% of the focal length. For better comparison, on the outer ring figures of successive saddle points have been superimposed. Since the curvatures of the systems are small, the aspect ratio of the plots has been changed so that the curvatures appear larger. Since this graphical change causes the thicknesses to appear too large, the thicknesses have also been reduced in the drawings.

Figure 8.3.7 shows the robust MF SPMI1 and the hub linked to them for a monochromatic quartet with small, but nonzero distances between surfaces. Despite the fact that the values of the curvatures differ somewhat from the ones computed with the simplified SA model, the structure mentioned above remains valid for the MF saddle points detected numerically. Moreover, note that, when we move from a MF saddle point to the following one, only one pair of consecutive surfaces changes significantly, while the other surfaces remain basically unchanged, as predicted by the simplified model. For a triplet, a figure having the same properties as Figure 8.3.7 can be obtained as well.

While for a doublet the hub is a poor quality local minimum, Fulcher has shown that for $m=3$ and $m=4$ the system called in this paper a hub can have SA=0 for a certain value of the refractive index [92]. For instance, the quartet hub has SA=0 for $n=1.5$. Moreover, the quartet hub is known to be a relaxed design that has an axial imaging of excellent quality even at large apertures [89], [93].

8.4. Triplet

Triplet with an object in infinity

In our first example the triplet forms an image of an object at infinity and we have used the first five curvatures as variables. The image plane was placed at its paraxial position and the curvature of the last surface has been solved to keep a constant effective focal length. As in the previous example the default Code V merit function (which is based on transverse ray aberrations) was used. The resulting network, which is presented in Figure 8.4.1, consists of 18 local minima and 20 saddle points. In this network, each node represents a point in the five-dimensional design space and the lines connecting nodes represent optimization paths that have been generated from the saddle points. As expected, the local minima form a network where they are all linked through optimization paths generated from the saddle points. This network, which has been detected in five dimensions, can be visualized in a two-dimensional graph. This allows us to examine the relationship between the various minima independently of the dimensionality of the MF space.

The network represented in Figure 8.4.1 has an excess of saddle points as only 17 saddle points are required to form a network where all 18 minima are connected. For example, the saddle point having a MF value of 54390 can be removed without disconnecting the network. By removing all such superfluous saddle points, we obtain the "essential" topography of the MF space as presented in Figure 8.4.2. The acyclic network thus formed shows the minimum barriers in MF value that needs to be overcome in order to move from one minimum to another one. From Figure 8.4.2 we can also derive a binary-tree representation where the splitting of the equimagnitude surfaces is represented (see Figure 8.4.3). This binary tree can be used to visualize how the equimagnitude surfaces split as a function of decreasing MF values. Such a representation is less sensitive to the type of local optimization algorithm used to generate the paths from the saddle points towards the minima.

Even in the case of a constrained MF space, we can apply our algorithm to detect the network of minima. For instance, we have added an additional constraint such that the curvature of the fifth surface is larger than zero. The corresponding network of minima is presented in Figure 8.4.4. This network shows a remarkable similarity with the network presented in Figure 8.4.2. Those parts of the network for which the constraints have not been violated are identical. However, saddle points and minima

Optical system networks

are now also found on the constraint while other parts of the unconstrained network do not exist anymore.
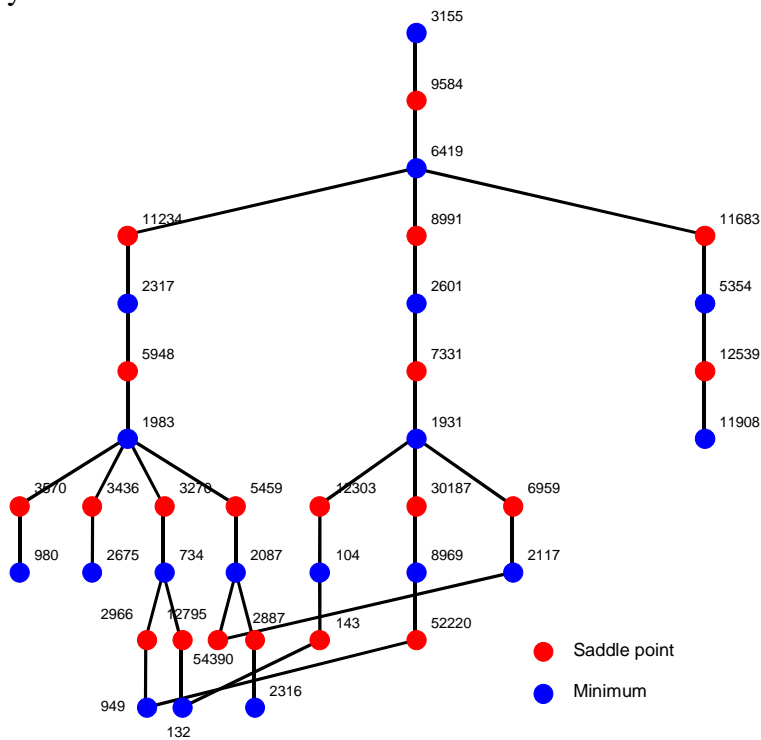
Figure 8.4.1 Network of the global search corresponding to the Cooke triplet. The nodes represent optical systems corresponding to the saddle points and local minima. Nodes are connected through optimization paths generated from the saddle points.
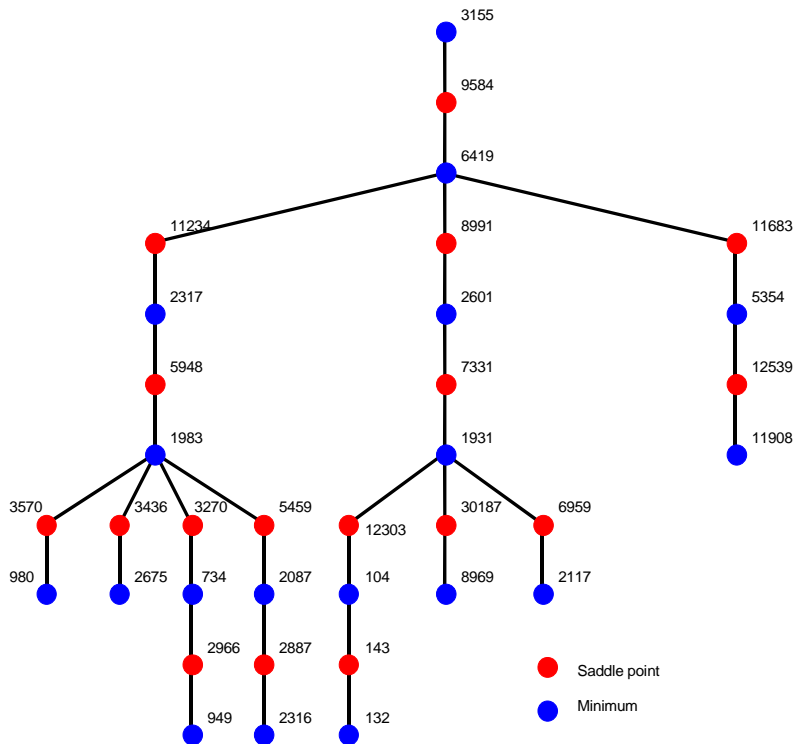
Figure 8.4.2 Essential network of the global search corresponding to the Cooke triplet. The minimum barrier in merit function value that needs to be overcome in order to move from one minimum to another one is determined by the saddle point with highest MF value that separates these minima.

Optical system networks
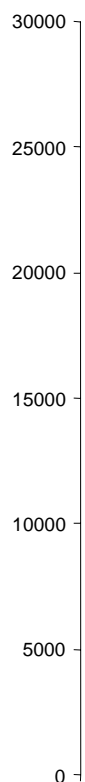
Figure 8.4.3 Tree structure of the global search corresponding to the Cooke triplet. The splitting of the equimagnitude surfaces is represented as a function of the merit function value. The branching points are the saddle points and the endpoints are the local minima
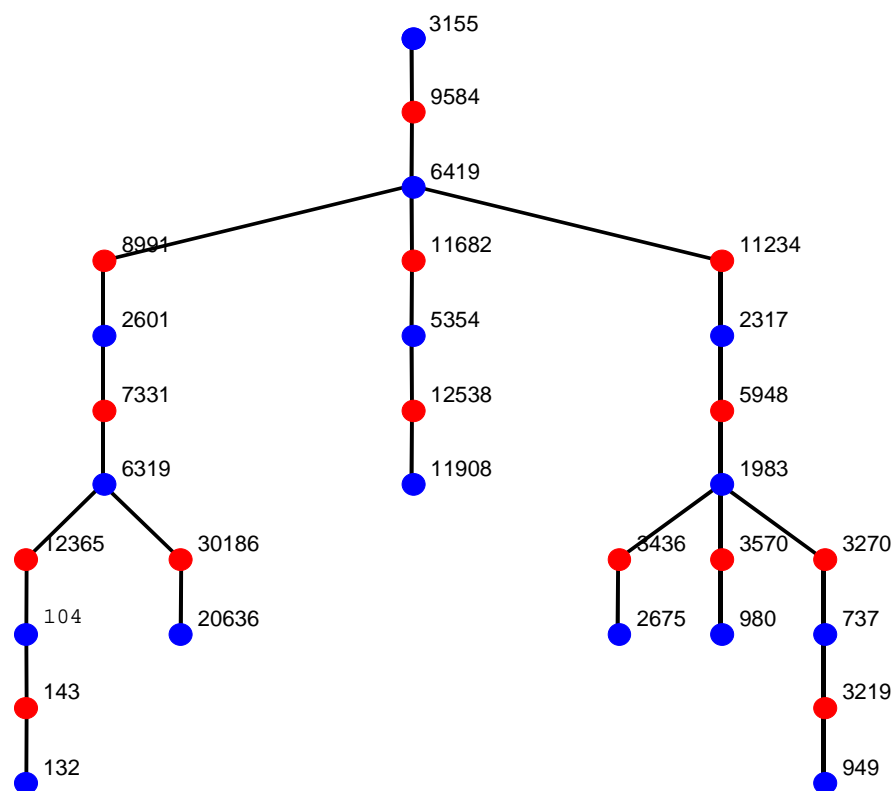
Figure 8.4.4 Essential network of the global search corresponding to the constrained Cooke triplet. Large parts of the network are identical to the unconstrained network. (Note however, that the branches are drawn in a different order.)

Our experience has shown that the searches into the direction of the eigenvector with smallest eigenvalue find slightly less than 50% of the saddle points. To find all saddle points, the eigenvectors with higher eigenvalues are also important. In the searches for the unconstrained Cooke triplet, the different eigenvalues of the Hessian matrix at a minimum can differ significantly. For one of the minima, the highest eigenvalue was approximately 25,000 times higher than the lowest eigenvalue of the Hessian matrix. Mostly, the ratio between the highest and lowest eigenvalue at a minimum ranges between 500 and 6000 so that the initialization of the algorithm for saddle point detection is extremely important in optics.

Symmetric Triplet

For testing the reliability of our network detection, in this example we have chosen the specifications (distances between surfaces, glass types) to be rigorously symmetric with respect to the aperture stop. For this purpose, the central lens has been split by a fictitious stop surface. The image plane was placed at its paraxial position and the position of the object plane was controlled such that the transverse magnification was kept equal to -1. Because of an additional equality constraint (the distance between object and image was also kept constant) the search space was effectively 5-dimensional. The merit function used was the default merit function of CODE V.

In the case of a symmetric triplet where the optimization variables were the six curvatures of the surfaces, we have found 23 SPMI1 (drawn within thin-line boxes in Figure 8.4.5). By following the downward paths of local optimization started at these points, we have obtained 19 local minima (thick-line boxes). The best two local minima, m_1 and m_2, have the well-known shape of the Cooke triplet. The first 17 of our local minima are identical with the 17 local minima listed in the output of Global Synthesis, the global optimization algorithm of CODE V. Interestingly, the saddle-point configurations s_{i-j} can be viewed as intermediate stages in a continuous transformation of the local minimum m_i into the minimum m_j.

As expected, the detected network show in Figure 8.4.5 is almost perfectly symmetric. With one exception, the saddle point s_{8-5}, the configurations in Figure 8.4.5 are either symmetric with respect to the stop (m_9, s_{1-2}, and s_{19-18}) or they have mirror images. For clarity, the pairs in which one configuration is (almost) the mirror image of the other have been grouped together in the same box. Moreover, with the exception of the two dashed links in the lower right part of Figure 8.4.5, the detected links display the same symmetry: if a saddle point links two minima, then the mirror of the saddle point will link the mirrors of the same minima. The minor deviations of the network from perfect symmetry are not surprising since the aberrations that affect the ray tracing results perturb to some extend the symmetry between object and image.

The best two local minima of this search, m_1 and m_2, have the well-known shape of the Cooke triplet. Interestingly, for a numerical aperture of 0.055 (the value of this search), both are slightly asymmetric and form a mirror pair, whereas the saddle point s_{1-2} between them is symmetric. However, if we increase the numerical aperture, beyond the value of 0.075 these two minima will merge into a single symmetric one.

Although we cannot be certain that the present algorithm has detected the entire network, the symmetry detected as expected increases our confidence in the potential of our network idea.
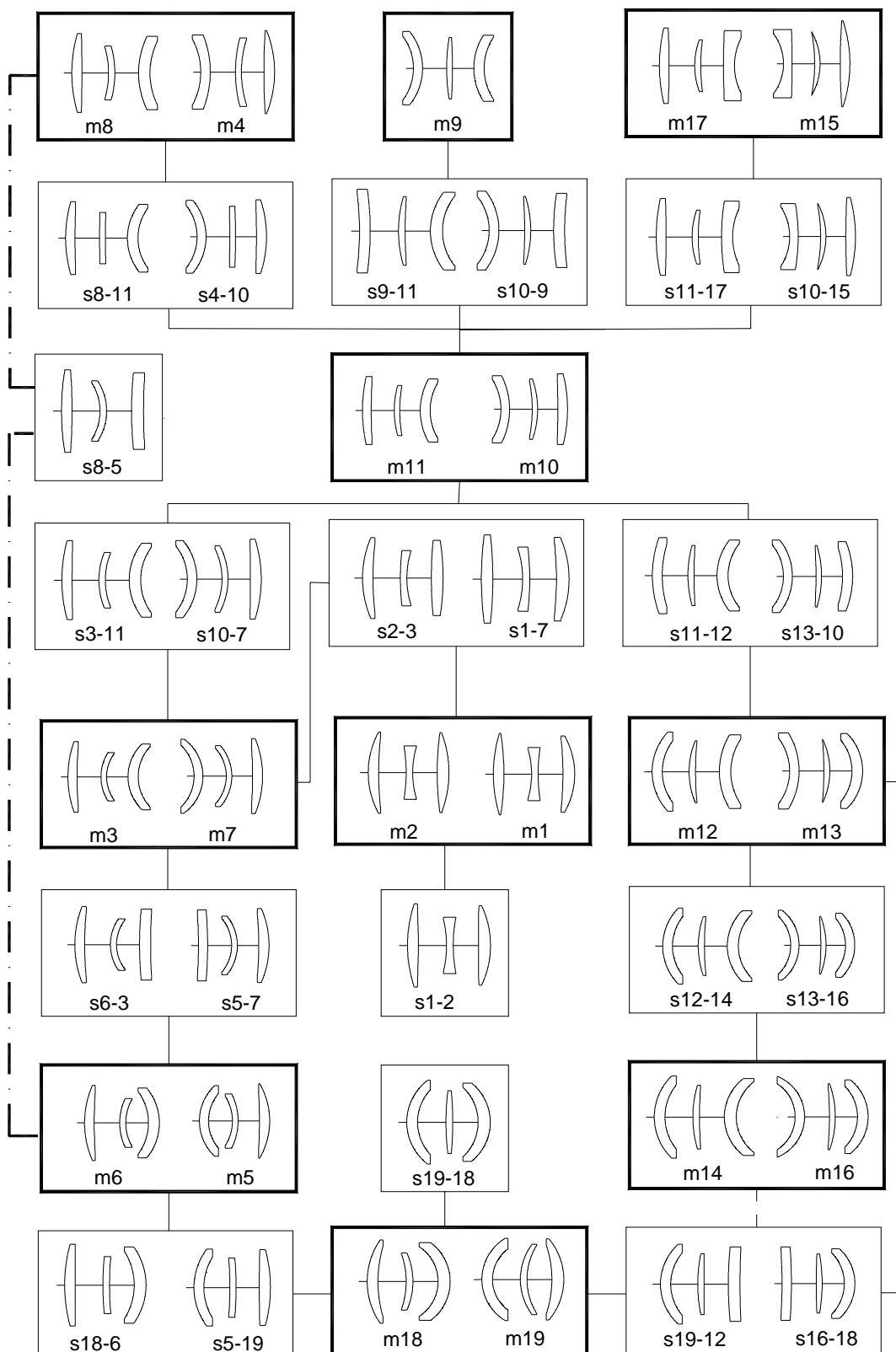
Figure 8.4.5 Network of the global search corresponding to the symmetric Cooke triplet

8.5. Double Gauss

The next example is the network of the Double Gauss objective (see Figure 8.5.1).
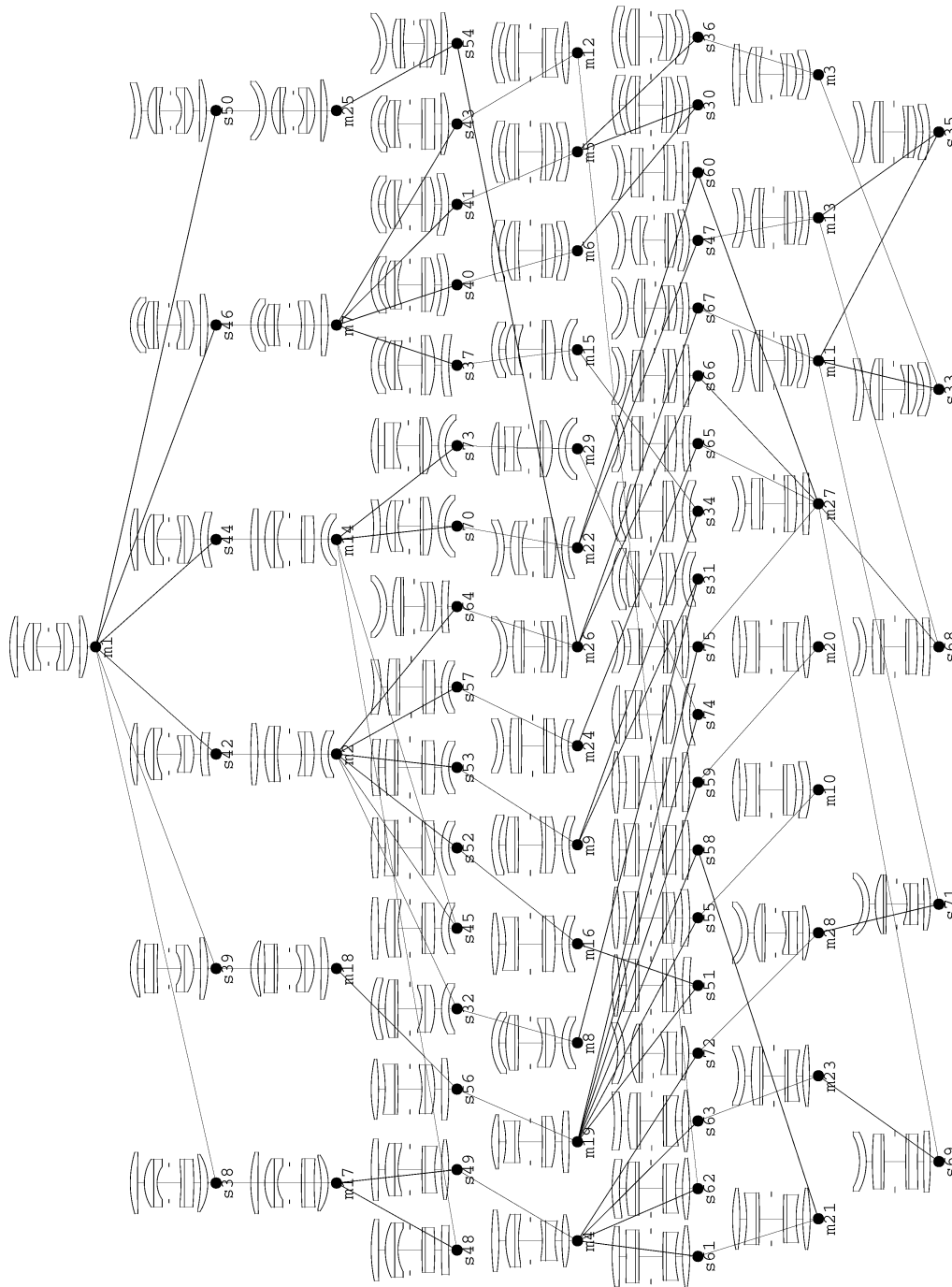
Figure 8.5.1 The network of local minima corresponding to a Double Gauss global search, as detected by the program NETMIN. The optimization variables are curvatures of the eight outer surfaces, and the merit function is the default error function of CODE V. (The system specifications are reduction ratio of 1, entrance pupil diameter 50 mm, field of view 28 degrees, working wavelength range 656…486 nm).

Again we take the symmetric design with regard to the stop plane. In this system we have eight free optimization parameters (the curvatures of the surfaces on each air-glass separation). As the parameters of the object distance (it was used to keep the reduction ratio constant) and the last thickness (the paraxial image distance solve was

put on it) were also used, the total track constraint in order to avoid "long" solutions was also used. The global search with NETMIN detected 29 local minima and 46 saddle points.

8.6.   DUV and EUV lithographic objectives

It is obvious that a further increase of the number of optimization parameters leads to larger and larger networks. For complex systems with many parameters exploring the entire network may be very time consuming because even the local optimization of these systems takes a lot of time even on a modern PC. This issue requires a new strategy based on network analysis for the choice of search directions leading to the better solutions. This strategy is a subject for further research.

Because of their complexity it is not easy to find even parts of the network of DUV objectives. For patented designs, the aberration correction is so well performed that already a small change of the system parameters often results in a shift to the basin of attraction of a neighboring local minimum. However, for these small parameter changes visually the neighboring local minima seem to be identical. For demonstration purposes we took an objective shown in Figure 4.4.2 (the specifications of this system were taken from Ref. [35]). We reduce the number of free parameters to five (the five curvatures of the lens group enlarged in Figure 8.6.1). The part of network of this objective discovered with the NETMIN program is shown in Figure 8.6.2.

m0.00207378   s3.34615   m1.08612
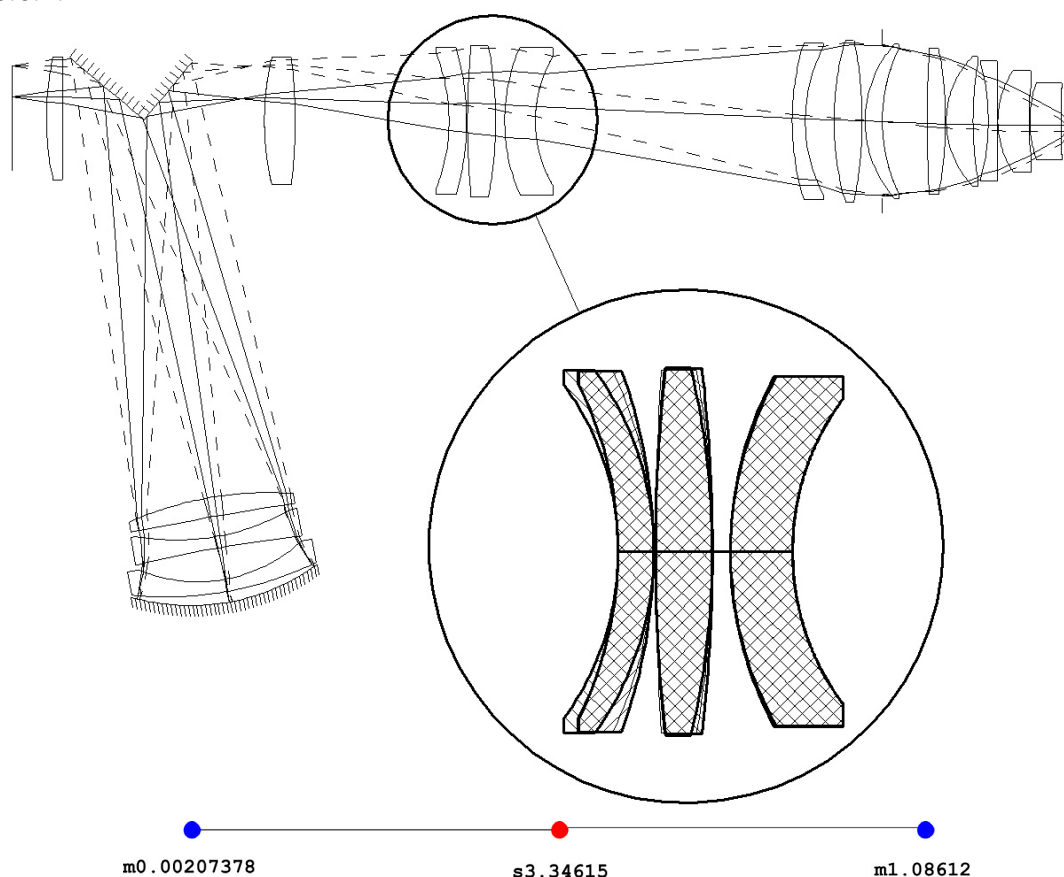
Figure 8.6.1 Three nodes of the network of DUV lithographic objective. In the enlarged picture two local minima hatched in crossing direction are superimposed. The contour of the system corresponding to the saddle point is shown in thin lines.

Optical system networks
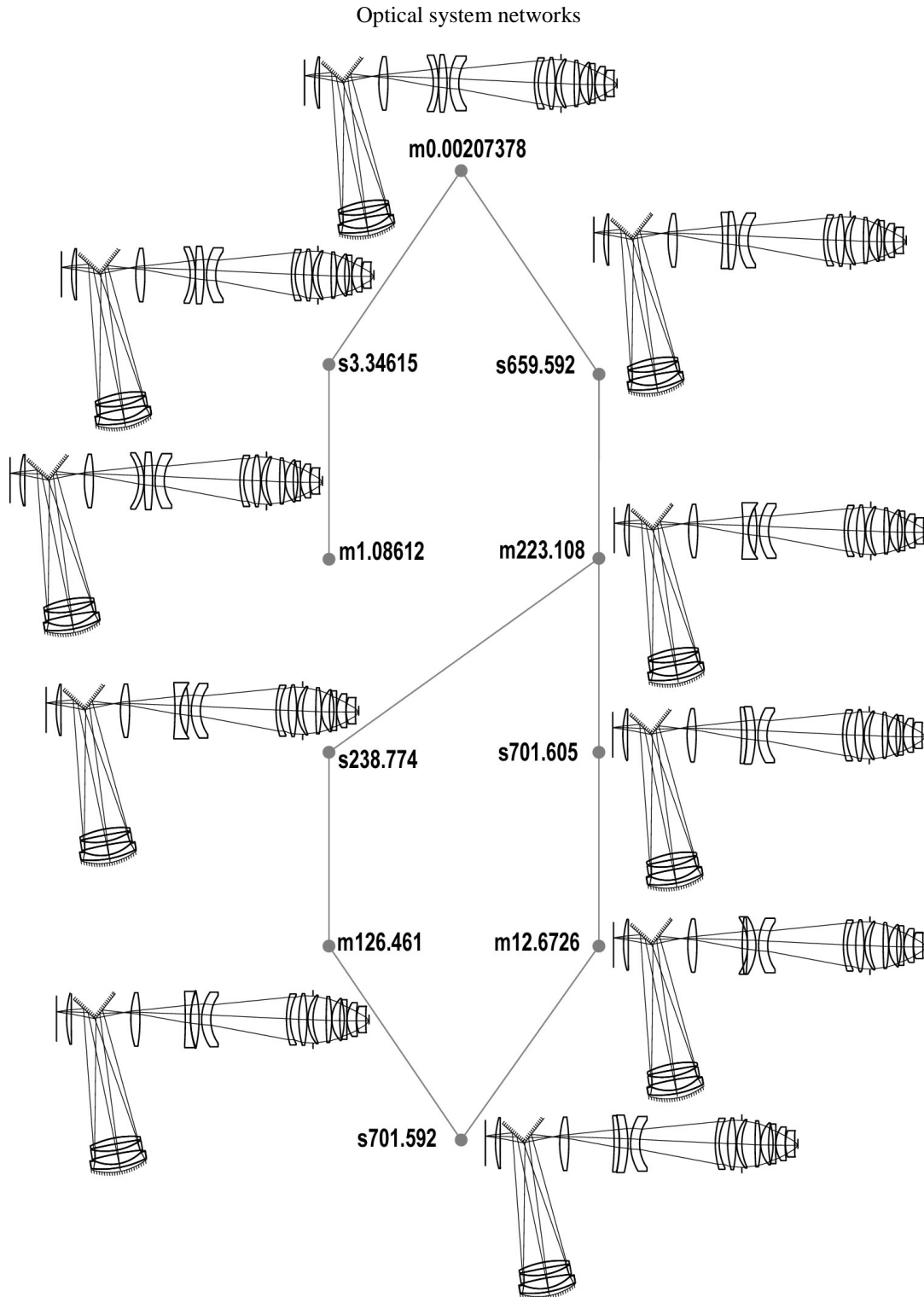
Figure 8.6.2 Part of the network of the lithographic objective. The specifications of the optical system are taken from Ref. [35].

Interestingly, it is easier to present parts of the network for EUV objectives because a number of basic configurations can be obtained already with several variables (mirrors curvatures). A part of such a network is shown in Figure 8.6.3. In order to prevent discontinuity in the MF topography, the condition of obscuration absence was temporarily omitted. (It can be seen that the unobscured local minima m6 and m3 are connected via obscured system m2.) Moreover, this network provides additional useful information. For instance, it can be seen that two neighboring obscured local minima m5 and m4 are connected via the unobscured saddle point s13. Thus, if we

implement the obscuration constraint at this saddle point it will drive us to two new unobscured local minima.
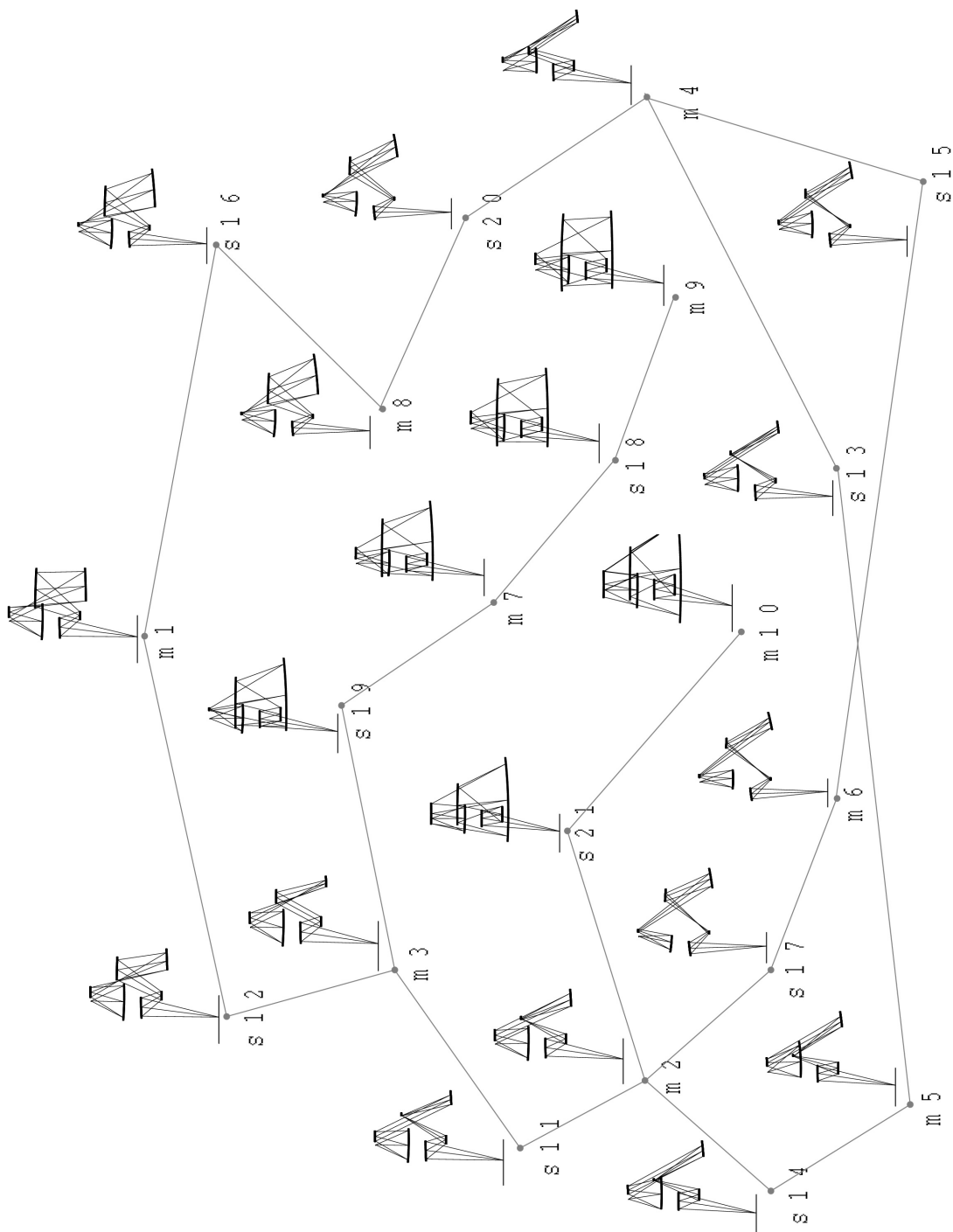
Figure 8.6.3 Part of the network of EUV lithographic objective.

In order to simplify the global optimization of complex systems, more appropriate procedures can be suggested. For instance, the complex optical systems can be split into groups (for instance objective, eyepieces, compensator etc.) and with the global optimization the number of basic solutions for each group is obtained. These solutions can be then combined in order to obtain the most promising result. Finally the local optimization for entire system has to be performed.

8.7.   Conclusions

In the last chapter we have shown and analyzed a number of networks of optical systems obtained with our global optimization method. The number of local minima and the network complexity increase with each additional optimization variable. Several presentation forms of this network were introduced as well. These representations allow a comprehensible view of the relationship between the various minima without having to deal with aspects such as the dimensionality of the optimization problem. These networks could thus be of use for the analyses of complex optical design problems.

We have also analyzed the MF topography and have shown that for certain optical systems the positions of saddle points in multidimensional space can be predicted.

Even when we did not obtain the expected result, we have often discovered some new and unexpected features of the MF topography. We believe that this new insight is part of a very valuable learning process. We do believe that optical system design would benefit very much if we had some methods that not only produce practical results, but also provide insight in the complexity of the MF landscape.

Summary and Conclusions

This thesis has been devoted to two main subjects: the compensation of birefringence induced by spatial dispersion (BISD) in Deep-UV lithographic objectives and the optimization of optical systems in general.

The motivation for this research follows from Moore's Law, according to which the number of transistors per integrated circuit grows exponentially in time and this tendency remains valid at least for the near future. This challenge requires advanced imaging capabilities for the projection optics of a photolithographic machine. One of the ways to improve the resolution of lithographic objectives is to decrease the wavelength, but in this case lithographers, among other issues, should find an appropriate lens material, because in the currently used deep UV range, only a few media are sufficiently transparent. Cubic crystals such as CaF_2 are used as a companion material at the wavelength of 193 nm and fluorides are the only possible known materials which can be used for optical systems working at 157 nm. However, the use of cubic crystals is limited by their birefringence induced by spatial dispersion. In the framework of this research, a number of studies were performed in order to investigate the difficulties related with the use of cubic crystals in modern lithography and to find possible solutions for them.

First, we have studied the problem of spatial dispersion in cubic crystals and we have obtained the expressions for the eigenpolarizations and the linear birefringence value in the case of BISD in cubic crystals for an arbitrary ray direction. The angular dependence of the magnitude of the effect has been analyzed as well. Cubic crystals possess seven optical axes with respect to the BISD effect. As known from the literature, considering the measured magnitude of the effect, the use of cubic crystals in DUV lithography causes serious problems for the resolution of the projection lens.

The resolution issue was further investigated by modeling the BISD effect in optical design software, which allowed us to estimate the detrimental effect on optical resolution. The image deterioration is brought on mainly by the phase retardation caused by BISD. This effect was computed on the basis of polarization ray tracing with the help of Jones matrices. It was shown that the magnitude of the phase retardation is large enough to cause serious problems for obtaining the required resolution. We have also examined the possibilities for BISD analysis offered by modern software tools and we found that, for the estimation of the retardation value, the standard deviation of the retardation over the pupil is useful. The second BISD consequence − the ray bifurcation and deviation − was briefly discussed as well.

The phase retardation effect in deep UV lithography can be compensated. We have discussed several approaches for the compensation of the phase retardation. All concepts assume the presence in the optical system of two groups of components contributing with almost the same distribution of the retardation magnitude but with the orthogonal retardation orientation. Several examples of DUV lithographic objectives with corrected phase retardation are presented.

Modern high-technological devices and systems require the best possible solution and implementation for the problem they have to solve. This is why global optimization is an important problem in modern optical system design. High-aperture optical systems with a resolution well within the diffraction limit such as lithographic objectives may have tens of optimization parameters, which complicates the task of optimization. Because of the existence of multiple local minima, a special optimization strategy providing additional information about the relationship between them is required.

In our research on optimization we first consider the general optimization problem and its specific application to optical system design. The most useful local and global optimization approaches were discussed and three strategies based on local optimization in order to escape from a local minimum were considered.

Nowadays, the known global optimization methods are able to find local minima only as isolated points in the parameter space without any information about the merit function topography. This is why we have focussed on the topological properties of the optimization solution space and we have demonstrated that the saddle points having Morse index of one play a special role in the merit function landscape in optical system design. We have also shown that it is possible to move from one local minimum to a neighboring one by locating a saddle point between them and we proposed a method for the saddle point detection. Once the saddle points are known, the corresponding local minima result automatically by following the downward links from the saddle points. Techniques for the saddle point detection and for the choice of the search directions were developed as well.

Moreover, by analyzing the splitting or merging of equimagnitude surfaces we have observed that the local minima of the merit function landscape in optical system design form a network. In order to perform this investigation a number of analyses and visualization tools were developed. Based on this idea, a new type of global optimization algorithm in optical system design has been proposed.

Finally, we have given several examples of optical system networks of different complexity. We have also shown by means of the example of systems of thin lenses in contact, that sometimes a simplified model can predict analytically the most important saddle points in the merit function landscape. It turned out that exploring networks of optical systems is useful even in the case of sophisticated Deep-UV and Extreme-UV lithographic objectives. In our opinion, sometimes it is easier to discover new features of optical systems by focussing on the saddle points rather than on the local minima, and the "saddle point" idea can also provide additional insight into the topography of the optimization space.

This new insight can be useful to meet the design challenges encountered in high-quality optics for lithography, microscopy and space applications. We do believe that asking new questions is essential for improving our understanding of optical design.

Nederlandse Samenvatting en Conclusies

Dit proefschrift is gewijd aan twee hoofdonderwerpen: de compensatie van dubbele breking veroorzaakt door ruimtelijke dispersie (BISD) in de Deep-UV lithografische objectieven en het optimaliseren van optische systemen in het algemeen.

De drijfkracht voor dit onderzoek vloeit voort uit de Wet van Moore. Volgens deze wet groeit het aantal transistoren per geïntegreerde schakeling exponentieel in de tijd en deze neiging blijft ten minste tot in de nabije toekomst geldig. Deze groei van transistoren vereist geavanceerde afbeeldingskwaliteit voor het optisch system dat nodig is in de fotolithografische machine. Een van de manieren om de resolutie van lithografische objectieven te verbeteren is het verkleinen van de golflengte. In dit geval zouden lithografen naast andere zaken ook een geschikt lensmateriaal moeten vinden, omdat in het Deep-UV (DUV) bereik dat tegenwoordig wordt gebruikt, slechts een aantal media voldoende doorzichtig zijn. Kubische kristallen zoals CaF_2 worden gebruikt als een hulpmateriaal bij een golflengte van 193 nm en fluoriden zijn de enig mogelijke bekende materialen die gebruikt kunnen worden voor optische systemen die werken bij een golflengte van 157 nm. Het gebruik van kubische kristallen is echter begrensd door hun dubbele breking veroorzaakt door ruimtelijke dispersie. In het kader van dit onderzoek zijn een aantal studies uitgevoerd om de moeilijkheden te onderzoeken die gerelateerd zijn aan het gebruik van kubische kristallen in de moderne lithografie en om mogelijke oplossingen voor deze moeilijkheden te vinden.

Ten eerste hebben we het probleem van ruimtelijke dispersie in kubische kristallen bestudeerd en hebben we de uitdrukkingen voor de eigenpolarisaties en de lineaire dubbele brekingswaarde voor een willekeurige straalrichting verkregen in het geval van BISD in kubische kristallen. Ook de hoekafhankelijkheid van de grootte van het effect is geanalyseerd. Kubische kristallen hebben zeven optische assen met betrekking tot het BISD effect. Het is algemeen bekend dat als we de gemeten grootte van het effect in beschouwing nemen, het gebruik van kubische kristallen in DUV lithografie ernstige problemen voor de resolutie van de projectielens veroorzaakt.

De resolutiekwestie werd verder onderzocht door het BISD effect te modelleren met behulp van ontwerpsoftware voor optische systemen, die het ons mogelijk maakte om het nadelige effect op de optische resolutie te bepalen. De beeldverslechtering wordt vooral veroorzaakt door de fasevertraging ten gevolge van het BISD effect. Dit effect werd berekend op basis van polarisatiestraaldoorrekening met behulp van Jones matrices. Getoond is dat de fasevertraging groot genoeg is om ernstige problemen te veroorzaken in het verkrijgen van de vereiste resolutie. We hebben ook de mogelijkheden voor BISD analyse onderzocht die door moderne softwaregereedschappen worden aangeboden en we vonden dat, voor de bepaling van de vertragingswaarde, de standaarddeviatie van de vertraging over de pupil geschikt is. Het tweede BISD gevolg – de straalopsplitsing en straalafwijking – werd eveneens kort besproken.

Het fasevertragingseffect in DUV lithografie kan gecompenseerd worden. We hebben een aantal methodes voor het compenseren van de fasevertraging voorgesteld. Alle ideeën veronderstellen de aanwezigheid van twee groepen componenten in het optische systeem die bijdragen met bijna dezelfde spreiding van de vertragingsgrootte maar met de loodrechte oriëntatie van de vertraging. Een aantal voorbeelden van DUV lithografische objectieven met gecorrigeerde fasevertraging werden getoond.

Moderne en technologisch geavanceerde apparaten en systemen vereisen de best mogelijke oplossing en implementatie voor het probleem dat ze op moeten lossen. Daarom is globale optimalisering een belangrijk probleem in het hedendaagse optische systeemontwerp. Optische systemen met een grote apertuur en met een resolutie ruim binnen de diffractielimiet, zoals lithografische objectieven, hebben tientallen optimaliseringsvariabelen die het optimaliseren zeer gecompliceerd maken. Omdat er meerdere lokale minima bestaan, is er een speciale optimaliseringsstrategie nodig die aanvullende informatie geeft over de relatie tussen de verschillende minima. In ons onderzoek naar optimalisering beschouwden we eerst het algemene optimaliseringsprobleem en zijn specifieke toepassing op optisch systeemontwerp. De meest bruikbare lokale en globale optimaliseringsmethodes werden besproken en er werden drie strategieën beschouwd die gebaseerd waren op lokale optimalisering om te ontkomen aan een lokaal minimum.

Tegenwoordig zijn de bekende globale optimaliseringsmethodes in staat om een lokaal minimum slechts als geïsoleerd punt in de parameterruimte te vinden, zonder enige informatie over de foutfunctietopologie. Daarom hebben we gekeken naar de topologische eigenschappen van de oplossingsruimte van een optimaliseringsprobleem en hebben we laten zien dat er een speciale rol is weggelegd voor zadelpunten met een Morse index gelijk aan 1 in het foutfunctielandschap van een optisch systeemontwerp. We hebben tevens aangetoond dat het mogelijk is om van een lokaal minimum naar het naburige lokale minimum te gaan door de plaats te bepalen van een zadelpunt dat tussen hen in ligt en we hebben een methode voorgesteld voor de detectie van deze zadelpunten. Als de zadelpunten eenmaal bekend zijn, volgen de overeenkomstige lokale minima automatisch door het volgen van de naar beneden gaande verbindingen vanaf de zadelpunten. Technieken voor de zadelpuntdetectie en voor de keuze van de zoekrichtingen werden eveneens ontwikkeld.

Bovendien hebben we, door het splitsen of samenkomen van contouren met dezelfde hoogte, waargenomen dat de lokale minima in het foutfunctielandschap van een optisch systeemontwerp een netwerk vormen. Om het onderzoek uit te voeren, werden er een aantal analyse- en visualiseringsgereedschappen ontwikkeld. Op basis van dit idee hebben we een nieuw soort algoritme voor globale optimalisering in optisch systeemontwerp voorgesteld.

Tot slot hebben we een aantal voorbeelden gegeven van optische systeemnetwerken van verschillende complexiteit. Tevens hebben we, door middel van het voorbeeld van systemen met dunne lenzen in contact, laten zien dat een vereenvoudigd model analytisch de meest belangrijke zadelpunten in het foutfunctielandschap kan voorspellen. Het werd duidelijk dat het verkennen van netwerken van optische systemen nuttig is, zelfs in het geval van ingewikkelde DUV en Extreme-UV lithografische objectieven. Naar onze mening is het soms gemakkelijker om nieuwe kenmerken van optische systemen te ontdekken door alleen de zadelpunten te beschouwen in plaats van de lokale minima. Ook kan het "zadelpunt idee" aanvullend inzicht verschaffen in de topografie van de optimaliseringsruimte.

Dit nieuwe inzicht kan nuttig zijn om de ontwerpuitdagingen aan te kunnen pakken die men tegenkomt in de hoge kwaliteitsoptica voor lithografie, in microscopen en in de toepassingen voor astronomie en ruimte-optica. Wij geloven dat het stellen van nieuwe vragen essentieel is om ons inzicht in optisch systeemontwerp te verbeteren.

References

[1] L. Hoddeson and M. Riordan, *Crystal Fire: The Invention of the Transistor and the Birth of the Information Age*, (W. W. Norton & Company, USA Edition, 1998).

[2] T. Reid, *The Chip: How Two Americans Invented the Microchip and Launched a Revolution*, (Random House Trade Paperbacks, USA Edition, 2001).

[3] http://www.intel.com/education/makingchips/index.htm.

[4] http://public.itrs.net.

[5] *Handbook of optics*, Vol. 1. Fundamentals, techniques, and design (McGraw-Hill, New York, 1995).

[6] G. Chiu and J. Shaw, "Optical lithography: Introduction", *IBM J. Res. Dev.* **41**(1/2) (1997).

[7] B. Smith, A. Bourov, H. Kang, F. Cropanese, Y. Fan, N. Lafferty, and L. Zavyalova, "Water immersion optical lithography at 193 nm", *J. Microlithogr., Microfabr., Microsyst.* **3**(1), 44-51 (2004).

[8] R. Singh, A. Rosenbluth, G. Chiu, and J. Wilczynski, "High-numerical-aperture optical designs", *IBM J. Res. Dev.* **41**(1/2) (1997).

[9] E. Glatzel, "New lenses for microlithography", *Proc. SPIE Int. Soc. Opt. Eng.* **0237**, 310-320 (1980).

[10] W. Ulrich, H. Rostalski, R. Hudyma, "Development of dioptric projection lenses for deep ultraviolet lithography at Carl Zeiss", *J. Microlithogr., Microfabr., Microsyst.* **3**(1), 87-96 (2004).

[11] A. Bates, M. Rothschild, T. Bloomstein, T. Fedynyshyn, R. Kunz, V. Liberman, and M. Switkes, "Review of technology for 157-nm lithography", *IBM J. Res. Dev.* **45**(5) (2001).

[12] H. Lorentz, *Collected papers,* Vol. 2-3 (Nijhoff, Den Haag, 1936).

[13] K. Hellwege, *Z. Physik* **129**, 626 (1951).

[14] V. Ginzburg, *Sov. Phys. JETR* **7**, 1096 (1958).

[15] V. Agranovich and V. Ginzburg, *Crystal Optics with Spatial Dispersion, and Excitons* (Springer-Verlag, Berlin, 1984).

[16] J. Burnett, Z. Levine, and E. Shirley, "Intrinsic birefringence in calcium fluoride and barium fluoride", *Phys. Review B* **64**, 241102 (2000).

[17] J. H. Burnett, Z. H. Levine, E. L. Shirley, and J. H. Bruning, "Symmetry of spatial-dispersion-induced birefringence and its implications for CaF_2 ultraviolet optics", *J. Microlithogr., Microfabr., Microsyst.* **1**, 213-224 (2002).

[18] D. Stockbarger, "Artificial fluorite", *J. Opt. Soc. Am.* **39**, 731 (1949).

[19] J. Hahn, G. Grabosch, L. Parthier, and K. Knapp, "Critical enabling properties of CaF_2 lens blanks for state-of-the-art lithography tools", *Proc. SPIE Int. Soc. Opt. Eng.* **5040**, 734-741 (2003).

[20] D. Golini, M. DeMarco, W. Kordonski, and J. Bruning, "Magnetorheological finishing produces calcium fluoride lenses for 157-nm lithography, overcoming crystalline anisotropy and producing nanometer-scale surface figure", *Laser Focus World* **37**(7) (2001).

[21] L. Landau, *Electrodynamics of continuous media* (Pergamon Press, Oxford, 1984).

[22] J. Nye, *Physical properties of crystals* (Clarendon Press, Oxford, 1985).

[23] R. Courant, *Methods of mathematical physics*, Vol. 1 (Interscience, New York, 1989).

[24]   A. Rosenbluth, G. Gallatin, N. Seong, O. Dittmann, and M. Totzeck, "Image Formation In A Lens With Spatial Dispersion (Intrinsic Birefringence)" presented at *4th International Symposium on 157 nm Lithography*, Yokohama, Japan (2003).

[25]   *Handbook of optics*, Vol. 2: Devices, measurement, and properties (McGraw-Hill, New York, 1995).

[26]   M. Born and E. Wolf, *Principles of optics* (Cambridge University Press, Cambridge, 1999).

[27]   R. Azzam and N. Bashara, *Ellipsometry and Polarized Light* (North-Holland Publishing Company, Amsterdam, 1977).

[28]   P. Lancaster and M. Tismenetsky, *The Theory of Matrises* (Academic Press, Orlando, 1985).

[29]   Shih-Yau Lu and Russell A. Chipman, "Homogeneous and inhomogeneous Jones matrices", *J. Opt. Soc. Am. A* **11**(2), 766-772 (1994).

[30]   Yasuyuki Unno, "Influence of Birefringence on the Image Formation of High-Resolution Projection Optics", *Appl. Opt.* **39**(19), 3243-3252 (2000).

[31]   *Code V 9.5 Reference Manual* (Optical Research Associates, August 2004).

[32]   B. Richards and E. Wolf, "Electromagnetic diffraction in optical systems. II. Structure of the image field in an aplanatic system", *Proc. R. Soc. London Ser. A* **253**, 358-379 (1959).

[33]   S. Stallinga, "Strehl Ratio for focusing into biaxially birefrigent media", *J. Opt. Soc. Am. A* **21**(12), 2406-2413 (2004).

[34]   Personal communication with Brice Irving (Optical Research Associates, December 2004).

[35]   R. Bunau, C. Hebmd-Sollner, H. Holderer *U.S. Patent US6784977* (2004).

[36]   W. Singer, M. Totzeck, H. Gross, *Handbook of Optical Systems*, Vol. 2: Physical Image Formation (John Wiley & Sons, New-York, 2005).

[37]   D. Shafer, A. Epple, W. Ulrich, *WO Patent 2003/050587* A3 (2003).

[38]   Y. Unno, "Polarization analyses of aerialimages produced by an optical lithography system", *Appl. Opt.* **37**(10), 1895-1902 (1998).

[39]   Y. Unno and A. Suzuki, "Analyses of imaging performance degradation caused by birefringence residual in lens materials", *J. Microlithogr., Microfabr., Microsyst.* **1**, 49-57 (2002).

[40]   N. Shiraishi, S. Owa, Y. Omura, T. Ozawa, and I. Tanaka, "Current status of Nikon's investigation on CaF$_2$ intrinsic birefringence," in *Calcium Fluoride Birefringence Workshop*, R. Harbison, ed., (International SEMATECH, Austin TX, 2001).

[41]   J. Hoffman, J. McGuire, *U.S. Patent US6885488* (2005).

[42]   J. Hoffman, J. McGuire, *U.S. Patent US6683710* (2004).

[43]   N. Shiraishi, *U.S. Patent US6775063* (2004).

[44]   N. Shiraishi, Y. Omura, *U.S. Patent Application US2003/0011893A1* (2003).

[45]   M. Gerhard, D. Krähmer, *German Patent DE 10133841A1* (2003).

[46]   T. Takahashi, J. Nishikawa, Y. Omura, *U.S. Patent US6757051* (2004).

[47]   D. Allan, J. Webb, J. Bruning, *U.S. Patent US6785051* (2004).

[48]   K. Doyle, J. Hoffman, V. Genberg, and G. Michels, "Stress birefringence modeling for lens design and photonics", *Proc. SPIE Int. Soc. Opt. Eng.* **4832**, 436-447 (2002).

[49]   K. Doyle, V. Genberg, and G. Michels, "Numerical methods to compute optical errors due to stress birefringence", *Proc. SPIE Int. Soc. Opt. Eng.* **4769**, 34-42 (2002).

[50]   J. Hahn, G. Grabosch, L. Parthier, and K. Knapp, "Critical enabling properties of CaF$_2$ lens blanks for state-of-the-art lithography tools", *Proc. SPIE Int. Soc. Opt. Eng.* **5040**, 734-741 (2003).

[51]   J. Webb, J. Bruning *U.S. Patent Application US2003/0168597A1* (2003).

[52]   http://www.e-optimization.com.

[53]   http://www.optimization-online.org.

[54]   R. Fletcher, *Practical methods of optimization* (Chichester, Wiley, 1987).

[55]   *Handbook of applied optimization*, (Oxford, University Press, 2002).

[56]   H. Kuhn and A. Tucker, "Nonlinear Programming", *Proc. Second Berkeley Symposium on Mathematical Statistics and Probability*, ed. J. Neyman, 481-492 (University of California Press, Berkeley, 1951).

[57]   W. Press, S. Teukolsky, W. Vetterling, B. Flannery, *Numerical Recipes in C++: The Art of Scientific Computing* (Cambridge University Press, Cambridge, 2002).

[58]   http://mathworld.wolfram.com/NewtonsMethod.html.

[59]   J. Shewchuck, *An introduction to the conjugate gradient method without the agonizing pain,* Technical Report CMU-CS-94-125, (School of Computer Science, Carnegie Mellon University, 1994), also available at http://www-2.cs.cmu.edu/~jrs/jrspapers.html.

[60]   P. Gill, W. Murray, and M. Wright, "The Levenberg-Marquardt Method" in *Practical Optimization*, 136-137 (Academic Press, London, 1981).

[61]   http://mathworld.wolfram.com/GlobalOptimization.html.

[62]   J. Pintér, *Global optimization in action* (Dordrecht, Kluwer Academic, 1996).

[63]   M. Kidger, *Intermediate Optical Design* (SPIE Press, Vol. PM92, 2004).

[64]   F. Bociort, "Optical System Optimization" in *Encyclopedia of Optical Engineering*, 1843-1850 (Marcel Dekker, New York, 2003)

[65]   T. Kuper, T. Harris, "Global optimization for lens design - an emerging technology", *Proc. SPIE Int. Soc. Opt. Eng.* **1780**, 14-28 (1992).

[66]   S. Weller, "Simulated Annealing: What good is it?", *Proc. SPIE Int. Soc. Opt. Eng.* **0818** (1987).

[67]   G. Forbes, A. W. Jones, "Towards global optimization with adaptive simulated annealing", *Proc. SPIE Int. Soc. Opt. Eng.* **1354**, 144-151 (1991).

[68]   E. Betensky, "Postmodern lens design", Opt. Eng. **32**(8), 1750-1756 (1993).

[69]   K. Moore, "Algorithm for global optimization of optical systems based on genetic competition", *Proc. SPIE Int. Soc. Opt. Eng.* **3780**, 40-47 (1999).

[70]   J. Beaulieu, C. Gagné, and M. Parizeau, "Lens System Design and Re-Engineering with Evolutionary Algorithms", *Proc. of the Genetic and Evolutionary Computing Conference (GECCO)*, 155-162 (2002).

[71]   http://www.lambdares.com/products/oslo/index.phtml.

[72]   M. Bal, F. Bociort, and J. Braat, "Analysis, Search, and Classification for Reflective Ring-Field Projection Systems", *App. Opt.* **42**(13), 2301-2311 (2003).

[73]   M. Isshiki, H. Ono, K. Hiraga, J. Ishikawa, S. Nakadate, "Lens design: Global optimization with Escape Function", *Opt. Rev.* **6**, 463-470 (1995).

[74]   G. Treccani, L. Trabattoni, and G. P. Szego, "A numerical method for the isolation of minima", in *Minimisation Algorithms, Mathematical Theories and Computer Results*, G. P. Szego (ed.), 239-255 (Academic Press, 1972).

[75]   C. Corles, "The use of regions of attraction to identify global minima", in *Towards global optimisation*, L. Dixon and G. Szego (eds.), 55-95 (North-Holland/Elsevier, Amsterdam, 1975).

[76]   J. Hart, "Morse Theory for Implicit Surface Modeling", in *Mathematical Visualization*, H.-C. Hege and K. Polthier (eds.), 257 (Springer-Verlag, Berlin, 1998).

[77]   G. Barkema, N. Mousseau, "Event-Based Relaxation of Continuous Disordered Systems", *Phys. Rev. Lett.* **77**, 4358 (1996).

[78]   N. Mousseau, G. Barkema, "Travelling through potential energy landscapes of disordered materials: The activation-relaxation technique", *Phys. Rev. E* **57**, 2419 (1998).

[79]   G. Wei, N. Mousseau, P. Derreumaux, "Exploring the energy landscape of proteins: A characterization of the activation relaxation technique", *J. Chem. Phys.* **117**, 11379 (2002).

[80]   D. Wales, "Rearrangements of 55 atom Lennard-Jones and $(C_{60})_{55}$ Clusters", *J. Chem. Phys.* **101**, 3750 (1994).

[81]   J. Doyle, D. Wales, "Surveying a potential energy surface by eigenvector-following", *Z. Phys. D* **40**, 194 (1997).

[82]   http://www.vni.com/products/imsl/fortran/overview.html.

[83]   D. Sturlesi, D. O'Shea, "Global view of optical design space", *Opt. Eng.* **30**(2), 207-217 (1991).

[84]   W. Welford, *Aberrations of optical systems* (Hilger, Bristol, 1986).

[85]   G. Slyusarev, *Aberration and optical design theory* (Hilger, Bristol, 1984)

[86]   E. Weisstein, "Monkey Saddle" in *CRC concise encyclopedia of mathematics*, CRC Press, Boca Raton, (1999), (also available at Wolfram Web Resource http://mathworld.wolfram.com/MonkeySaddle.html).

[87]   http://www.zemax.com.

[88]   http://wwwoptica.tn.tudelft.nl/users/bociort/doublet_network.html. (For more significant merit function changes, the two systems for a given saddle point must be farther away from the saddle point itself, so that these systems enter more deeply in the basins of attraction of the corresponding local minima.)

[89]   D. Shafer, "Optical Design and the Relaxation Response", *Proc. SPIE Int. Soc. Opt. Eng.* **0766**, 2-9 (1987).

[90]   W. Smith, *Modern optical engineering: the design of optical systems* (McGraw-Hill, New York, 2000).

[91]   M. Kidger, "Techniques for Handling Difficult Lens Design Problems 1. The 'Local Minimum' Problem", *Proc. SPIE Int. Soc. Opt. Eng.* **0766**, 27-31 (1987).

[92]   G. Fulcher, "Telescope objective without spherical aberration for large apertures, consisting of four crown glass lenses", *J. Opt. Soc. Am.* **37**(1), 47-53 (1947).

[93]   R. Fisher, "Spherical Aberration - some fascinating observations", *Proc. SPIE Int. Soc. Opt. Eng.* **0766**, 53-60 (1987).

Acknowledgments

There are a lot of people and companies that I would like to thank for what they have done for me.

First of all I would like to mention my promoter Prof. Joseph Braat who gave me this opportunity to study and work in the Optics Research Group at the TU Delft, where I have learned a lot. I enjoyed very much interesting and fruitful discussions with him. Dear Joseph, thank you for your incredible patience and for investing enormous efforts and time to help me with writing and correcting this thesis.

A special word of gratitude goes to Dr. Florian Bociort for long hours spent with me, for directing and guiding me through the entire project. He is the one who coached me on the daily basis and his ideas and valuable pieces of advice in many areas were of great importance for me. It was he, who helped me from the very beginning of my work at TU Delft to the very end of it. Dear Florian, your help can be hardly overestimated!

My deepest thanks to all former and current members of the Optics Research Group, especially, to Eco van Driel for his assistance with programming, Oana Marinescu for her help with optimization of EUV systems, and Maarten van Turnhout for his aid with mathematical derivations and Dutch language. Others contributed to my work indirectly, by creating a nice and pleasant environment.

I also want to sincerely thank many people representing different organizations: Jan Mulkens, Jos Benshop, and Michael Albert at ASML, Heiko Feldmann and Michael Totzeck at Carl Zeiss SMT AG, John Burnett at NIST, Alan Rosenbluth and Gregg Gallatin at IBM's TJ Watson Research Center and Prof. Masaki Isshiki at Isshiki Optics. I have benefited from many discussions with these colleagues during a number of meetings and conferences.

I would like to acknowledge Prof. Evgeny Maksimov and Nobel Prize winner Prof. Vitaly Ginzburg for their help in the theoretical research of the spatial dispersion in cubic crystals.

This study has been initiated and fully supported by ASML and TNO and I am very grateful to them for the financial support of this research.

I appreciate help of Optical Research Associates and Lambda Research Corporation for providing an opportunity to use their software for optical modeling.

Finally, I want to say 'thank-you' to all my friends and family, particularly my beloved wife Catherine, only I know how much she did for me.

Curriculum vitae

Full name: **Alexander Georgievich Serebryakov**
           (in other spelling Alexandre Georgievich Serebriakov)
Date of birth: 08.06.1974
Place of birth: Leningrad, USSR

Education

1997 – 2000 State Institute of Fine Mechanics & Optics /Technical University/
                                                    (St. Petersburg, Russia)
Postgraduate at Department of Applied & Computational Optics
- Obtained degree: Candidate of technical sciences
- Dissertation title: Research and development of the optical systems with remote pupil

1991 – 1997 State Institute of Fine Mechanics & Optics /Technical University/
                                                    (St. Petersburg, Russia)
Student at Department of Applied & Computational Optics
- Obtained degree: Optical engineer (diploma cum laude)
- Dissertation title: An objective with flat field of view and remote entrance pupil

1981 – 1991 High School N529 (Leningrad, USSR)

Research and Development Experience

2005 –   ASML NETHERLANDS BV (Veldhoven, the Netherlands)
Sr. Application Engineer Imaging

2001 – 2005 Delft University of Technology (Delft, the Netherlands)
Ph.D. student at Optics Research Group
- Dissertation title: Optimization and analysis of Deep-UV imaging systems

1999 – 2001 Manufacturing Company AZIMUT (St. Petersburg, Russia)
Senior optical designer/Head of the optical department
- Supervising the optical department
- Optical system design
- Mechanical design
- Development of technologies & know-how
- Contacts with customers and suppliers

1997 – 1999 Vavilov State Optical Institute (St. Petersburg, Russia)
Research engineer at Department of Space Optics
- Lens design
- Research & development
- Teaching & consultations

List of publications related to this thesis

Reviewed journal publications:
- A. Serebriakov, E. Maksimov, F. Bociort, and J.J.M. Braat, "Birefringence induced by the spatial dispersion in deep UV lithography: theory and advanced compensation strategy", *Opt. Rev.* **12**(2), 140-145 (2005).
- F. Bociort, E. van Driel, and A. Serebriakov, "Networks of local minima in optical system optimization", *Opt. Lett.* **29**(2), 189-191 (2004).
- A. G. Serebryakov, F. Bociort, and J.J.M. Braat, "Spatial dispersion of crystals as a critical problem for deep UV lithography", *J. Opt. Technol.* **70**(8), 566-569 (2003).

Conference proceedings:
- A. Serebriakov, F. Bociort, and J. Braat, "Correction of the phase retardation caused by intrinsic birefringence in deep UV lithography", Proc. SPIE Int. Soc. Opt. Eng. **5754**, (2005).
- F. Bociort, A. Serebriakov, and M. van Turnhout, "Saddle points in the merit function landscape of systems of thin lenses in contact", Proc. SPIE Int. Soc. Opt. Eng. **5523**, 174-184 (2004).
- A. Serebriakov, F. Bociort, and J. Braat, "Advanced compensation strategy for the birefringence induced by spatial dispersion in deep UV lithography", Technical Digest of 2004 ICO Int. Conf. "Optics&Photonics in Technology Frontier", Tokyo (Japan), 23-24 (2004).
- A. Serebriakov and F. Bociort, "Connected local minima in optical system design", Technical Digest of 2004 ICO Int. Conf. "Optics&Photonics in Technology Frontier", Tokyo (Japan), 21-22 (2004).
- A. Serebriakov, F. Bociort, and J.J.M. Braat, "Compensation of the birefringence induced by spatial dispersion in 157 nm lithography", Proc. EOS Topical Meeting "Advanced Imaging Techniques", Delft, The Netherlands (2004).
- A. Serebriakov, E. Maksimov, F. Bociort, and J.J.M. Braat, "The effect of intrinsic birefringence in deep UV-lithography", Proc. SPIE Int. Soc. Opt. Eng. **5249**, 624-635 (2004).
- E. van Driel, F. Bociort, and A. Serebriakov, "Topography of the merit function landscape in optical system design", Proc. SPIE Int. Soc. Opt. Eng. **5249**, 353-363 (2004).
- F. Bociort, E. van Driel, and A. Serebriakov, "Network structure of the set of local minima in optical system optimization", Proc. SPIE Int. Soc. Opt. Eng. **5174**, 26-34 (2003).
- F. Bociort, A. Serebriakov, and J.J.M. Braat, "Local optimization strategies to escape from poor local minima", Proc. SPIE Int. Soc. Opt. Eng. **4832**, 218-225 (2002).

Conference abstracts:
- A. Serebriakov, F. Bociort, and J.J.M. Braat, "Polarization issues caused by spatially induced birefringence in deep UV lithography", 6th ASML Technology Conference, Veldhoven, The Netherlands (2005).

- A. Serebriakov, F. Bociort, and J.J.M. Braat, "Birefringence induced by spatial dispersion in modern lithography. New reasons for concern?", 5th ASML Technology Conference, Veldhoven, The Netherlands (2004).
- A. Serebriakov, F. Bociort, and J.J.M. Braat, "Compensation of the birefringence induced by the spatial dispersion in lithographic optical design", Digest of 4th International Symposium on 157 nm Lithography, Yokohama, Japan (2003).
- A. Serebriakov, F. Bociort, and J.J.M. Braat, "Design of lithographic objectives including the effect of spatially induced birefringence", 4th ASML Technology Conference, Veldhoven, The Netherlands (2003).
- A. Serebriakov, F. Bociort, and J.J.M. Braat, "Spatial dispersion in crystals as a showstopper for deep UV lithography", Proc. V Int. Conf. Applied Optics-2002, St. Petersburg, Russia, (2002).